Double perovskites with ferromagnetism above room temperature

TOPICAL REVIEW

Double perovskites with ferromagnetism above room temperature

D Serrate[1,2], J M De Teresa[1] and M R Ibarra[1,2]

[1] Instituto de Ciencia de Materiales de Aragón, Universidad de Zaragoza-CSIC, Spain
[2] Instituto de Nanociencia de Aragón, Universidad de Zaragoza, Spain

Abstract

We review the structural, magnetic and transport properties of double perovskites ($A_2BB'O_6$) with ferromagnetism above room temperature. Ferromagnetism in these compounds is explained by an indirect B–O–B$'$–O–B exchange interaction mediated by itinerant electrons. We first focus on the BB$'$ = FeMo-based double perovskites, with Sr_2FeMoO_6 (T_C = 420 K) being the most studied compound. These compounds show metallic behaviour and low magnetic coercivity. Afterwards, we will focus on B$'$ = Re compounds, where the significant orbital moment of Re plays a crucial role in the magnetic properties, for example in the large magnetic coercivity and magnetostructural coupling. More specifically, we first discuss the A_2FeReO_6 series, with maximum T_C = 520 K for Ca_2FeReO_6, which shows a tendency to semiconducting behaviour. Finally, we describe the $Sr_2(Fe_{1-x}Cr_x)ReO_6$ series, with maximum T_C = 625 K for Sr_2CrReO_6, which is the highest T_C in an oxide compound without Fe. This compound is metallic. We discuss the impact of these materials for spin electronics in the light of their high spin polarization at the Fermi level and metallicity. In particular, we focus on the large intergrain magnetoresistance effect observed in polycrystalline samples and the possible implementation of these materials as electrodes in magnetic tunnel junctions.

(Some figures in this article are in colour only in the electronic version)

Contents

1. Introduction

1.1. Historical overview

Oxide perovskites with ferromagnetic behaviour around room temperature were first reported in 1950 in the pioneering studies on manganites ($AMnO_3$; A = divalent or trivalent cation) by Jonker and Van Santen [1]. In these compounds, the existence of mixed valence in Mn allowing for an electron transfer through oxygen orbitals was invoked in order to explain the ferromagnetic behaviour via a double exchange mechanism proposed by Zener [2]. This discovery encouraged further studies on oxide materials that could show ferromagnetism at high temperatures via some electron transfer mechanism between mixed valence transition metals, in analogy to the observed behaviour in manganites. In 1961, ferrimagnetic behaviour above room temperature in $B' = $ Re-based double perovskite oxides ($A_2BB'O_6$; A = divalent or trivalent cation; B and $B' = $ transition metals) was reported by Longo and Ward [3]. Subsequent experiments on Re-based double perovskites further explored their magnetic and electrical properties [4, 5]. This finding on Re-based double perovskites stimulated the research on new ferromagnetic compounds with double perovskite crystallographic structure, such as $B' = $ Mo-based and $B' = $ W-based double perovskites, reported by Patterson and co-workers in 1963 [6]. That study showed that ferromagnetism above room temperature was also possible in some of these compounds. Strong steric effects associated with the cation size at the A site of A_2FeMoO_6 were already noticed in the study by Galasso *et al* [7]. Since these initial times, it was noticed that ordinary superexchange rules could not account for the ferrimagnetic ordering of B and B' sites observed with microscopic techniques in these compounds [5, 8–10]. Unexpectedly, the A_2FeMoO_6 and A_2FeReO_6 compounds were also found to be highly conductive [5, 9]. All these features suggested that the involved physics was much richer than expected. Even though some small activity kept on going on this class of materials for the next three decades, the publication by Kobayashi *et al* in 1998 of the half-metallic properties of Sr_2FeMoO_6 triggered a renewed interest in these materials in the context of their potential applications in the field of spin electronics [11]. In fact, that paper by Kobayashi *et al* has been cited more than 610 times according to the *ISI Web of Knowledge* database. However, we notice that no review article has been published so far on these materials in sharp contrast with the case of, for example, manganite oxides. In this article, we will review the experiments performed on this subject during the last six years and we will discuss the basic aspects required for the understanding of these materials. Besides, we will provide the references of some of the most relevant studies on this topic, which will allow the reader to go deeper in the subject, and we will illustrate the physical ideas with part of our contributions to the field. However, it is not our aim to carry out a detailed review of all the references on this topic published in
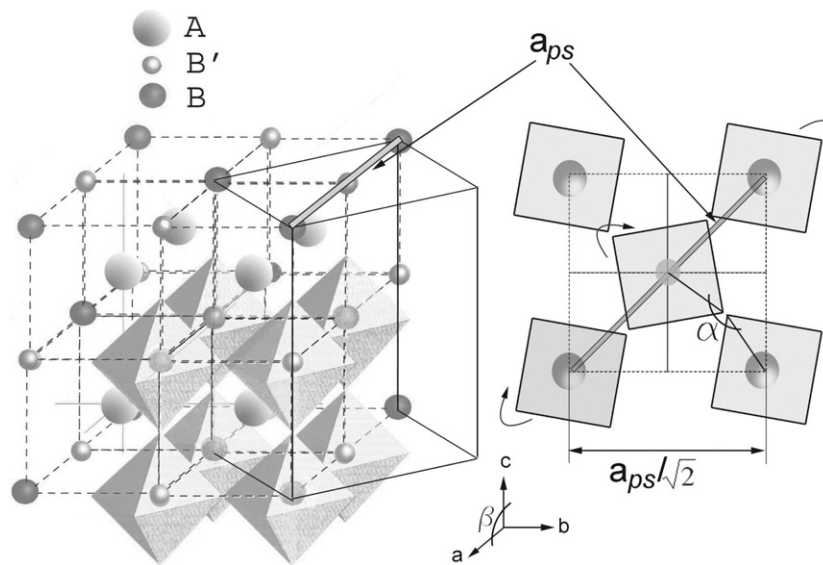
Figure 1. Left: structure of an ideal cubic double perovskite with chemical formula $A_2BB'O_6$. Oxygen atoms are located at the octahedra vertex and B and B$'$ atoms are alternated. Solid lines depict the tetragonal unit cell. Right: top view of the tetragonal unit cell showing the $a^0a^0c^-$ tilting. The thick line is the lattice parameter of the cubic (left) and pseudocubic (right) cell.

literature so far, which incidentally could be an interesting approach for a future review of this subject.

1.2. Crystallographic structure

Double ordered perovskites ($A_2BB'O_6$) possess a modified perovskite structure (ABO_3) where the BO_6 and $B'O_6$ octahedra are alternatively arranged in two interleaving fcc sublattices. The A sites are occupied by alkaline or rare earth ions, while the B sites correspond to transition metal ions, as shown in figure 1. This cubic structure can be well described within the $Fm3m$ space group. However, this structure is very often distorted as a consequence of steric pressure and temperature variations. As in the case of the manganites, the octahedra can undergo cooperative tilting distortions towards the most energetically favourable structure in response to the size mismatch between the A and B–B$'$ cations, which brings about a symmetry reduction of the cubic cell. By means of the $a^0a^0c^-$ tilting in Glazer's notation, the cubic structure transforms into a tetragonal one. The pristine cubic cell is then denominated the *pseudocubic* cell, and the $Fm3m$ space group no longer applies because several symmetries, such as the C_4 around the a axis and the σ_h with respect to the (001) plane, are lost. Instead, the higher set of symmetry operations compatible with the evolution of the structural parameters is that one of the $I4/m$ tetragonal space group. As shown in figure 1, when the tetragonal distortion takes place, a new unit cell can be found. The actual unit cell is smaller than the pseudocubic cell, having the a and b axis along the pseudocubic [110] and [$\bar{1}$10] lattice vectors.

As explained in figure 1, the lattice parameters of the tetragonal (*tetra*) and the pseudocubic (*ps*) cells are related as follows,

$$c = c_{\text{tetra}} = c_{\text{ps}}$$
$$a = b = a_{\text{tetra}} = a_{\text{ps}}/\sqrt{2}. \tag{1}$$

Thus, the lattice parameter of the pseudocubic cell, a_{ps}, which is equal to c prior to the distortion, can be used to quantify the *tetragonal distortion* as

$$t \equiv 1 - \frac{a_{ps}}{c} = 1 - \frac{a\sqrt{2}}{c}. \tag{2}$$

The double perovskite structure can also show a lower degree of symmetry, especially when very small cations are placed at the A site. This is the monoclinic $P2_1/n$ space group, which is generated by the $a^0b^-c^-$ tilting of the cubic structure. In this case, $a \neq b \neq c$ and $\beta \neq 90°$. The crystallographic structure of a double perovskite can be anticipated beforehand on the basis of the mismatch between the length occupied by the A cation and the space left inside the oxygen interstices (see figure 1). In order to measure such mismatch, we can define a tolerance factor analogously to the perovskites. The tolerance factor in double perovskites, f, has to take into account the two possible distances B–O and B′–O, so

$$f \equiv \frac{r_A + r_O}{\sqrt{2}(\langle r_B \rangle + r_O)} \tag{3}$$

$$f_{obs} = \frac{d_{A-O}}{\sqrt{2}\langle d_{B-O} \rangle} \tag{4}$$

where r_i is the effective ionic radius of the i atom ($i =$ A, B, B′, O) tabulated by Shannon, and d_{j-O} are the averaged atomic distances between the j atom ($j =$ A, B, B′) and the nearest oxygen neighbours that belong to the AO_{12}, BO_6 or $B'O_6$ polyhedra. Here '$\langle \rangle$' stands for the average of the B and B′ parameters. Equation (4), which defines the observed tolerance factor (f_{obs}), is the closest experimental approach to the definition. The d_{A-O} calculation in the case of structures different from cubic yields a very complex explicit formula, and the use of the FULLPROF software package is preferred. The measurement of f_{obs} entails an accurate determination of the oxygen positions. X-rays are weakly scattered by oxygen, so the most suitable technique is the neutron powder diffraction. However, it might exist some discrepancy between the definition and the experimental value, because the former is based on calculated chemical bond lengths of the atoms in different compounds and the latter on the experimental distances between nuclei. It is noteworthy that in the A_2FeMoO_6 compounds, and following equation (3) and Shannon's tabulated values [12], the theoretical tolerance factors for the A = Ca ($P2_1/n$), Sr ($I4/m$) and Ba ($Fm3m$) become respectively 0.9422, 0.9766, and 1.026, whereas the observed ones are 0.9522, 0.9984 and 1.000 respectively. The calculated tolerance factors of the most representative double perovskites in the literature are listed in table 1. The f value has been calculated assuming the valence state for the B and B′ atoms on the basis of a number of experimental evidences (namely NMR, XAS, Mössbauer spectroscopy, optical conductivity experiments and bond valence calculations). When no reported values of the B and B′ oxidation states exist in the literature, a 3+/5+ state has been assumed for the f calculation. Except in rare cases, which can be ascribed to the uncertainty in the valence assessment, one can readily observe that the following recipe holds true for the whole $A_2BB'O_6$ family: *For $f > 1.05$ an hexagonal structure is adopted, for $1.05 > f > 1.00$ the compound becomes cubic within the $Fm3m$ space group, for $1.00 > f > 0.97$ the most likely structure corresponds to the $I4/m$ tetragonal space group, and finally, if $0.97 > f$ the compound becomes either monoclinic ($P2_1/n$) or orthorhombic.* A similar conclusion was reached by Philipp *et al* [13] by means of a SPuDS [14] simulation for the bond lengths intervening in equation (4).

Generally speaking, the trend of f_{obs} agrees with the theoretical one (f), as shown in table 1. The listed structural data are chosen at the lowest temperature which is available in the literature, so that the data reflect the structural ground state quite reliably. When f_{obs} is

Table 1. Main crystallographic and physical properties of the $A_2BB'O_6$ double ordered perovskites: theoretical tolerance factor (f) as obtained from the definition given in equation (3) and Shannon's table [12]; observed tolerance factor (f_{obs}) as calculated from the crystallographic structures reported in the first reference of each compound; reported crystallographic space group (H = hexagonal, and O = orthorhombic in the case of an unknown space group); lattice parameters (a, b, and c); tetragonal distortion (t) as defined in equation (2); representative valence states of the B and B′ atoms determined on the basis of NMR, XAS, optical conductivity, bond valence sum rule applied to neutron diffraction data and/or Mössbauer experiments (which can be found in the listed references); and magnetic ordering temperature. When no reported valence state exists in the literature, a 3+/5+ state has been assumed for the f calculation. The structural data always correspond to the first reference given for each compound. The magnetic ordering temperature (T_C/T_N) corresponds to the ferromagnetic/ferrimagnetic to paramagnetic transition. The magnetic ordering type is specified (PM = paramagnetic for the whole temperature range, AFM = antiferromagnetic, C = canted ferromagnetism) if different from ferromagnetic or ferrimagnetic.

B	Cr			Mn			Fe			Co
A₂ B′	Mo	Re	W	Mo	Re	W	Mo	Re	W	Re
Ba₂ (Ref.)	[15]	[4]	[13]	—	[16, 3, 5]	[17]	[18, 6, 7, 9, 19, 20]	[21, 22, 4, 5]	[23]	[5, 3]
f/f_{obs}	1.0576/—	1.0655/—	1.0549/—	1.0497/—	1.018/1.000	1.006/1.001	1.026/1.000	1.044/1.000	1.018/1.006	1.0395/—
Space group	$P6_3/mmc$	H	$P\bar{6}2c$	—	$Fm3m$	$Fm\bar{3}m$	$Fm3m$	$Fm3m$	$I4/m$	$Fm3m$
Lattice (Å)				—						
a	5.694	4.94	5.70	—	8.1865	8.1844	8.0121	8.0518	5.7446	8.078
b/t (×10³)	—/—	—/—	—/—	—	—/0	—/0	—/0	—/0	—/1.7	—/0
c	13.985	13.8	13.99	—	—	—	—	—	8.1099	—
Valence B, B′	—	—	—	—	2+/6+	2+/6+	2.5+/5.5+	2.5+/5.5+	2+/6+	2+/6+
T_C/T_N (K)	PM	PM	145-PM[a]	—	110	45-AFM[a]	308	303	40-AFM	40-AFM
Sr₂ (Ref.)	[24–26, 6]	[27, 28]	[13, 6, 29]	[26, 30]	[31]	[32]	[18, 48, 11, 7, 33]	[28, 21, 22, 34]	[23, 35]	[28, 4]
f/f_{obs}	0.9978/0.9996	0.9947/0.9996	0.9838/—	0.9905/1.0000	0.9608/0.9337	0.9495/0.9927	0.9766/0.9984	0.9850/0.9984	0.9608/0.9927	0.9808/0.9968
Space group	$I4/m$	$I4/m$	$Fm3m$	$Fm3m$	$P2_1/n$	$P4_2/n$	$I4/m$	$I4/m$	$P2_1/n$	$I4/m$
Lattice (Å)										
a	5.5335	5.5206	7.832	8.0056	5.651	7.9992	5.5705	5.561	5.643	5.5659
b/t(×10³)	—/0.05	—/0.6	—/0	—/0	5.6378/2.4	—/0.8	—/5.9	—/4.6	5.5856/8.6	—/7.1
c	7.8251	7.8023	—	—	7.9731	8.0058	7.9253	7.9008	7.9128	7.9508
Valence B/B′	3+/5+	2.5+/5.5+	2.5+/5.5+	3+/5+	2+/6+	2+/6+	2.5+/5.5+	2.5+/5.5+	2+/6+	2+/6+
T_C/T_N (K)	420	620	458	12-AFM	120-C	13-AFM[a]	420	400	40-AFM	65-AFM

Table 1. (Continued.)

| B | Cr | | | Mn | | | Fe | | | Co |
A$_2$ B$'$	Mo	Re	W	Mo	Re	W	Mo	Re	W	Re
Ca$_2$ (Ref.)	[6]	[28, 36]	[13, 6]	—	[28, 4]	[37]	[18, 19, 9, 7, 6]	[38, 39, 22, 21]	[40]	[28, 4]
f/f_{obs}	0.9627/—	0.9699/0.9837	0.9382/—	0.9556/—	0.9270/—	0.9161/0.9774	0.9422/0.9531	0.9627/0.9522	0.9533/0.9979	0.9463/0.9743
Space group	O	$P2_1/n$	$P2_1/n$	—	$P2_1/n$	$P2_1/n$	$P2_1/n$	$P2_1/n$	$Pmm2$ (O)	$P2_1/n$
Lattice (Å)										
a	5.49	5.3886	5.39	—	5.44651	5.4457	5.3875	5.390/7.623	5.4242	5.402 66
$b/t(\times10^3)$	7.70/8.3	5.4604/5.1	5.45/4.9	—	5.639 97/9.5	5.6529/10.4	5.5027/7.5	5.5165/6.4	5.5108/4.4	5.573 47/5.9
c	5.36	7.6598	7.66	—	7.776 57	7.7828	7.6767	7.6719	7.7051	7.686 07
Valence B, B$'$	—	3+/5+	2+/6+	—	2+/6+	2+/6+	2.5+/5.5+	2.5+/5.5+	—	2+/6+
T_C/T_N (K)	148	360	160	—	110	16-AFM	365	522	—	130-AFM[a]

[a] The appearance of weak ferromagnetism or canted antiferromagnetism below the ordering temperature.
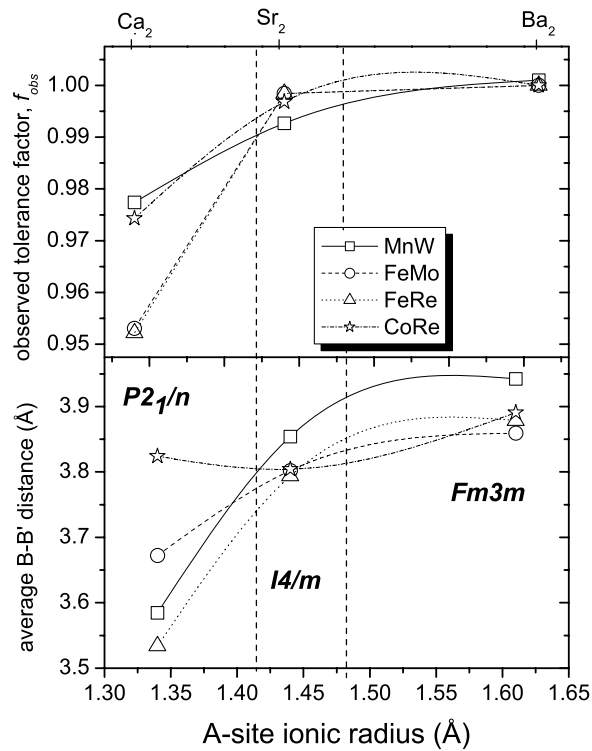
Figure 2. Dependence of the observed tolerance factor (upper panel) and the average distance between the two B crystallographic sites (lower panel) as a function of the ionic radius of the atom occupying the A site: $BB' = MnW$ (squares), MoFe (circles), FeRe (triangles), and CoRe (stars). Structural parameters are taken from table 1.

calculated within the $Fm3m$ space group, the symmetry constraints bring about an observed tolerance factor equal to 1 within the experimental error. In the case of non-cubic space groups, f_{obs} provide an experimental measure of the extent of the octahedra tilting distortion. As shown in figure 2, one can notice that when the B and B' cations do not change (for instance in compounds having $BB' = MnW$, FeMo, FeRe and CoRe), the f_{obs} deviates from 1 as the cation occupying the A site decreases its size, r_A, from Ba_2 to Ca_2. Figure 2 also displays how the average distance between the B and B' metals (calculated as one half of a_{ps}) undergoes an overall strong reduction when r_A decreases. Moreover, due to the gradual r_A decrease and the required distortion in order to accommodate the empty space, the symmetry is reduced from cubic $Fm3m$ for $A_2 = Ba_2$ to tetragonal $I4/m$ for $A_2 = Sr_2$. The symmetry is further decreased to monoclinic $P2_1/n$ for $A_2 = Ca_2$. We anticipate that the distortion associated with such symmetry reduction will largely influence the magnetic and transport properties, as can be readily seen from the T_C values listed in table 1.

1.3. Interplay between electronic structure and magnetism

Ferromagnetism in high T_C double perovskites arises from the spin of the B and B' site ions. Given the unique aspects of Sr_2FeMoO_6 (SFMO) and its historical importance, we will discuss its electronic and magnetic properties as an archetypal double perovskite. In SFMO, the $Fe^{3+}(3d^5)$ and $Mo^{5+}(4d^1)$ orbitals are at octahedral interstices formed by negative

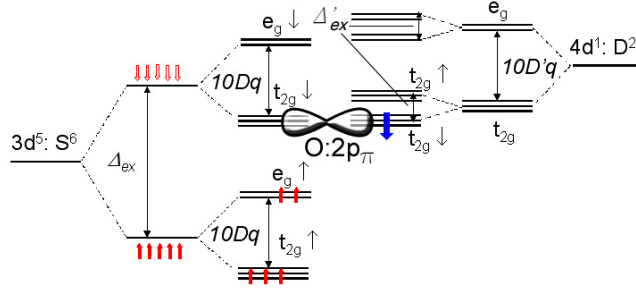**Figure 3.** Energy levels schematic diagram of Sr_2FeMoO_6 as calculated by Kobayashi [11]. The Fermi level lies at the band formed exclusively by the $Fe(t_{2g}\downarrow)$–$O(2p)$–$Mo(t_{2g}\downarrow)$ sub-band.

O^{2-} charges (see figure 1). Consequently, the ground state is a triplet, and the first excited state a doublet, namely the $|t_{2g}\rangle$ and $|e_g\rangle$ respectively. They are separated by an energy gap $\Delta_{CEF} = 10Dq \sim 1$ eV [11], where Dq is the strength of the crystal electric field [41].

$$|e_g\rangle \begin{cases} d_{3z^2-r^2} = |2,0\rangle \propto \dfrac{1}{2}\dfrac{2z^2-x^2-y^2}{r^2} \\[2mm] d_{x^2-y^2} = \dfrac{1}{\sqrt{2}}(|2,2\rangle + |2,-2\rangle) \propto \dfrac{\sqrt{3}}{2}\dfrac{x^2-y^2}{r^2} \end{cases}$$
$$|t_{2g}\rangle \begin{cases} d_{xy} = \dfrac{1}{i\sqrt{2}}(|2,2\rangle - |2,-2\rangle) \propto \sqrt{3}\dfrac{xy}{r^2} \\[2mm] d_{yz} = -\dfrac{1}{i\sqrt{2}}(|2,1\rangle + |2,-1\rangle) \propto \sqrt{3}\dfrac{yz}{r^2} \\[2mm] d_{zx} = -\dfrac{1}{\sqrt{2}}(|2,1\rangle - |2,-1\rangle) \propto \sqrt{3}\dfrac{zx}{r^2} \end{cases} \quad (5)$$

x, y, and z being atomic coordinates and $|l,m\rangle$ the spherical harmonics.

In the high spin configuration, the Fe^{3+} atom bears a $S = 5/2$ spin moment. This entails a strong exchange splitting $\Delta_{ex} \sim 3$ eV between the spin up and spin down states, as has been shown in band structure calculations based on density functional theory (DFT) [11, 42]. The same result is obtained for Fe atoms having Re neighbours [43, 44], whereas in the case of $B = Cr$ (Cr^{3+}, $S = 3/2$) and $B = Mn$ (Mn^{2+}, $S = 5/2$) compounds the Hund's intra-atomic exchange splitting amounts to about 2 eV [13, 44, 45] and 4 eV [44] respectively. Therefore, in most of the cases $\Delta_{ex} \gg \Delta_{CEF}$ at the B site. On the contrary, the exchange coupling strength of the non-magnetic B' site is negligible, so that the splitting due to the CEF prevails. For instance, Δ_{ex} of the $Mo^{5+}(4d^1)$ manifold is nearly one order of magnitude smaller than in 3d atoms, as shown in figure 3. Within this ionic picture one might suppose that, in analogy with the manganites, the antiferromagnetic superexchange interaction between neighbouring B and B' sites having occupied and partially filled t_{2g} states [46], would bring about a ferrimagnetic arrangement of their 5 μ_B/f.u. and -1 μ_B/f.u. respective spin moments. However, this model does not support two of the main physical properties of SFMO. First, the highly spin polarized metallic state below T_C [11, 47] and the non-integer valence of Fe reported in Mössbauer and x-ray absorption experiments [21, 48–51]. Second, the high magnetic ordering temperature observed in SFMO is incompatible with a superexchange-based magnetic coupling within a localized picture of the d-type electrons. Although neutron powder diffraction, NMR and XMCD studies have shown experimental evidences of the ferrimagnetic arrangement [18, 52–54], the large T_C values would require a superexchange coupling between Mo and Fe at least comparable to that of Mn^{4+}–Mn^{4+} pairs in manganites
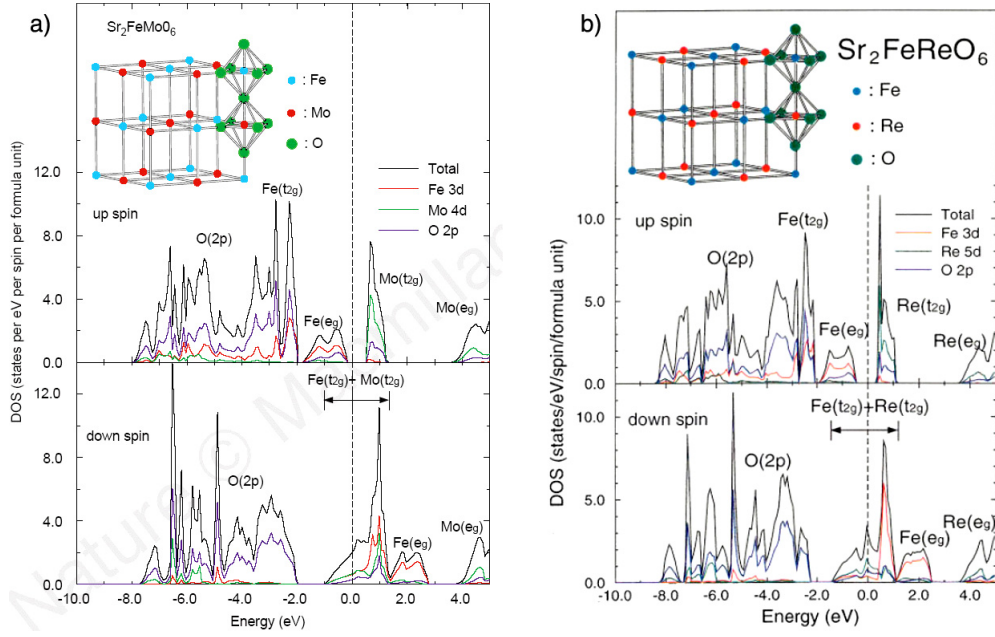
Figure 4. The density of states of Sr_2FeMoO_6 (a) and Sr_2FeReO_6 (b) as calculated by Kobayashi [11, 43]. The Fermi level lies at the band formed exclusively by the $Fe(t_{2g}\downarrow)$–$O(2p)$–$Mo/Re(t_{2g})$ sub-band.

(T_N = 120 K in $CaMnO_3$ [55]), which is not expected due to the non-magnetic nature of Mo. Furthermore, magnetic susceptibility measurements in the paramagnetic regime yielded a positive exchange Curie–Weiss constant, thus suggesting a magnetic interaction which is ferromagnetic in nature [56]. Besides these observations, in table 1 a clear coincidence between the high Curie temperature and the B^{2+}/B'^{6+}–B^{3+}/B'^{5+} mixed valence state can be noticed (see for instance the A_2FeMoO_6, A_2FeReO_6, A_2CrReO_6, and A_2CrWO_6 series).

Therefore, we must incorporate the electronic structure into the magnetic model. In the pioneer calculation of the density of states (DOS) by Kobayashi *et al* using the DFT technique [11], the majority spin up channel exhibits a band gap of ~0.8 eV. The minority spin down Mo and Fe t_{2g} levels are partially filled, whereas the e_g levels are empty (see figure 4(a)). The bands lying at the Fermi level exhibit a *full negative spin polarization* ($P = -1$), and are predominantly from Mo and Fe t_{2g}, with some small admixture of the O 2p states. The calculation yields the expected values for the Δ_{CEF}, and for the exchange splitting at the Fe atom, Δ_{ex}. However, the Mo $t_{2g}\downarrow$ is anomalously broadened and pushed down to the Fermi level. Considering a tight binding model containing d orbitals at the Fe and Mo sites, and p orbitals at the oxygen sites, Sarma *et al* [42] realized that this anomalous splitting could only be fitted with an effective intra-atomic exchange strength, Δ'_{ex}, approximately 20 times larger than the expected one for a non-magnetic atom like Mo. The key ingredient for such an enhanced Δ'_{ex} is the presence of electron hopping interactions between Fe and Mo states with the same spin and orbital symmetry, which allow the $Fe(t_{2g})$–$O(2p)$–$Mo(t_{2g})$ hybridization and, as a consequence, lower in energy the Mo spin down states, whereas the spin up states are pushed further up. In agreement with the experimental observations [21, 19, 48–50, 57–62], the charge transfer due to the hopping mechanism produces a $Fe^{(3-\delta)+}/Mo^{(5+\delta)+}$ (or $Fe^{(3-\delta)+}/Re^{(5+\delta)+}$) state with $0 < \delta < 1$, as originally proposed by García-Landa *et al* [63]. In addition,

since the available Fe t_{2g} states are purely spin down polarized, the electron hopping can only occur when the localized Fe spin moments are ferromagnetically aligned. Thus, the hopping interaction reinforces the ferromagnetic arrangement of the nearest neighbouring Fe atoms, consequently increasing T_C. The antiferromagnetic coupling between Fe and Mo prior to the hopping interaction is crucial, otherwise the shift of the bare $t_{2g}\downarrow$ and $t_{2g}\uparrow$ Mo levels would have opposite direction, resulting in a reduced T_C [42].

The compulsory requirement in Sarma's model is that the Fermi level must be located within the large energy gap in the electronic band structure of the B atom states. In the case of Sr_2FeMoO_6 [11] and Sr_2FeReO_6 [43], the gap is formed between the Fe $e_g\uparrow$ and $t_{2g}\downarrow$ bands, as shown in figure 4, whereas in the A_2CrWO_6 compound the gap is located between the Cr $t_{2g}\uparrow$ and $e_g\uparrow$ bands [13, 45]. The energy gain by exchange splitting due to the hopping mechanism between non-magnetic atoms and high spin 3d metals was generalized by Kanamori *et al* [64] for other transition metal compounds. On the other hand, the A_2FeWO_6 series (A = Ba, Sr) was found to be insulating and to show commensurate antiferromagnetic arrangements of the Fe moments [23], which might result from the strong Fe^{2+}/W^{6+} character of the valence state and the consequent absence of hopping electrons. As discussed by Fang *et al* [65], the higher energy of the W 5d states as compared to the Mo 4d and Re 5d ones passivates the hopping mechanism. Then, the bare antiferromagnetic superexchange interaction stabilizes the low Néel temperature antiferromagnetism observed in Sr_2FeWO_6 compound. This has been recently illustrated using a simplified double exchange Hamiltonian in the $Sr_2FeMo_xW_{1-x}O_6$ series alloyed at the B′ site [66], which shows an AFM insulator to FM metal transition when increasing the Mo content for $x \sim 0.3$, in agreement with earlier experimental data [35]. As shown in table 1, ferromagnetism was also found in A_2CrReO_6 [27, 28], A_2MnReO_6 [16, 31] and also in a variety of B-substituted compounds [28, 24, 67].

The saturation magnetization value (M_S) at low temperatures is well described within the simplest ionic picture of an antiferromagnetic arrangement between the Fe^{3+} core spin and the Mo^{5+} 4d electron. This gives, in the case of A_2FeMoO_6, the following spin counting per formula unit (see figure 3): $g_J\mu_B(5/2 - 1/2) = 4\ \mu_B/f.u.$, g_J being the Landé factor when only the spin contributes to the angular momentum. Equivalently, if we split the ferromagnetic contribution into a localized part (5 $\mu_B/f.u.$ from the Fe core spin) and an itinerant part arising from the fully spin down polarized t_{2g} conduction band ($-1\ \mu_B/f.u.$), the sum becomes the same. Similar arguments can be given for the A_2FeReO_2 [22], A_2CrReO_6 [27, 36] and A_2CrWO_6 [13] ferromagnetic compounds, which gives rise respectively to 3 $\mu_B/f.u.$, 1 $\mu_B/f.u.$ and 2 $\mu_B/f.u.$ expected values of M_S.

1.4. Basic theoretical concepts

Later on, there were two theoretical attempts to describe this hopping interaction within the framework of a kinetically driven double exchange interaction. Chattopadhyay and Millis [68] proposed a many body Hamiltonian with an on-site energy for the B sublattice, plus three 2D hopping interactions, acting each one independently in the three planes set by the allocation of the t_{2g} states. The on-site energy has a Hund's coupling term and a site dependent contribution that is equal to the difference in energy between the Mo and Fe t_{2g} states, Δ. They allow for hopping within and between the B and B′ sublattices. The dynamic mean field theory yields for this model a strong dependence of T_C on the bandwidth and the conduction band filling. T_C is maximized if the hopping probability within the same sublattice tends to zero. In this model, the term '*double-perovskite-double-exchange*' describes the limit in which hopping interactions involves exclusively jumps between B and B′ sublattices, while standard '*double exchange*' would apply only for the case where both sublattices are not coupled and

hopping does only occur between the same kinds of atoms, following the original Zener's description [2].

Alonso *et al* [69] proposed an equivalent Hamiltonian, but using a variational mean field approach and assuming an infinite Hund's coupling at the Fe sites. In their approximation, not only contains the kinetic energy terms for hopping between Fe–Mo nearest neighbours, but also between Mo–Mo nearest neighbours. Thus, when they evaluate the energy of the trial solutions, the hopping between and within sublattices is taken into account, like in Chattopadahyay's model. Both calculations, similarly to the more recent one carried out by Carvajal *et al* [66], foresee a T_C reduction when increasing the number of delocalized electrons from one to two. This contradicts the recent experimental demonstrations of the effect of band filling, which will be reviewed in section 2.1.

This fact could lead us to question the double exchange scenario for the hopping interactions in double perovskites. However, we point out that Alonso's model gives a very accurate description of the influence of structural disorder in T_C and the magnetization at low temperatures [69]. It seems that the double exchange-like models succeed in the stabilization of the ferromagnetic state at high temperatures and other low temperature properties such as the half-metallicity and the saturation magnetization, but fails in the description of the dependence on the band filling. According to Alonso *et al*, T_C is lowered because on electron doping the Mo $t_{2g}\uparrow$ levels become gradually populated. We wonder whether the theoretical description of magnetism in terms of double exchange should include the antiferromagnetic interaction between Fe and Mo, which is a key ingredient for the T_C enhancement in Sarma's model. This strategy would preclude to some extent the spin up levels population by means of an effective $\Delta_{Mo}\uparrow > \Delta_{Mo}\downarrow$. In this sense, we would like to mention the existence of an example of ferrimagnetic insulating double perovskite with modest T_C, the $Ba_{2-x}Sr_xMnReO_6$ system [16]. This provides experimental support to the existence of a finite AFM coupling between B and B' sublattices in absence of hopping interactions. It is obvious that the failure of the double exchange-like Hamiltonians lies in the double occupancy of Mo spin up and down states in the paramagnetic regime. After submission of this review we became aware of the reported simplification of the DE Hamiltonian into an effective Heisenberg model [70]. In this situation, and instead of using an AFM exchange interaction, the authors are able to include the electronic correlations at the Mo atom aiming to penalize the double occupancy, which allows the authors to reproduce the observed linear T_C increase with electron doping.

Another interesting approach was carried out by Tovar *et al* by means of a description of the coupling between the localized and delocalized spin moments in the framework of the mean field theory [71]. Assuming the role of an additional magnetic lattice for the itinerant electrons, they divide the total magnetization into two parts corresponding to the localized (the B site core spin) and delocalized magnetic moments respectively. The effective magnetic field acting over each pseudolattice is related to the magnetization of the other one by means of an exchange coupling constant termed λ. In order to explain the anomalously reduced paramagnetic effective moment observed in SFMO [71, 72], λ has to be negative, which reflects a strong antiferromagnetic coupling of the itinerant electrons to the localized Fe core spin. In this model T_C is proportional to the product of the density of states at the Fermi level times λ^2. Such a model provides a phenomenological point of view of the ferromagnetic interaction in high T_C double perovskites. However, it will be very difficult to find out the relationship between λ and the structural, electronic and chemical properties that are known to affect very much the magnetic interaction in double perovskites. Moreover, the model overlooks the magnetism of the B' sublattice. In consequence, the superexchange interaction that might exist between B and B' nearest neighbours is neglected. This interaction is a key ingredient in Sarma's double exchange-like model, and could be responsible for the ferrimagnetic behaviour

of the A_2MnReO_6 compounds (see table 1 and references therein). Therefore, the use of the mean field theory for the description of the itinerant magnetism is suitable in the limit of vanishingly small superexchange interactions, and can be helpful in order to parametrize the strength of the B–B′ hopping amplitude in double perovskites.

From a theoretical point of view, the hopping amplitude must be determined by the amplitude of the kinetic terms in the Hamiltonian, which are responsible for the electron delocalization, and consequently for the ferromagnetic ordering of the B sublattice. Such kinetic terms will be relevant whenever the B′ unpaired electrons can be transferred to available B states around the Fermi level with compatible energy eigenvalues, angular momentum and spin quantum numbers. Their amplitude is proportional to the hybridization matrix elements of the atomic potential crossing orbitals that belong to different atoms. Harrison and co-workers calculated the matrix elements crossing p- and d-type states whose reference nuclei are separated by a distance d [73]:

$$V_{\mathrm{pd}m} = \eta_{\mathrm{pd}m} \frac{\hbar \sqrt{r_{\mathrm{p}} r_{\mathrm{d}}^3}}{m_e d^4} \tag{6}$$

where r_{p} and r_{d} are tabulated values of the muffin-tin orbital theory [74] of the p and d states respectively. m_{e} is the electron mass and m is the third component of the angular momentum. It happens that the atomic potential is spherically symmetric, so that it only crosses d and p states with the same m quantum number. As the O 2p states have $m = -1, 0, 1$, the η coefficients are obtained for $m = \pm 1(\pi)$ and $m = 0(\sigma)$:

$$
\begin{aligned}
m = 1 &\Rightarrow \eta_{\mathrm{pd}\pi} = \frac{3\sqrt{5}}{2\pi} \\
m = 0 &\Rightarrow \eta_{\mathrm{pd}\sigma} = -\frac{3\sqrt{15}}{2\pi}.
\end{aligned}
\tag{7}
$$

A glance to equations (5) and (6) unveils that $V_{\mathrm{pd}\pi}$ can only couple $\mathrm{Fe}(t_{2g})$–$\mathrm{Mo}(t_{2g})$ orbitals through π oxygen p states, whilst $V_{\mathrm{pd}\sigma}$ only couples $\mathrm{Fe}(e_g)$–$\mathrm{Mo}(e_g)$ orbitals through σ oxygen p states. For the calculation, Harrison employs the atomic wavefunctions with a first order correction, which is an expansion of orthogonalized plane waves [73]. This sort of wavefunction has a strong atomic character and therefore they are suitable for a tight binding treatment. In the tight binding approach to the electronic bandwidth, the matrix elements crossing wavefunctions belonging to next nearest neighbours, such as Fe and Mo dd hybridization terms, are required. The attempt to calculate such matrix elements entails an enormous complexity, especially for a general geometrical configuration with arbitrary $d_{\mathrm{B-O}}$, $d_{\mathrm{B'-O}}$, and B–O–B′ angle. Some trials have been reported in manganites [75] and titanates [76], showing that the problem is far too much complicated to have an analytical solution.

We will adopt the following approach for the extension of Harrison's results to the cubic double perovskites (having B–O–B′ bond angle equal to 180°). In Harrison's calculations, the first order quantum correction of the atomic wavefunctions gives rise to the coupling between d states and oxygen p states. In order to apply the quantum perturbation theory to calculate the coupling between d and d′ states through the oxygen p states, we have to take into account the shift of the unperturbed function due to every coupled state. Assuming that any kind of coupling rather than the p–d nearest neighbours is negligible, the crossed term of the true Hamiltonian (H) between next neighbouring B and B′ d states would be, at a first order approximation:

$$V_{\mathrm{dpd}\pi} = \langle t_{2g}|H|t'_{2g}\rangle \propto V_{\mathrm{pd}\pi} V'_{\mathrm{pd}\pi} \left[\frac{1}{\varepsilon_{t_{2g}} - \varepsilon_{2\mathrm{p}}} + \frac{1}{\varepsilon'_{t_{2g}} - \varepsilon_{2\mathrm{p}}} \right] \tag{8}$$

$$V_{\mathrm{dpd}\sigma} = \langle e_g|H|e'_g\rangle \propto V_{\mathrm{pd}\sigma} V'_{\mathrm{pd}\sigma} \left[\frac{1}{\varepsilon_{e_g} - \varepsilon_{2\mathrm{p}}} + \frac{1}{\varepsilon'_{e_g} - \varepsilon_{2\mathrm{p}}} \right]. \tag{9}$$
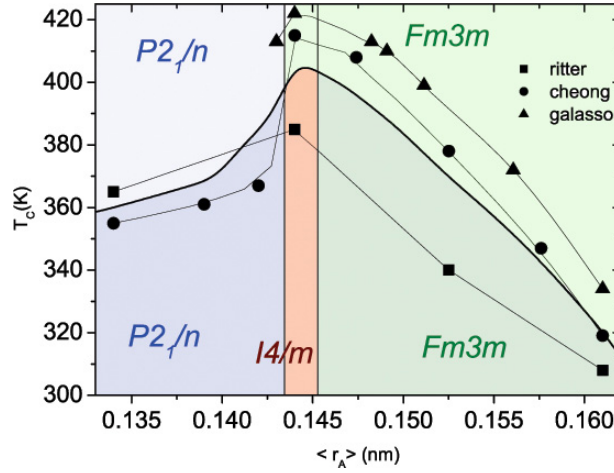
Figure 5. Phase diagram of A_2FeMoO_6 with data taken from several references (squares [18], circles [77] and triangles [7]). The solid line is the averaged value of T_C. Dark areas correspond to the ferromagnetic phase, while lighter ones to the paramagnetic phase.

Here, $V_{dpd\pi(\sigma)}$ accounts for the indirect d–d coupling through oxygen p states, namely the pdd–$\pi(\sigma)$ coupling. ε_i is the energy of the i state in absence of the hopping interaction. Therefore, equations (6)–(9) permit us to estimate the strength of the ferromagnetic interaction in cubic or nearly cubic double perovskites (B–O–B$'$ $\sim$ 180°) on the basis of structural information ($d_{B-O}, d_{B'-O}$) and typical parameters of the atoms such as the $r_{p,d}$ and ε_i. The clear relationship between the $V_{dpd\pi(\sigma)}$ hybridization terms and T_C can be understood in the framework of the Zener's double exchange model [2]. In this model, T_C is proportional to the energy difference between the antiferromagnetic arrangement of the magnetic ions and the ferromagnetic ground state. It is straightforward that such an energy difference must be proportional to the hybridization strength between the orbitals containing the delocalized carriers, $T_C \sim V_{dpd\pi(\sigma)}$.

1.5. Relevance of structural effects

The role played by the structural effects in double perovskites is twofold. First, the amplitude of the hopping interaction responsible for the ferromagnetism is very sensitive to the local geometry of the overlapping orbitals. This is because the first order correction of the wavefunction due to the kinetic term in the Hamiltonian depends on the spatial distribution of the d O(2p) d$'$ states. Consequently $V_{dpd\pi(\sigma)}$ can change very much as a function of the interatomic distances and bond angles (α; see figure 1), as evidenced by equation (6). Second, structural defects are very likely to occur in such complex transition metal oxides. We will show that these structural defects such as antisite disorder, antiphase boundaries and oxygen vacancies give rise to a rich phenomenology in double perovskites.

The influence of the crystallographic structure on the hopping interaction which stabilizes the high temperature ferromagnetism can be illustrated through the archetypal A_2FeMoO_6 series. Several independent publications have confirmed the magnetic phase diagram of A_2FeMoO_6 (A = Ca, Sr, Ba) [7, 18, 77]. As shown in figure 5, all compounds remain ferromagnetic with a fairly large T_C. However, the symmetry is lowered from Ba-rich compounds showing $Fm3m$ cubic space group, to Sr-rich compounds with tetragonal $I4/m$

structure, and finally to Ca-rich compounds with the monoclinic $P2_1/n$ structure. As explained in section 1.2, by means of the octahedra tilt, the lattice compensates the empty space produced by the reduction of the A cation size (according to [12], $r_A = 1.61$, 1.44 and 1.34 Å for Ba^{2+}, Sr^{2+} and Ca^{2+} respectively in XII coordination). On symmetry lowering there is a trade-off between two competing effects having similar energy scales. On the one hand, the interatomic distances decrease due to the atomic size reduction, as shown in figure 2(b), from which the d–d$'$ overlapping (see equation (6)) benefits and therefore increases the hopping amplitude of the kinetically driven magnetic interaction. We have described this amplitude as the hybridization strength given by the pdd–π coupling (in A_2FeMoO_6 the e_g levels are far above in energy from the Fermi level, so the pdd–σ coupling is zero). Obviously, this effect ends up in a strong T_C increase when Ba is replaced by Sr. On the other hand, with further reduction of r_A, the Fe–O–Mo bond angle deviates from 180°, which is detrimental for the hopping amplitude. The monotonic enhancement of the distortion when decreasing r_A can be observed in figure 2(a). The balance of these two effects on the hybridization strength results in a maximum T_C for A = Sr, for which $f_{obs} = 0.9984$, $\langle d_{B-B'} \rangle = 3.8021$ Å and $\alpha = 169°$ in the *ab* plane [18].

In equations (8) and (9), we have put forward an explicit form of the $V_{dpd\pi(\sigma)}$ dependence on the interatomic distances, which agrees qualitatively with the phase diagram shown in figure 5 for $r_A > r_{Sr}$. However, a general description of the hybridization strength as a function of α is not available. Instead, it is convenient to define the tilting angle as $\omega \equiv (\pi - \alpha)/2$. Let us suppose that $T(\omega)$ and $E(\omega)$ are prefactors in equations (8) and (9) that describe the dependence of the hybridization strength on ω for the pdd–π and pdd–σ coupling respectively. Given the cubic symmetry of the t_{2g} and e_g states, $T(\omega)$ and $E(\omega)$ must be even functions of ω. In particular, $E(\omega)$ has been empirically found to follow the law $E(\omega) \sim \cos \omega$ [75, 78], or the more steep $E(\omega) \sim \cos^2 \alpha$ [79]. Thus, we should rewrite equations (8) and (9) as:

$$\text{pdd–}\sigma \text{ coupling } (e_g) \, T_C \propto V_{dpd\sigma} \approx V_{pd\sigma} V'_{pd\sigma} \cos(\omega) \tag{10}$$

$$\text{pdd–}\pi \text{ coupling } (t_{2g}) \, T_C \propto V_{dpd\pi} \approx V_{pd\pi} V'_{pd\pi} T(\omega). \tag{11}$$

Hereafter we assume that the $\varepsilon_{t_{2g}(e_g)}$, $\varepsilon'_{t_{2g}(e_g)}$ and ε_{2p} values are constant given a fixed B–B$'$ couple. Okimoto *et al* [76] calculated $T(\omega)$ in the tight binding approximation for (La, Y)TiO_3. One could extract the functional form of $T(\omega)$ as $T_C/(V_{pd\pi} V'_{pd\pi})$. However, these authors do not provide reliable structural data, which makes impossible to calculate ω and $V_{pd\pi}$. As will be discussed later, further work on this issue would help to understand the impact of the structural distortions in non-cubic magnetic double perovskites.

Regarding the structural defects, the most probable ones to occur are the *antisite disorder* (AS) and *oxygen vacancies*, although *antiphase boundaries* [80] and *A cation vacancies* are also likely to appear. The AS is defined in this review as the percentage of misplaced B ions at B$'$ sites and vice versa. Thus, a complete disordered sample would be denoted by AS = 50%, and would be like an ABO_3–$AB'O_3$ alloy. In the ferromagnetic compounds, the AS disorder always leads to a decrease in the saturation magnetization, because it naturally prevents the B moments from the fully aligned pattern. AS can be experimentally inferred from the intensities of certain nuclear Bragg peaks in neutron and x-ray powder diffraction. These are superstructure peaks that reflect the cation ordering at the B and B$'$ sublattices. For instance, in the cubic $Fm3m$ structure, the main superstructure Bragg reflections are (111), (113) and (331), which vanish as the AS approaches 50% [126]. In addition, since Fe atoms out of regular sites experience a different local magnetic field, the hyperfine splitting of the nuclei states is sensitive to the appearance of AS disorder. Thus, Mössbauer spectroscopy can also be used to quantify the AS percentage [50]. Similarly, the hyperfine field on the Mo atom induced by the spin down t_{2g} electrons can distinguish between regular and misplaced Mo, and
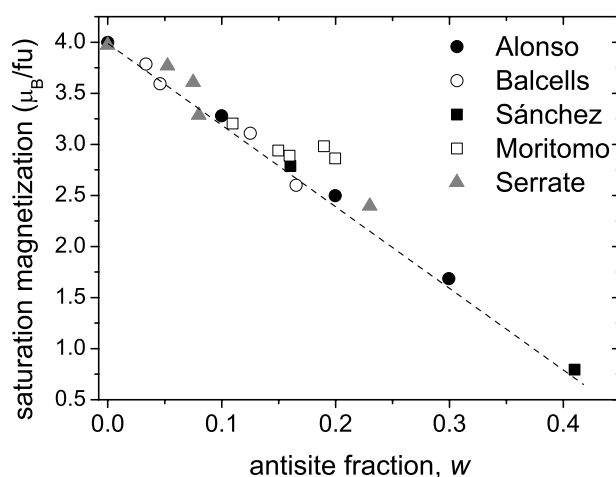
14

Figure 6. Comparison of the theoretical (solid circles [69]) and experimental values (empty circles [49], solid squares [53], empty squares [84], and triangles [83]) of the low temperature saturation magnetization as a function of the AS fraction in A_2FeMoO_6.

therefore NMR can also give an insight into the AS concentration [19, 81]. It is believed that the presence of AS defects manifests itself as a low frequency peak at around 51 MHz [19, 51, 81]. Nevertheless, Wojcik *et al* showed that such a peak was insensitive to the AS degree of their samples [82]. The origin of this controversy might be the different kinds of Mo defective sites contributing to the low frequency peak [51].

In the case of A_2FeMoO_6, several authors have reported the following dependence for M_S on the fraction of AS disorder, w [49, 53, 83]

$$M_S = (4 - 8w)\mu_B/\text{f.u.} \tag{12}$$

These experimental observations are in agreement with the magnetic behaviour of single crystals as a function of AS [84], and supported by Monte Carlo simulations [85] and the variational mean field treatment of the double exchange Hamiltonian [69]. As suggested by Balcells *et al* [49], equation (12) can be understood within the simplest ferrimagnetic model in which the B and B′ sublattices are antiferromagnetically coupled. In that case, each misplaced Fe ion reduces M_S by $2 \times 5 = 10 \ \mu_B$, while each misplaced Mo increases M_S by $2 \times 1 = 2 \ \mu_B$. Therefore, as there are w misplaced atoms per formula unit, $M_S = 4-8w \ \mu_B/\text{f.u.}$ A more realistic description is given in [69]. Here, with the only assumption of an AFM superexchange coupling in the Fe–O–Fe path (which is true in the isostructural and isoelectronic $LaFeO_3$ compound), the same tendency is confirmed, as shown in figure 6. In this latter case, the Mo–Mo interactions are neglected as a consequence of the paramagnetic nature of $SrMoO_3$. Then, if misplaced Mo atoms do not contribute to the deviation of M_S, how is it possible that the simulations did not yield a M_S versus w slope closer to -10? The reason is that the simple assumption of a $10 \ \mu_B$ decrease per misplaced Fe ion does not hold true if one takes into account the existence of different environments for the misplaced Fe atoms, with $0, 1, \ldots, 6$ Fe neighbours. As observed in the Monte Carlo simulations [85], the misplaced Fe atoms with similar amount of Fe and Mo neighbours experience magnetic frustration, so that not all of them contribute with $-10 \ \mu_B$ to M_S. In fact, element specific XMCD measurements showed that the individual Fe spin moments are strongly reduced with increasing disorder [86].

Moritomo *et al* have shown that an AS increase from 11% to 20% is detrimental for the stabilization of long range magnetic ordering in single crystals [84]. One might think

that even larger AS disorder would lead to samples with strongly reduced T_C. However, in highly disordered samples (AS $\sim$40%) it has been shown the appearance of FM contributions in neutron powder diffraction below 750 K. The reason is the large Néel temperature of the antiferromagnetic Fe-rich clusters. Sánchez *et al* [53] identified in a disordered sample an AFM transition at about 770 K, which gives a superexchange strength comparable to that of LaFeO$_3$. The sample region with stoichiometric DP does not order at this temperature, but the ordering of the AFM clusters drag the magnetic moments of the surrounding Fe atoms. Similar speculation was raised by the double exchange treatment proposed in [69]. In [53] it is also shown that such an effect is absent in samples with AS < 16%. The AS threshold depends on whether the AFM clusters are large enough to maintain the coherence through the stoichiometric areas. Then, the long range ordering can be established in the DP phase at higher temperatures than in the case of completely ordered samples, as has been shown in samples having artificially enhanced Fe to Mo ratio [87, 88].

In practice, AS disorder is mainly controlled by the relative atomic radii of the B and B$'$ cations, which depends on both the atomic number and the valence state. Very different atoms are beneficial to the atomic ordering, whereas atoms with similar size and valence have more probability of occupying wrong sites. This was demonstrated in the case of the 25% doped Sr$_2$Fe$_{0.75}$T$_{0.25}$MoO$_6$ compounds (T = 3d transition metal) [67], as will be shown in section 2.2. Moreover, the AS can be varied systematically by means of different preparation conditions and thermal treatments [49]. In addition to the well-known M_S reduction predicted by equation (12), the presence of AS can induce subtle changes in the magnetic properties of double perovskites. For instance, significant AS disorder broadens the magnetic transition, increases the magnetic hardness and suppresses the mean field model characteristics of double perovskites [89, 90]. As a consequence, the T_C determination by means of the onset of the magnetic transition can be misleading. Indeed, this criterion indicates a moderate T_C increase for heavily disordered Sr$_2$FeMoO$_6$ samples [89], whereas the near-E_F photoemission spectra of the same samples unveils a reduced DOS at Fermi level, and the AS increase actually brings about a weakening of the ferromagnetic interaction [89, 91]. Therefore, one must take thoroughly into account the AS level when dealing with other properties of double perovskites which could likewise affect atomic ordering (such as electron doping, B–B$'$ off-stoichiometry, A site steric pressure, or different sintering conditions aiming to tailor the grain size).

In the following sections we will survey the influence of AS on the spin polarization and other transport properties in double perovskites. However, we anticipate that *ab initio* calculations have clearly shown that very low AS destroys the half-metallic character of the DOS [92, 93]. On the contrary, the half-metallicity is much more robust against oxygen vacancies, which preserve a P value close to -1 up to 16% of oxygen vacancies [93]. This is not surprising, given the key role played by the delocalized electrons and taking into account that each Fe–Mo antisite can remove up to ten B–O–B$'$ bonds, whilst each oxygen vacancy concerns a single B–O–B$'$ bond. Another expected effect of oxygen vacancies is the decrease of the saturation magnetization, since the strength of the indirect ferromagnetic coupling depends directly on the number of O 2p bridges coupling B and B$'$t$_{2g}$ states.

Antiphase boundaries (APB) in double perovskites can occur when there is a lattice shift equal to half a lattice parameter along a crystallite plane. This gives rise to a plane formed by antiferromagnetic Fe–O–Fe bonds or Mo–O–Mo bonds. This kind of defect is likely to appear in the coalescence region of two grains during sintering processes. In order to accommodate the AFM superexchange interaction at the Fe–O–Fe boundary and the long range ordered DP at both sides of the boundary, a kind of domain wall having parallel magnetic moments at both sides must appear [50]. Throughout such a domain wall, the Fe moments are misaligned, and therefore the appearance of Fe–O–Fe APBs will largely decrease the

saturation magnetization [94, 95]. APBs boundaries in DPs have been investigated by means of Mössbauer spectroscopy [50, 94], high resolution transmission electron microscopy [96, 97], and NMR measurements [98]. Very recently, combined TEM dark field images of the [111] superstructure peak and Lorentz microscopy have allowed observing that the magnetic domain walls become pinned at the antiphase boundaries [99].

1.6. Magnetoresistance effects

Due to the marked half-metallic character ($P = -1$) of the minority spin electrons lying at the $B(t_{2g}\downarrow)$–$O(2p)$–$B'(t_{2g}\downarrow)$ hybrid band, which are responsible for both the conduction mechanism and the ferromagnetic interaction, strong magnetoresistance effects are expected in the ferromagnetic phase of double perovskites. Hereafter we define the spin polarization, P, as:

$$P = \frac{N_\uparrow - N_\downarrow}{N_\uparrow + N_\downarrow} \tag{13}$$

where $N_{\uparrow(\downarrow)}$ is the density of occupied states per volume unit at the Fermi level in the majority (minority) spin sub-band. Thus, when one of the spin projected density of states is gapped at the Fermi level, $P = 1 (-1)$. In the case of many double perovskites such as $(Sr, Ca, Ba)_2FeMoO_6$, $(Sr, Ca, Ba)_2FeReO_6$, Sr_2CrReO_6 and $(Sr, Ca)_2CrWO_6$, it is theoretically predicted that $P = -1$, as shown in figure 4.

Further characterization of the spin polarization by means of the *tunnel magnetoresistance* (TMR) response in tunnel junctions with electrodes based on double perovskites has been frustrated by the difficulty to grow flat double perovskite thin films with high quality. Bibes *et al* [100] applied advanced lithography techniques to pattern nanosized tunnel junctions over sub-micrometric continuous SFMO islands grown by PLD. Their $SFMO/SrTiO_3/Co$ tunnel junctions exhibited a TMR = 50% at 4 K, which corresponds to $P = -0.86$ within Jullière's model [101]. High quality epitaxial SFMO with atomically smooth surfaces can be grown on $SrTiO_3(001)$ and (111) substrates, but the method calls for very high deposition temperatures (around 900 °C) and it is extremely sensitive to the deposition atmosphere (the oxygen partial pressure must be below 10^{-5} mbar) [102–104]. Therefore, most of the studies reported about the spin dependent transport in double perovskites were performed in polycrystalline ceramics. We will focus on the magnetoresistance properties of such specimens, which indeed raises the main interest of double perovskites for potential technological applications. The reason is that the magnetoresistive response concentrates at moderate magnetic fields (<1 kOe), which, together with the low manufacturing cost of DPs and their high T_C, makes these compounds very attractive for applications as magnetic field sensors and contactless potentiometers [105].

A number of irrefutable evidences point out that the MR in granular double perovskites arises from spin dependent scattering at the grain boundaries. The underlying conduction mechanism is electron tunnelling across insulating grain boundaries of the granular material. Double perovskites meet the two essential prerequisites for the TMR to occur in polycrystalline samples: $P \neq 0$ in the bulk grain and insulating grain boundaries small enough to allow tunnelling between grains. The magnetoresistance associated with tunnelling processes across grain boundaries will be named hereafter *intergrain tunnelling magnetoresistance* (ITMR) (there is not unanimity in the scientific community to refer to this effect). As it is strongly dependent on the microstructure, it is an *extrinsic* phenomenon. The simplest picture in order to explain the ITMR can be described as follows. An ensemble of grains separated by insulating grain boundaries can be viewed as a network of electrodes embedded in an insulating matrix. At the coercive field the overall magnetization of the material is zero and the magnetizations of the grains point randomly. According to the simplest TMR theory [101], this constitutes a

higher resistance state compared to the low resistance state achieved above the saturation field, when all the magnetizations of neighbouring grains are parallel. Hence, under the application of an external magnetic field, the sample undergoes a resistivity decrease as the magnetization approaches saturation. In order to give a theoretical approach to the functional dependence of the ITMR on the magnetic field, we make use of Inoue and Maekawa's [106] model for the ITMR of a set of monodisperse magnetic particles in an insulating matrix. This model is an extension of Slonczewski's model for the conductivity of a tunnel junction where the electrodes are forming an arbitrary angle [107]. Let m be the normalized magnetization of a polycrystalline sample whose grains do not interact magnetically between them. Then, Inoue and Maekawa's model yields the following expression for the conductivity:

$$G(H) = G_0(1 + P^2 m^2) \exp(-2\kappa s) \tag{14}$$

where G_0 is the conductivity in absence of spin polarization and within the limit $\kappa s \rightarrow 0$. κ^2 and s are respectively the representative barrier height and thickness to describe all the tunnel barriers formed at the grain boundaries of the sample. The interpretation of the κs exponent in equation (14) is different to that in [106]. In our case it is the averaged value of the exponential function throughout the whole sample, weighted by its corresponding probability function [108]. For instance, equation (14) would be exact if the barrier height and thickness are constant and equal to κ^2 and s respectively. Thus, if we assume that the barrier properties, say, the factor κs, are independent of the magnetic field, we can calculate from equation (14) the magnetoconductivity associated with the ITMR effect:

$$MC = \frac{\Delta G}{G(H=0)} = \frac{G(H) - G(H=0)}{G(H=0)} = (\text{ITMR}) = P^2 m^2. \tag{15}$$

Since the resistance can be defined as $R = 1/G$, one has the following alternatives to equation (15) in terms of magnetoresistance (MR):

$$\text{MR}_0 = \frac{\Delta R}{R(H=0)} = \frac{R(H) - R(H=0)}{R(H=0)} = (\text{ITMR}) = -\frac{P^2 m^2}{1 + P^2 m^2} \tag{16}$$

$$\text{MR}_h = -MC = \frac{\Delta R}{R(H)} = \frac{R(H) - R(H=0)}{R(H)} = (\text{ITMR}) = -P^2 m^2. \tag{17}$$

Each MR definition can be used depending on their convenience. In particular, MR_0 is useful when we want to add more contributions to the MR acting in series [108], whereas using MR_h it is easier to incorporate contributions in parallel [109]. We would like to remark that, in addition to bulk parameters such as P and m, the ITMR effect is strongly dependent on the extrinsic properties of the grains, such as their size, surface defects, impurities and/or grain boundaries nature, as will be shown later.

Yin *et al* [110] patterned a Wheatstone bridge straddling an artificial grain boundary in a SFMO epitaxial film grown on top of a SrTiO$_3$ bicrystal, which is shown in figure 7(a). Only two branches of the bridge cross the grain boundary. The 1000 Å epitaxial film showed metallic conductivity similar to the one reported for the single crystal [47], as well as a low saturation magnetization and remanence that are attributable to a large concentration of AS and APB. They showed a strong low field unbalance of the bridge when a magnetic field is applied, as displayed in figure 7(b). In spite of the large defect concentration, the two remaining branches without grain boundary only exhibit a negligible linear magnetoresistance. This fact demonstrates that the bridge unbalance is due to the ITMR effect taking place at the intersections of the Wheatstone bridge with the grain boundary, and that the bulk AS and APB defects only plays a minor role in the magnetotransport properties. Another solid proof of the origin of the low field magnetoresistance (LFMR) is the appealing work by Niebieskikwiat *et al* [111]. They monitor *in situ* the oxidation state of the grain boundaries in several polycrystalline
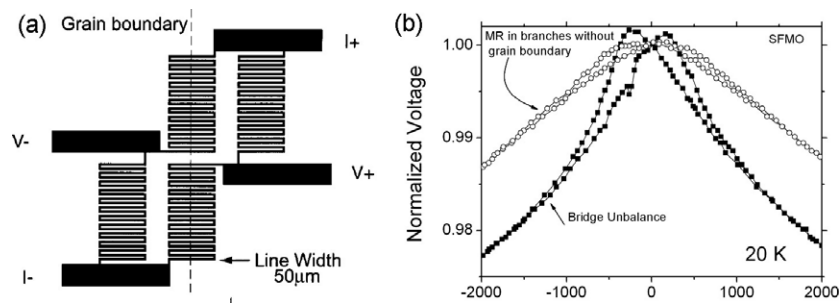
Figure 7. (a) Wheatstone bridge patterned in a 1000 Å SFMO epitaxial film [110]. The artificial grain boundary crosses only two branches of the bridge. (b) Comparison of the bridge unbalance (solid squares) and the magnetoresistance at the branches without grain boundary. The bridge unbalance is therefore due to the ITMR effect taking place at the grain boundary. Data taken from [110].

SFMO specimens, and change independently the AS level by means of different sintering temperatures. They demonstrate how the LFMR is set by the grain boundary conductivity and nature rather than by the Fe/Mo disorder. Along this line, Zhong *et al* have reported very recently a method to tune the quality of the insulating grain boundaries based on a sonochemical reaction with water which alters the $SrMoO_4$ content at the grain surface [112].

Yuan *et al* synthesized SFMO samples with nanometric grain size using the sol gel method [113]. They showed that the LFMR is gently enhanced on decreasing the average grain size from 45 to 29 nm. The MR increase is accompanied by a monotonic lowering of the conductivity as the grain diameter decreases. In other words, when the number of grain boundaries increases, the LFMR becomes much more pronounced. On the other hand, the AS-rich SFMO single crystal [47] does not show any noticeable LFMR. In conclusion, the above described results indicate that the ITMR effect arising from the spin dependent scattering at the insulating grain boundaries is responsible for the observed magnetoresistive response below the bulk magnetization saturation field, and rule out any influence of the intrinsic transport properties (apart from the prerequisite of a high spin polarization) and the AS disorder on the LFMR. However, one cannot exclude the spin dependent transport across antiphase boundaries (APB) as a plausible additional source of magnetoresistance. This effect has been carefully modelled by Eerenstein *et al* [114] in epitaxial Fe_3O_4 thin films and it brings about a linear magnetoresistance for magnetic fields larger than the uniaxial anisotropy field. However, this effect is only expected in samples with a substantial amount of APB, which correspondingly must show a reduced saturation magnetization. This can be the case of the epitaxial SFMO film in [110], where the magnetoresistance is found to be linear and very small at low fields ($\sim 1.2\%$ at 2 kOe), as depicted in figure 7(b). In contrast, the LFMR associated with the ITMR is present whenever the sample contains grain boundaries, and it shows a much more steep dependence on the magnetic field. One example can be found in [115], in which the $Ba_{1.6}Sr_{0.4}FeMoO_6$ compound exhibits a huge LFMR (see figure 8) in spite of its full saturation magnetization of $4\,\mu_B/$f.u.

Finally, we want to single out the existence of additional magnetoresistance mechanisms even in polycrystalline double perovskites having ideal structural and magnetic properties. In this review we will show that a linear MR above the bulk saturation field is often observed in double perovskites, which can be readily noticed in figure 8. According to the field dependence of the slope, the apparently linear behaviour can be related with several phenomena, such as the magnetic nature of the grain surface, the existence of magnetic impurities within the
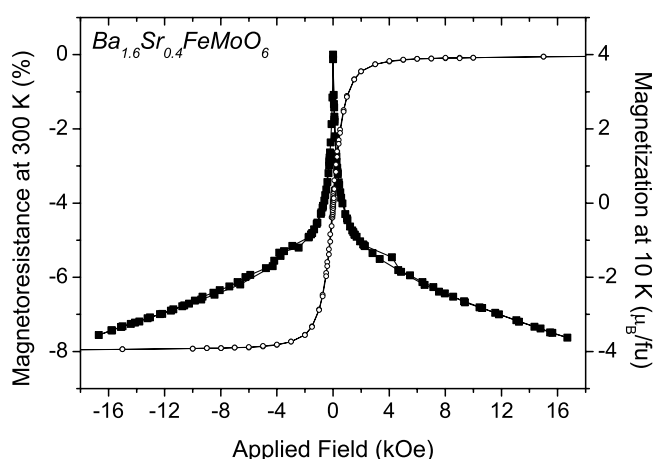
Figure 8. Magnetoresistance at room temperature (solid squares) and magnetization at 10 K (open circles) of $Ba_{1.6}Sr_{0.4}FeMoO_6$. The sharp resistance drop below 2 kOe, which is associated with the ITMR effect, is nicely seen. Above this field, a linear magnetoresistive response appears.

insulating grain boundaries, AS defects within the bulk grain [97], or other intrinsic sources of magnetoresistance [108].

2. FeMo-based double perovskites

2.1. A_2FeMoO_6

Good quality A_2FeMoO_6 double perovskites (A = Sr, Ca, Ba divalent cations or trivalent cations such as Nd or La) can be synthesized in the form of polycrystalline pellets. More difficulties have been found in the growth of single crystals [47, 116]. By varying the ionic content at the A site, two physical parameters of great importance for the ferromagnetic interaction can be modified in a controlled manner. One is the steric pressure at the A site, which can be used to tailor the structural parameters and crystallographic space group. As has been shown throughout sections 1.4 and 1.5, this internal chemical pressure exerted on the lattice can affect the magnetic interactions. The other one is the electron population at the Fermi level, which is mainly occupied by the Fe–O–Mo hybrid sub-band responsible for the indirect ferromagnetic coupling. In this section we survey the impact of these two parameters in the magnetic and magnetotransport properties.

We have already briefly discussed the impact of isovalent substitution using Sr, Ba and Ca atoms, which leads to moderate changes in the magnetic properties through structural modifications that vary the hybridization terms and the electronic band structure. In contrast, we will show that electron doping by means of La^{3+} or Nd^{3+} substitution gives rise to a robust increase of the Curie temperature. This kind of doping will also produce some associated steric and electronic volume effects. In order to give a true picture of the physical scenario, one cannot discuss the structural changes and the band filling influence separately. This is because in practice, it is very difficult to avoid the appearance of both effects simultaneously. There is the need to analyse carefully the possible reasons for the observed changes in the magnetic properties in terms of not only electron doping and steric effects, but also through other side effects such as antisite disorder, oxygen vacancies, off-stoichiometry, A cation size variance and segregation of secondary phases. In the next subsections we will develop a comprehensive study of the physical consequences of A cation substitution.

2.1.1. Steric effects.   The average atomic radius at the A site (r_A) provides a continuous abscissa to parametrize the cationic composition in A_2FeMoO_6 double perovskites (A = Ba, Sr, Ca). The phase diagram shown in figure 5 is well established, and displays how the monotonic decrease of the B–B$'$ distances strengthens the magnetic interaction and increases T_C in the $Ba_xSr_{2-x}FeMoO_6$ series, $0 < x < 2$. When further decreasing r_A in $Ca_xSr_{2-x}FeMoO_6$, the progressive bending of the Fe–O–Mo angle, produced by the gradual symmetry reduction, plays a more important part in the magnetic interaction than the $d_{B(B')-O}$ decrease. This results in an overall T_C reduction for $r_A < r_{Sr} = 1.44$ Å. The impact of the structural modification on the Fe oxidation state has been studied recently through the Fe K edge [58] and L_3 edge [57, 91] x-ray absorption spectra. The Fe atom is always in a 2+/3+ intermediate valence state, but in all the compounds the main resonance line is closer to the 3+ state, which might reflect the fact that most of the time the delocalized electron is located at the Mo 4d states. Whereas in the $A_2 = Sr_2$ and Ca_2 compounds the values of the Fe absorption edge are nearly the same, in the Ba_xSr_{2-x} compounds there is a chemical shift of the absorption edge towards the Fe^{2+} state and proportional to x. This is a proof of the close relationship between the electronic state and the hybridization strength (or equivalently, T_C), determined by the $d_{Fe(Mo)-O}$ distances and the Fe–O–Mo angle (see equation (11)). A similar trend regarding the Fe oxidation state as a function of r_A was reached by Mössbauer spectroscopy [50], although the quantification of the Fe valence is strongly dependent on the choice of the reference values for the Fe^{2+} and Fe^{3+} isomer shifts [48, 50].

Furthermore, the relationship between the ferromagnetic interaction and the Fe and Mo valence states has also been addressed by means of NMR measurements [10, 19, 117]. The hyperfine field of the Fe/Mo nuclei gives a measure of the magnetic moment on these ions. When going from Sr_2 to Ba_2, the authors in [117] observe a decrease of the Fe magnetic moment of $-0.2\,\mu_B$, which, in agreement with the XANES experiments [57, 58], corresponds to a valence state variation towards Fe^{2+}. But the main NMR result is the striking non-monotonic behaviour of the Mo resonance frequency as a function of r_A. Indeed, the behaviour of the magnetic moment at the Mo site mimics that of the Curie temperature for the whole A_2FeMoO_6 series, as depicted in figure 9. This fact can be understood within the first principles model expounded in sections 1.4 and 1.5. Combining equations (6) and (11),

$$T_C \propto V_{dpd\pi} \propto \frac{T(\omega)}{\langle d_{Fe-O}\rangle^4 \langle d_{Mo-O)}\rangle^4}. \tag{18}$$

In A_2FeMoO_6 the maximum Curie temperature is attained for $A_2 = Sr_2$ due to the balance of the numerator and denominator in equation (18). At the same time, this entails that the $Fe(t_{2g})$–$Mo(t_{2g})$ hybridization term, $V_{dpd\pi}$, is maximum for this compound. When replacing Sr by Ba or Ca, the $V_{dpd\pi}$ and T_C will jointly decrease owing to the $T(\omega)$ decrease (Sr to Ca) or to the increase of the interatomic distances (Sr to Ba). Then, it is straightforward that the charge depletion at the Fe site, and therefore the electronic population at the Mo $t_{2g}\downarrow$ band, has to be maximum when the Mo $t_{2g}\downarrow$ energy gain with respect to the Fermi level is optimized by the $V_{dpd\pi}$ hybridization term, that is to say, for the maximum Curie temperature. In good correspondence, all NMR, Mössbauer and XANES measurements to date evidence that μ_{Mo}, which arises exclusively from the delocalized electron, is proportional to T_C (see figure 9) [10, 50, 57, 82, 117].

In order to determine precisely the functional form of $T(\omega)$ from equation (18), one would have to collect T_C values against ω. Unfortunately, to our knowledge, there is no complete set of data correlating T_C and the structural parameters obtained by powder neutron diffraction for both the end compounds ($A_2 = Ba_2$, Ca_2) and intermediate compositions around Sr_2. There are lots of reports of the structure of particular compounds [18, 20, 33, 118], or even some
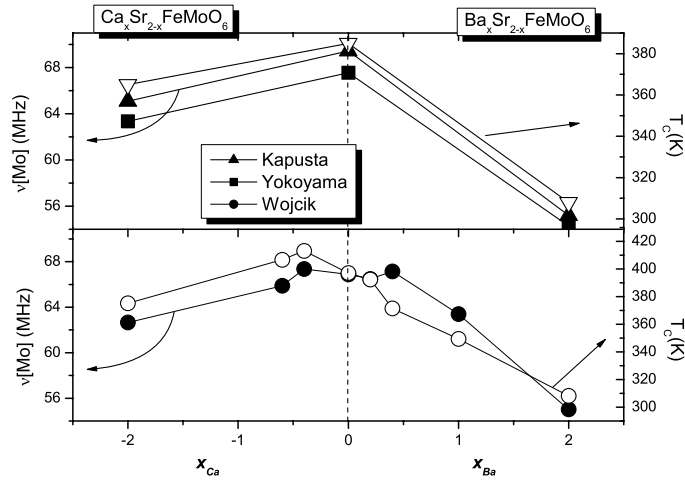
Figure 9. Resonance frequency of the ^{95,97}Mo NMR line in A_2FeMoO_6 (left axis) and corresponding Curie temperatures (right axis). Data are taken from [18] (empty triangles), [19] (solid triangles) and [10] (solid squares) in panel (a), and from [117] (circles) in panel (b). The absolute value of the magnetic moment at the Mo site is proportional to ν [Mo].

systematic studies as a function of the A cation composition in confined r_A regions [119, 120]. But the true picture would come only if all the samples belonged to the same batch, T_C were measured always with the same technique and the influence of defects such as AS disorder, oxygen vacancies and magnetic impurities were taken adequately into account.

The A site compositional substitution can induce local chemical inhomogeneities in the lattice. When different kinds of cations are present at the same crystallographic site, local distortions in $BO_6/B'O_6$ octahedra are created, and this distortion will propagate and eventually decay according to standard elasticity mechanisms. This kind of random quenched disorder creates random potentials and has been shown to have dramatic effects in critical phenomena, as for instance in the ferromagnetic and charge-ordering transitions in CMR manganites [121, 122] or superconducting transitions in oxide cuprates [123]. In a solid solution of cations at the A site, quenched disorder is quantified by $\sigma^2 = \langle r_A^2 \rangle - \langle r_A \rangle^2$, and calculated assuming a random probability distribution weighted by the A site stoichiometry. Sher *et al* addressed this topic in double perovskites through the series $Sr_{2-x}(Ca_{0.55}Ba_{0.45})_xFeMoO_6$ [124]. Since $r_A = 1.44$ Å for Sr and $r_A = 1.46$ Å for $Ca_{0.55}Ba_{0.45}$ [12], the average r_A is nearly constant and σ^2 varies linearly between 0 and 0.088 with x, $0 < x < 0.8$. They found a linear decrease of $T_C = T_C(x = 0) - 510 \times \sigma^2$ K, as well as an increasing magnetic softness given by $H_C = H_C(x = 0) - 700 \times \sigma^2$ Oe. However, due to the small r_A increase with x, one cannot isolate the effect of the increasing disorder and the slight steric pressure enhancement. Taking into account that r_A varies from 1.44 to 1.448 Å for $0 < x < 0.8$, the phase diagram shown in figure 5 yields an overall T_C decrease of 10 K due to steric effects. This only accounts for 20% of the observed T_C reduction, and therefore we can conclude from [124] that the A cation disorder gives rise to some intrinsic T_C decrease. However, the T_C decrease is probably overestimated, because the authors point out the use of different reducing synthesis conditions as a function of x, so that the unknown oxygen content might play an important role [85].

We have further investigated the steric pressure effect through the series $(Ba_{0.8}Sr_{0.2})_{2-x}$ $La_{2x/3}\#_{x/3}FeMoO_6$ ($x = 0, 0.1, 0.2, 0.3, 0.6$) [83], whose nominal composition is designed to

Table 2. Saturation magnetization, Curie temperature (measured with the Faraday balance), tolerance factor, lattice parameters, AS disorder, Fe/Mo–O distances and cubic hybridization parameter (see equation (18)) of $(Ba_{0.8}Sr_{0.2})_{2-x}La_{2x/3}\#_{x/3}FeMoO_6$. The structural parameters were determined from XRD at room temperature. The oxygen positions for $x = 0.6$ could not be refined, so that $a_{ps}/4$ is assumed to be the average Fe/Mo–O distance.

	$x = 0$	$x = 0.1$	$x = 0.2$	$x = 0.3$	$x = 0.6$
M_S (μ_B/f.u.)	3.98	3.77	3.61	3.29	2.39
T_C (K)	345	355	370	392	440
Space group	$Fm3m$	$Fm3m$	$Fm3m$	$Fm3m$	$P2_1/n$
f	1.0234	1.0119	1.0004	0.9889	0.9543
Lattice parameters (Å)	$a = 8.0342(1)$	$a = 8.0272(1)$	$a = 8.0198(1)$	$a = 8.0156(1)$	$a = 5.6556(6)$
					$b = 5.5921(6)$
					$c = 7.9881(9)$
AS (%)	0	5	7	8	23
d_{Fe-O} (Å)	2.0635(10)	2.0156(6)	2.0298(8)	2.0167(3)	1.9987(9)
d_{Mo-O} (Å)	1.9545(10)	1.9985(10)	1.9801(8)	1.9911(3)	1.9987(9)
$(d_{Fe-O} \times d_{Mo-O})^{-4}$ (au)	3.79	3.80	3.83	3.85	3.93

vary r_A without any kind of electron doping, despite the presence of La^{3+} ions. One readily sees that for each added electron, the divalent cation vacancy, denoted as #, promotes one hole, leading to no nominal doping at all. This assures that the synthesis routes are the same as in the case of other electron doped series (which will be reviewed in the next subsection). Analysis of the combined XRD and magnetization measurements experimentally demonstrates that no electron doping occurs in this series [83]. The magnetic and structural properties at room temperature are summarized in table 2. The lattice parameters decrease linearly from $x = 0$ to $x = 0.6$ as a result of the r_A reduction. We point out that significant electron doping would give rise to an enhancement of the volume state [125, 126]. T_C was obtained as the extrapolation down to zero of the line parallel to the magnetization versus temperature curve at the temperature in which the derivative is maximum, as illustrated in figure 10(a). As predicted by equation (18), figure 10(b) evidences that T_C depends linearly on the ppd–π hybridization terms which overlap Fe and Mo t_{2g} through O $2p_\pi$ oxygen states. The pdd–π calculation was done from the interatomic distances listed in table 2. On the other hand, if the variance was to play the same role as in [124], T_C would decrease from 345 K for $x = 0$ to 234 K for $x = 0.6$. This is completely incompatible with the observed results, so that it is clear that either the σ^2 variation plays a minor role when other structural parameters are varied or the σ^2 cannot be quantified in the same way.

2.1.2. Electron doping effects. Aiming to combine the large ITMR ratios with the highest possible Curie temperature, the strategy of electron doping at the Fermi level has often been tested. Electron doping is achieved in double perovskites replacing divalent cations by trivalent rare earths at the A site. This kind of doping was first shown to be effective in order to increase T_C in $Sr_{2-x}La_xFeMoO_6$ [127] ($T_C = 425$ K and 490 K for $x = 0$ and $x = 1$ respectively). In addition to numerous works dealing with La and Nd doping in A_2FeMoO_6 [115, 118, 120, 125, 126, 128], trivalent doping in $A_{2-x}La_xCrWO_6$ also results in a strong T_C increase [129, 130]. Thus, the strengthening of the ferromagnetism on electron doping is a general characteristic of high Curie temperature double perovskites (at least up to a certain doping level). This is not surprising because as La^{3+} replaces the divalent cation, a net electron doping at the Fermi level takes place. Consequently, the higher band filling increases
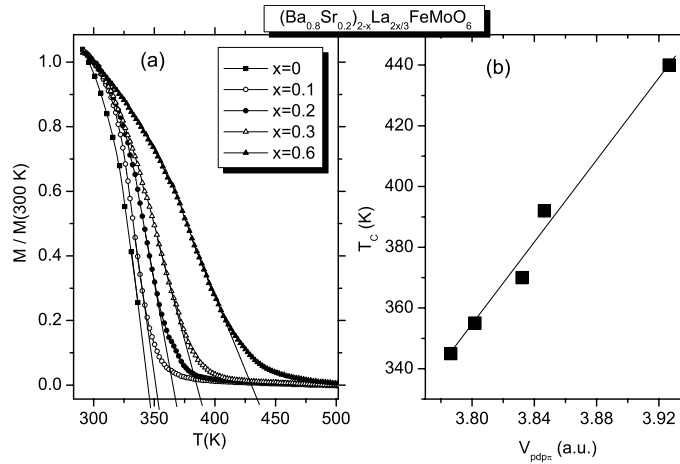
Figure 10. (a) Magnetization as a function of the temperature for $(Ba_{0.8}Sr_{0.2})_{2-x}La_{2x/3}$#$_{x/3}FeMoO_6$ measured with the Faraday balance. For a better comparison, the magnetization has been normalized by its value at 300 K. (b) Curie temperature dependence on the $Fe(t_{2g})$–$Mo(t_{2g})pd\pi$ hybridization terms.

the DOS at the Fermi level, which would optimize the Fe/Mo double exchange mechanism by analogy with the scenario in manganese perovskites [55]. Near-E_F valence band photoemission spectra recorded in *in situ* broken or scraped samples have revealed that, in fact, the density of occupied states at the Fe–Mo $t_{2g}\downarrow$ hybrid sub-band increases linearly with the doping level, x [131–133]. The opposite effect, consisting in a reduced photoemission intensity near E_F, has been recently observed in hole doped $K_xSr_{2-x}FeMoO_6$ double perovskites [134].

In the following we survey the impact of trivalent rare earth doping on the magnetic and structural properties, as well as the role played by the accompanying DOS increase at the Fermi level. We have selected the parent compound $(Ba_{0.8}Sr_{0.2})_2FeMoO_6$ (BSFMO) for the assessment of La doping. This compound shows the lowest saturation field and largest room temperature ITMR ratio [115, 77, 135, 136]. First, if we look at the phase diagram of A_2FeMoO_6 (see figure 5), for $r_A = 0.8r_{Ba} + 0.2r_{Sr} = 1.576$ Å, the r_A decrease on La doping ($r_{La} = 1.36$ Å [12]) will give rise to a T_C increase by reducing the Fe(Mo)–O distances, provided that the structure remains cubic. This holds true up to a doping level 65% of La, for which $r_A = 1.44$. Second, the electron doping will raise the occupation of the Fe(Mo) t_{2g} spin down sub-band, responsible for the hybridization mechanism, which is also beneficial for the stabilization of ferromagnetism at higher temperatures. Therefore, we have performed a careful structural, magnetic and transport study of the series $(Ba_{0.8}Sr_{0.2})_{2-x}La_xFeMoO_6$, with $x = 0$, 0.2 and 0.4. X-ray diffraction and neutron powder diffraction indicate that the three studied samples are cubic ($Fm3m$) and single phase. From the value of the relative intensity of the (111) superstructure peak, we conclude that the Fe/Mo ordering is very high and not affected by La doping. If we force some Fe/Mo disorder (AS $\approx 4\%$) in the Rietveld refinement, the fits do not show any significant improvement or they worsen. Refinements of the neutron diffraction data at 500 K also support the perfect Fe/Mo ordering. If we allow the Fe/Mo/O content to vary in the refinement, we find the stoichiometries listed in table 3, which are very close to the nominal ones.

In figure 11(a) the temperature dependence of the intensity of the (111) and ($\bar{1}$11) magnetic Bragg peaks obtained from the neutron diffraction data in D1B (ILL, Grenoble, France) is

Table 3. Stoichiometry, structural parameters at 4 K, saturation magnetization at 5 K and 5 T, and Curie temperature of $(Ba_{0.8}Sr_{0.2})_{2-x}La_xFeMoO_6$. Structural information was obtained from high resolution neutron diffraction profiles taken at 4 K in D2B. The Curie temperature is measured as the onset of the temperature dependence of the magnetic scattering intensity in thermodiffractograms recorded at D1B. The cubic hybridization parameter according to equation (18) is included.

Nominal A_2	$Ba_{1.6}Sr_{0.4}$	$Ba_{1.44}Sr_{0.36}La_{0.2}$	$Ba_{1.29}Sr_{0.32}La_{0.4}$
BB'	$Fe_{1.00(1)}Mo_{1.01(2)}$	$Fe_{1.02(1)}Mo_{1.03(2)}$	$Fe_{1.03(1)}Mo_{1.00(2)}$
Oxygen content	5.89(6)	5.99(6)	5.99(5)
a (Å) 4 K	8.021 39(3)	8.010 67(4)	8.000 22(6)
d_{Fe-O} (Å)	2.0597(36)	2.0527(40)	2.0477(40)
d_{Mo-O} (Å)	1.9510(35)	1.9527(39)	1.9525(39)
f	1.0234	1.0159	1.0085
M_S (μ_B/f.u.)	3.98	3.84	3.40
T_C (K)	345	378	405
$(d_{Fe-O} \times d_{Mo-O})^{-4}$ (au)	3.83	3.87	3.91

shown. This kind of measurement provides a microscopic tracking of the evolution of the long range magnetic ordering as an extra magnetic contribution to the integrated intensity of structural Bragg peaks ((111) in this case). Whilst T_C is 345 K for $x = 0$, it increases to 378 K for $x = 0.2$ and to 405 K for $x = 0.4$. The change in T_C is huge, 3 K per % of La at the A site, and much higher than in the case of La doping in Sr_2FeMoO_6, 1.3 K per % of La at the A site [131]. The origin of this enhanced T_C increase can be found in the cooperative effect of both the steric pressure and electronic band filling with La doping towards higher T_C. Taking into account the known impact of r_A on T_C (see again figure 5) we estimate that half of the effect could arise from structural effects owing to the r_A decrease with La doping from 1.58 Å for $x = 0$ to 1.53 Å for $x = 0.4$. This is reflected in the increase of the hybridization parameter defined in equation (18) (see table 3). The other contribution to the T_C enhancement would come from the doping itself through the band filling optimization.

In figure 11(b) the magnetization isotherms at 5 K are shown. For the parent compound BSFMO, the measured magnetization (3.98 μ_B/f.u.) is the expected one in absence of Fe/Mo disorder. This correlates perfectly with the structural data from x-ray and neutron diffraction that indicated the complete Fe/Mo ordering. The low saturation field ($\sim$1 kOe) of this compound is also remarkable, as already observed in [77]. On La doping, the saturation magnetization is still rather high, as shown in table 3. Valence band photoemission experiments have proved that the extra electron provided by each La ion goes into the minority spin sub-band lying at the Fermi level [131, 133]. In consequence, in the ideal case without AS disorder, one would expect magnetic moments of 3.8 and 3.6 μ_B/f.u. for $x = 0.2$ and 0.4 respectively. The small discrepancy between the experimental and the theoretical values can be explained by a certain off-stoichiometry at the A site, which would be beyond our experimental resolution. Nevertheless, the decrease of M_S whilst AS remains unnoticeable confirms the efficiency of electron doping, as well as the antiparallel coupling of the itinerant electrons with the Fe core moment.

Electron doping has a dramatic effect on the electronic state of the Mo atom, which is naturally explained by the fact that the spin down conduction band near the Fermi level is dominated by the Mo(4d) $t_{2g}\downarrow$ [44]. The evolution of the Fe–Mo magnetic moment, as a function of the electron doping was first addressed by Moritomo *et al* [137]. Their neutron diffraction experiments show a μ_{Mo} enhancement in absolute value with the doping level, which indicates the preferential occupation of the Mo orbitals. Since the spin magnetic moment is the only source of hyperfine field in Mo, the ^{95,97}Mo NMR resonance frequency is an excellent

probe for the μ_{Mo} evaluation. Using this technique, it has been uncontroversially shown that on electron doping in double perovskites ($Sr_{2-x}La_xFeMoO_6$ [82], $Ca_{2-x}Nd_xFeMoO_6$ [118], $Ba_{1+x}Sr_{1-2x}La_{2x}FeMoO_6$ [81], and $(Ba_{0.8}Sr_{0.2})_{2-2x}La_xFeMoO_6$ [138]), a spin down polarized carrier injection takes place mainly into the Mo t_{2g} states. In all the mentioned series there is a T_C increase concomitant to the Mo electron uptake. Therefore, the exchange splitting of the up and down sub-bands due to the hopping mechanism is reinforced by the electron doping, as expected in a double exchange-like scenario. However, the site selective electron doping triggers the appearance of antisite defects in lanthanide doped double perovskites. The reason is that the induced intra-atomic electronic repulsion raise in the Mo atom gives rise to a net MoO_6 volume gain. Prior to the doping, the volume of the MoO_6 octahedra is smaller than that of the FeO_6 octahedra (see for instance [18]), which favours the Fe/Mo ordering. The electronic doping promotes an approach of the FeO_6 and MoO_6 octahedra volumes, from which the B and B' crystallographic sites become homogenized and the Fe/Mo atomic disorder comes out [67]. Such an effect is illustrated in figure 1: in Ba-rich compounds such as $(Ba_{0.8}Sr_{0.2})_{2-x}La_xFeMoO_6$ [115] and $Ba_{2-x}La_xFeMoO_6$ [128], the MoO_6 and FeO_6 octahedra volumes of the undoped compounds ($x = 0$) are more unlike each other than in compounds with smaller r_A (see figure 12(b)). Thus, if follows that when the MoO_6 octahedra volume is further enhanced on electron doping, the AS disorder is developed at a much larger extent in series with pristine Sr- or Ca-rich compounds (see figure 12(a)).

The promotion of AS disorder on Lanthanide doping [53, 69, 89], and the steric effect that accompanies every A site atomic substitution, can mask the true impact of electron doping in double perovskites. In order to solve this uncertainty, there have been two experimental reports in which it is evidenced that the T_C increase is a genuine effect associated with electron doping. One is the result concerning the series $Ca_{2-x}Nd_xFeMoO_6$ [118]. In brief, Ca replacement with Nd does not alter significantly r_A due to the similarity between their average ionic radius in coordination XII [12] (1.34 Å for $A_2 = Ca_2$ and 1.312 Å for $Ca_{1.2}Nd_{0.8}$). In spite of the small r_A reduction, the cell volume is gently enhanced from 0.230 nm^3 for $x = 0$ to 0.236 nm^3 for $x = 0.8$. This is due to the electronic volume effect occurring at the MoO_6 octahedra. If one calculates the average Fe–Mo distance as in figure 2 (i.e., as one half of a_{ps}), the B–B' distance increases ∼0.8% when going from $x = 0$ to $x = 0.8$. Taking into account the structural relationship between such a distance and r_A reported in figure 2 (bottom panel), this corresponds to an effective r_A enhancement from 1.34 Å to approximately 1.36 Å for $x = 0$ and 0.8 respectively. This effective r_A shift in the phase diagram shown in figure 5 cannot account for the large T_C increase in $Ca_{2-x}Nd_xFeMoO_6$ of 60 K between $x = 0$ and $x = 0.8$ [118]. Therefore, the intrinsic T_C increase on electron doping describes correctly the physical picture of FeMo double perovskites.

However, the authors in [118] recognize that the growing presence of AS defects in $Ca_{2-x}Nd_xFeMoO_6$ (as high as 32% for $x = 0.8$; see the top panel of figure 12) is troubling. As already mentioned, one should work with larger r_A values in order to avoid this problem. That is the case in the series with nominal composition $Ba_{1+x}Sr_{1-2x}La_{2x}FeMoO_6$ [126]. In the following we will review this second experimental report that not only unambiguously proves the intrinsic nature of the T_C raise on electron doping, but also demonstrates the dominant character of the band filling effects. In the aforementioned series with $x = 0$, 0.1, 0.2 and 0.3 (for obvious reasons doping is feasible only up to $x = 0.33$), the steric effects are minimized and electron doping at the conduction band is achieved. For XII coordination, the ionic radii of Ba^{2+}, Sr^{2+} and La^{3+} are respectively 1.61, 1.44 and 1.36 Å [12]. The average $r_A = 1.525$ Å corresponding to the parent compound does not change if the Sr ions are replaced by one third of Ba ions and two thirds of La ions.

26

Table 4. Stoichiometry (refined at 700 K) and structural parameters (refined at 2 K) of $Ba_{1+x}Sr_{1-3x}La_{2x}FeMoO_6$ obtained from high resolution neutron diffraction data taken at D2B. All the samples can be indexed in the $Fm3m$ space group and remain cubic down to the lowest temperature. Data labelled with star ($*$) are obtained from refinements of the XRD patterns at room temperature. Curie temperature measured with the Faraday balance and saturation magnetization at 5 K–5 T are also included.

Refined stoichiometry (700 K)	BaSr [Fe_{0.95(1)}] [Mo_{0.97(1)}]O_{5.84(3)}	Ba_{1.11(5)}Sr_{0.71(5)}La_{0.20(5)} [Fe_{0.90(3)}Mo_{0.10(3)}][Mo_{0.90(3)}Fe_{0.10(3)}] O_{5.84(3)}
a (Å)	7.9272(4)	7.9869(5)
x_{O1}	0.2532(9)	0.2549(6)
d_{FeO} (Å)	2.008(8)	2.036(5)
d_{MoO} (Å)	1.956(8)	1.957(5)
μ_{Fe} (μ_B)	4.32(8)	3.97(7)
μ_{Mo} (μ_B)	0.06(10)	−0.27(8)
T_C (K)	362	372
M_S (μ_B/f.u.)	3.90	3.35
a^* (Å)	7.9813(8)	7.994(1)
AS* (%)	3(2)	8(2)
$(d_{FeO} \times d_{MoO})^{-4}$	4.2	3.96
Nominal A_2 Refined BB′ (700 K)	Ba_{1.2}Sr_{0.4}La_{0.4} [Fe_{0.91(4)}Mo_{0.09(4)}][Mo_{0.91(4)}Fe_{0.09(4)}]	Ba_{1.3}Sr_{0.1}La_{0.6} [Fe_{0.90(7)}Mo_{0.10(7)}][Mo_{0.90(7)}Fe_{0.10(7)}]
a (Å)	8.0024(3)	8.0280(5)
x_{O1}	0.2523(21)	0.2527(19)
d_{FeO} (Å)	2.019(17)	2.029(15)
d_{MoO} (Å)	1.982(17)	1.985(15)
μ_{Fe} (μ_B)	4.14(8)	4.25(10)
μ_{Mo} (μ_B)	−0.21(10)	−0.31(11)
T_C (K)	390	401
M_S (μ_B/f.u.)	2.93	2.04
a^* (Å)	8.0054(4)	8.0268(7)
AS* (%)	10(3)	16(3)
$(d_{FeO} \times d_{MoO})^{-4}$	3.9	3.8

We think that this kind of doping can be an effective way to reduce the steric effects, whilst La doping assures an increase in the number of conduction electrons. The structural properties were studied by means of x-ray diffraction and neutron powder diffraction at D2B (ILL, Grenoble). The lattice parameters as a function of La doping, obtained from fits of the x-ray and neutron diffraction patterns, are listed in table 4. We notice that, contrary to the expectation, the lattice parameter is not constant across the series but a slight increase is observed on doping. This unexpected increase can be understood in terms of the expected slight volume cell increase on electron doping (see figure 12(b) and [126, 118]), as occurs in manganese oxides [139]. By refinement of the XRD diffractions patterns, the actual amount of AS has been determined and it is listed in table 4. Beyond the error bars, a moderate increase of AS with doping is observed, in agreement with the previous discussion. The performed doping and the increasing presence of AS have a strong impact on the magnetization value as shown in figure 13(a). First, one can notice that for the undoped compound ($x = 0$), the saturation magnetization, 3.9 μ_B/f.u., is slightly below the expected value when no AS defects are present, 4 μ_B/f.u. As observed in inset of figure 13(a), the saturation magnetization strongly decreases with x. This decrease is attributed to two different effects. First, due to the antiparallel coupling of the added electron with the local magnetic moment, M_S will diminish
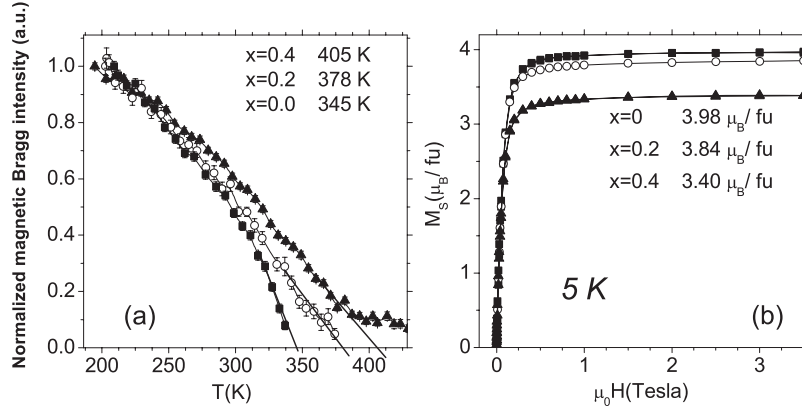
Figure 11. (a) Temperature dependence of the magnetic Bragg intensity normalized to its value at 200 K for $(Ba_{0.8}Sr_{0.2})_{2-x}La_xFeMoO_6$ with $x = 0$ (solid squares), $x = 0.2$ (open circles) and $x = 0.4$ (solid triangles). The corresponding Curie temperatures are listed. (b) Magnetization at 5 K versus applied magnetic field. The corresponding saturation values are listed.

according to the dependence $[5 - (1 + 2x)]$ μ_B/f.u. Second, the presence of AS reduces the magnetization as given by equation (12). However, the impact of the simultaneous presence of AS disorder and electron doping on the magnetization is controversial. As long as the gap at the Fermi level in the spin down conduction band is preserved, every added electron will contribute with -1 μ_B/f.u., even in presence of AS. Hence, equation (12) transforms to:

$$M_S = 4 - 2x - 8w \ \mu_B/\text{f.u.} \tag{19}$$

But it has been shown that AS disorder gradually destroys the half-metallic character of the electronic structure [92, 93]. For instance, *ab initio* calculations show that for a crystal structure with AS = 25%, the DOS retains a negative spin polarization of only $\sim$33% [92]. In the limit of AS = 50%, the spin polarization should vanish. An alternative way to equation (19) to allow for this effect is to assume that every antisite promotes an available spin up state at the conduction band. Then, as done in the case of $Sr_{2-x}La_xFeMoO_6$ [131], equation (12) transforms to:

$$M_S = (4 - 2x)(1 - 2w). \tag{20}$$

Since the loss of spin polarization per antisite is unknown, and certainly AS does not give rise to a magnetic arrangement having the Fe and Mo moments fully antiparallel to their respective directions in the regular sites, we can adopt equation (20) as the theoretical upper limit for $M_S(w, x)$, whereas equation (19) would be the lower bound of $M_S(w, x)$. If we apply the latter formula using the experimentally inferred AS and the nominal electron doping, we find a good quantitative agreement with the observed M_S (see the inset in figure 13(a)). This means that electron doping was achieved and it is very close to the nominal one. We remark that NMR [81] and neutron diffraction experiments in the same samples yielded consistent values of AS with those ones derived from XRD.

According to the small decrease of $V_{dpd\pi} \sim (d_{FeO} \times d_{MoO})^{-4}$ listed in table 4, the phase diagram shown in figures 5 and 10(b) foresees a slight decrease of T_C with doping in this series. However, this conflicts with the main finding for this series shown in figure 13(b). A strong increase of T_C with doping is found from the temperature dependence of the magnetization around the ferromagnetic transition. The T_C raise per added electron in a formula unit amounts to about 70 K. In other words, T_C increases 0.7 K/% La at the A site. We would like to remark
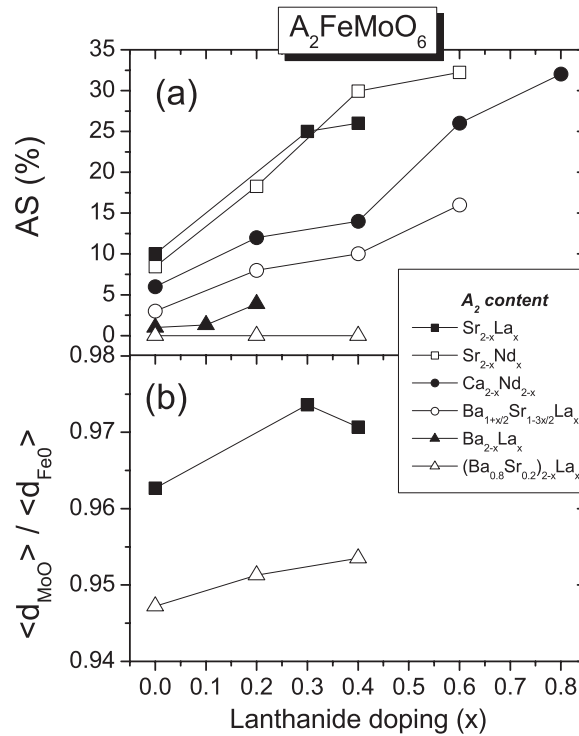
Figure 12. (a) Antisite disorder as a function of the Lanthanide doping at the A site of several A_2FeMoO_6 electron doped series. (b) Length scale mismatch of the MoO_6 and FeO_6 octahedra, calculated as the average Mo–O distance over the average Fe–O distance. Data has been taken from [120] (solid squares), [125] (open squares), [118] (solid circles), [126] (open circles), [128] (solid triangles) and [115] (open triangles).

that this increase in T_C cannot be attributed to having strong Fe/Mo disorder. In fact, Sánchez *et al* have observed that Sr_2FeMoO_6 samples with AS $\sim$ 16% do not show any noticeable increase of T_C due to AS disorder [53]. As a consequence, AS disorder can be ruled out as a source of the observed T_C increase in our samples. It has been discussed how different methods and criteria used to determine T_C influence its value [89]. In this sense, we would like to underline that the T_C estimates from the two methods employed throughout the experimental review in this section are equivalent, and therefore, their T_C values can be safely compared. Let T_C be the value extracted from the extrapolation down to zero of the maximum slope of the magnetic signal around the transition temperature. The so defined T_C resulting from the temperature dependence of both the D1B magnetic Bragg intensity and the magnetization agree perfectly. In summary, neither the steric effect of the variation of the BB′ distance upon the magnetic interaction, nor the moderate AS degree ($\leqslant$16%) can account for the large T_C raise. Once these effects have been discarded, the plausible scenario is that the increase of the number of conduction electrons promoted by La doping enhances the hopping mechanism proposed by Sarma [42] and Kanamori [64] (see section 1.3). It seems that this sort of double exchange-like mechanism strengths up to the studied doping level (0.6 conduction electrons per formula unit).

In the three series presented in this section, there are two competing physical parameters that influence the ferromagnetic ordering temperature. One is, for sure, the nominal electron doping, which cannot be accurately measured because not all the stoichiometries at the
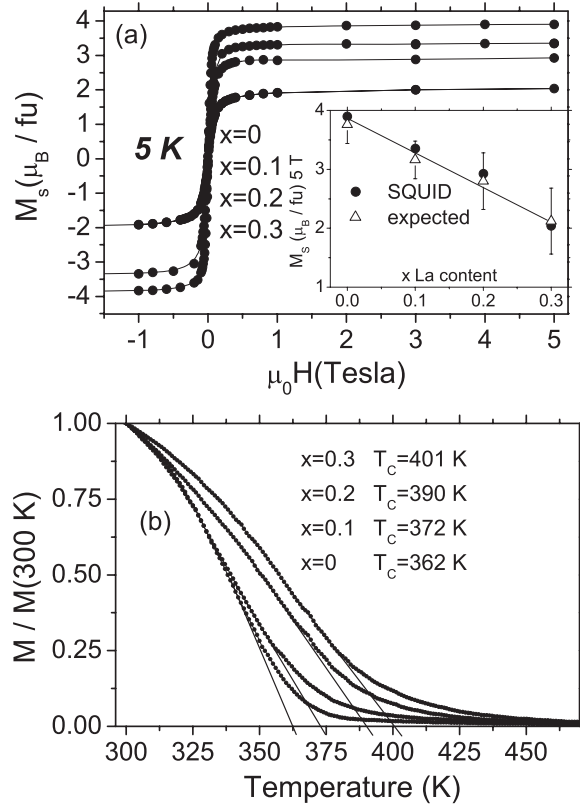
Figure 13. (a) SQUID magnetization isotherms at 5 K in $Ba_{1+x}Sr_{1-3x}La_{2x}FeMo_6$. The inset shows the comparison between the experimental MS and the corresponding inferred values taking into account AS and the nominal electron doping. (b) Magnetization as a function of the temperature for all the studied compounds measured with the Faraday balance. For better comparison, the magnetization has been normalized by its value at 300 K. T_C appears correspondingly listed as a function of doping.

A site could be refined in the structural analysis. However, the good agreement between the experimental and the expected saturation magnetization, leads us to think that the nominal stoichiometry provides a good approach to the actual electron doping (see [83], figures 11(b) and 13(a)). If n_e is the number of carriers at the Fermi level per formula unit,

(1) $A_2 = (Ba_{0.8}Sr_{0.2})_{2-x}La_x \rightarrow n_e = 1 + x$

(2) $A_2 = Ba_{1+x}Sr_{1-3x}La_{2x} \rightarrow n_e = 1 + 2x$

(3) $A_2 = (Ba_{0.8}Sr_{0.2})_{2-x}La_{2x/3}\#_{x/3} \rightarrow n_e = 1.$

The other parameter is the structural effect produced by the variation of the steric pressure at the A site. In particular, the relative position of Fe, Mo and O atoms in the unit cell determines the strength of the hopping interaction that stabilizes the ferromagnetism in the B sublattice. In the model elaborated in section 1.5, we have seen that the suitable physical parameter to describe this interaction is $V_{dpd\pi}$. In the above mentioned series, the structure remains cubic for all the compounds except for the sample with $x = 0.6$ of series number three. For this sample the tetragonal distortion (see equation (2)) amounts only to 0.0015. Therefore, the Fe–O–Mo angle is approximately 180° and, consequently, the hopping interaction strength will be given uniquely for all the three series by the dependence of $V_{dpd\pi}$ on the $d_{Fe/Mo-O}$ distances, as
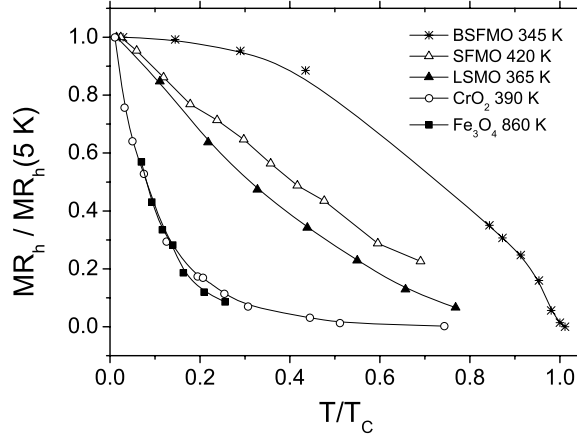
Figure 14. ITMR contribution to the magnetoresistance in several candidates to half-metallic materials. In the legend the Curie temperature of each compound is shown. Data taken from: [144] for Fe_3O_4, [142] for CrO_2 [140] for $La_{2/3}Sr_{1/3}MnO_3$ (LSMO), and this work for Sr_2FeMoO_6 and $(Ba_{0.8}Sr_{0.2})_2FeMoO_6$.

shown in equations (6) and (11). As already mentioned, the value of $V_{dpd\sigma}$ in these compounds becomes meaningless, because the e_g levels are empty (see figure 3). The slope of $T_C(n_e)$ is 150 K/(e^-/fu) for series one and 67 K/(e^-/fu) for series two. This is because in the former, the band filling and the steric pressure contribute to the T_C raise on La doping, whereas in series number 2 the electron doping must overcome the decrease of the hybridization terms. Thus, in series 2 the trend to increase T_C due to band filling predominates over the structural effects. In series number 3, for which the band filling is nominally zero, the T_C increase should be solely ascribed to the impact of the smaller r_A through the $V_{dpd\pi}$ enhancement. In summary, from the experimental study of series 1–3, we can conclude that:

- Electron doping at the Fermi level always increases T_C.
- The Curie temperature depends linearly on the matrix elements of the atomic potential mixing the t_{2g} levels of the Fe and Mo cations through the O 2p states. These matrix elements can be changed in a controlled manner by means of the steric pressure at the A site.
- When both effects compete, as in the case of series number two, the electron doping overcomes the structural effect. A similar conclusion was reached in the work by Frontera *et al* [120].

2.1.3. Magnetoresistive properties. The search for magnetic materials with a high degree of spin polarization and T_C well above room temperature is a key issue in the field of magnetoresistive sensors and non-contact potentiometers. Oxide materials might offer opportunities in these applications. In this sense, the scores obtained in ITMR with manganites and CrO_2 do not suffice for actual applications. For example, the maximum $T_C = 365$ K in CMR manganites was observed in $La_{2/3}Sr_{1/3}MnO_3$ [140], while in the case of CrO_2 T_C amounts only to 390 K [141, 142]. However, the room temperature ITMR rates in polycrystalline specimens have been reported to be quite modest, typically below 1% [140, 142–144] at fields not greater than 1 T. Large low field magnetoresistance was found in the double perovskite Sr_2FeMoO_6 (SFMO), which was explained in terms of ITMR [11, 113]. Following the definition in equation (17), $MR_h(300 \text{ K}, 1 \text{ T}) = 5.5\%$ and $MR_h(5 \text{ K}, 1 \text{ T}) = 24\%$ for
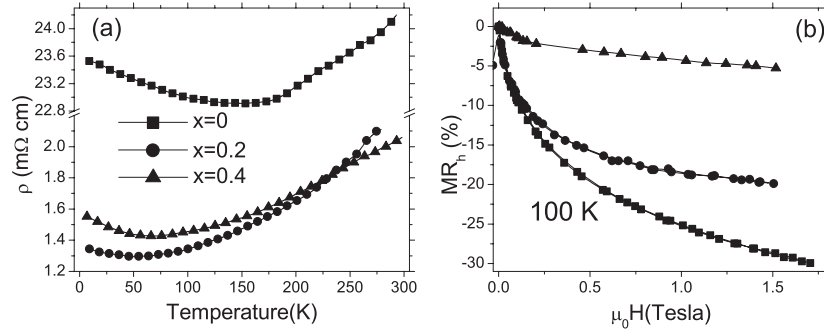
Figure 15. (a) Temperature dependence of the resistivity of $(Ba_{0.8}Sr_{0.2})_{2-x}La_xFeMoO_6$ for $x = 0$ (solid squares), $x = 0.2$ (solid circles) and $x = 0.4$ (solid triangles). Note the break in the ordinate axis. (b) Magnetoresistance isotherms at 100 K.
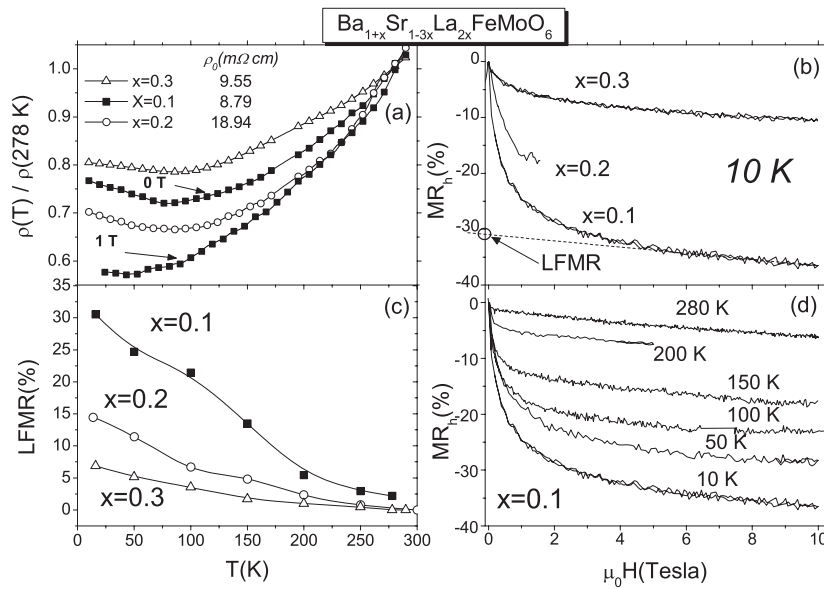

Figure 16. Magnetotransport properties of $Ba_{1+x}Sr_{1-3x}La_{2x}FeMoO_6$ for $x = 0.1$ (solid squares), $x = 0.2$ (open circles) and $x = 0.3$ (open triangles). (a) Resistivity normalized by its value at 280 K. For $x = 0.1$ the curve under zero and 1 T applied field are shown. The residual resistivity at 10 K, ρ_0, is listed. (b) Magnetoresistance isotherms at 10 K. (c) Temperature dependence of the low field magnetoresistance (LFMR) as defined in (b). (d) Magnetoresistance of the $x = 0.1$ sample at selected temperatures.

SFMO. This fact, together with the fairly large $T_C = 420$ K of SFMO, triggered the interest for double perovskites as they were expected to meet the suitable standards to achieve stable and large ITMR well above room temperature. According to equation (17), as the temperature is raised, a decrease of the ITMR is expected due to the reduction of both P and m^2. The gradual population of excited states reduces P as the ground state becomes depopulated, and the thermal energy gain permits the occupation of equilibrium states with lower mean M_S, diminishing m^2.

A serious drawback in the aforementioned half-metals is the fast decrease of $MR_h(T)$ as the temperature increases. This decrease was much faster than the one foreseen by the scaling
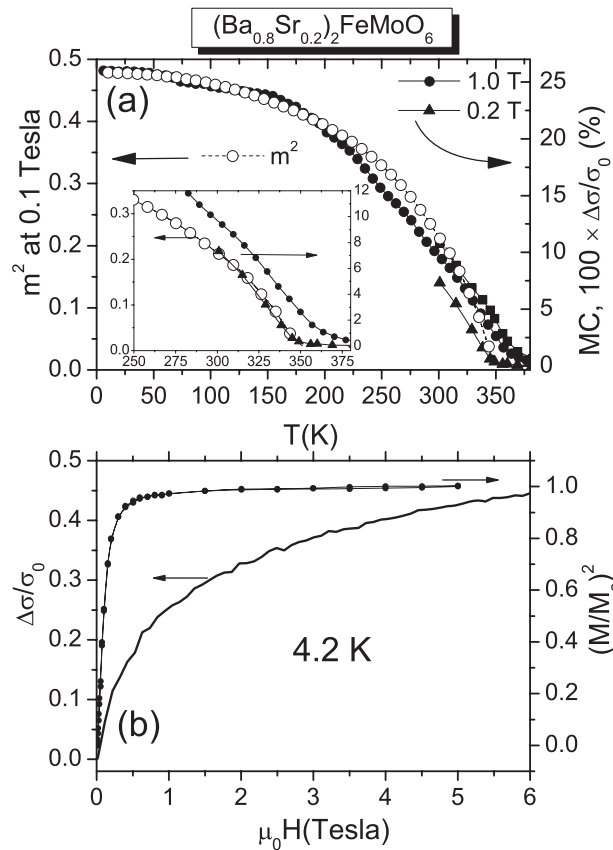
Figure 17. (a) Scaling law of the squared magnetization of $(Ba_{0.8}Sr_{0.2})_2FeMoO_6$, together with the magnetoconductivity. Inset: magnetization of the region close to T_C. It shows that the low field magnetoresistance occurs exactly at T_C. (b) Comparison of the magnetoconductivity and the squared magnetization isotherms at 4.2 K.

law for ITMR (see equation (17)), $P^2m^2 = P^2(M(T, H)/M_S(0\ K))^2$. The explanation can be either that a simple ITMR model as the one presented in section 1.6 does not apply, or that the magnetic interaction of surface boundaries is weakened with respect to that of the bulk [145]. This topic and the ITMR will be addressed in detail in this review for the field of double perovskites. At this stage, it is worth recalling that the robustness of the grain surface magnetism determines whether the ITMR vanishes very close or far below T_C. As shown in figure 14, in FeMo double perovskites not only is T_C above room temperature, but also the MR_h dependence on the temperature approaches that of the scaling law [11, 108] (equation (17)), which means that the surface magnetism and spin polarization are closer to the bulk ones. This fact has an extremely beneficial effect on the ITMR enhancement (see figure 8). In consequence, the expectation for a further increase of T_C would be an ITMR raise at room temperature, the ITMR remaining large up to almost T_C. In the previous section we have shown how T_C can be gently enhanced by means of electron doping. In this section we survey the impact of electron doping in the magnetotransport properties.

Single crystals of FeMo double perovskites like SFMO show metallic resistivity with absolute value $\sim$0.3–0.4 mΩ cm [47, 84, 116]. Polycrystals of the same material can show
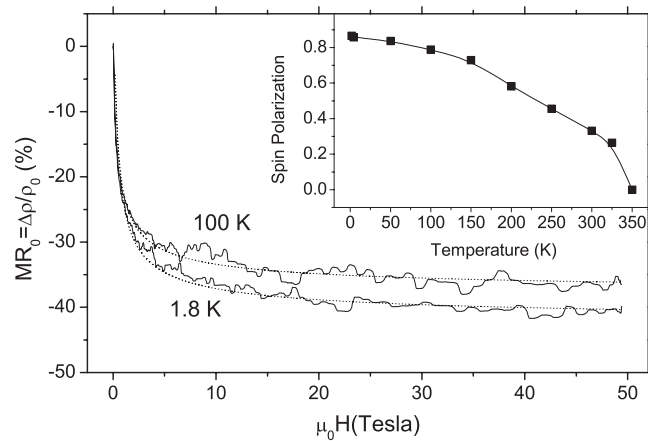
Figure 18. Magnetoresistance measurements in pulsed fields of $(Ba_{0.8}Sr_{0.2})_2FeMoO_6$. The solid lines are the experimental data and the doted lines represent the fit to the modified direct tunnelling model (see equations (21) and (22)). An absolute experimental noise of about 0.9% above 30 T is observed. The inset shows the temperature dependence of the fitted spin polarization.
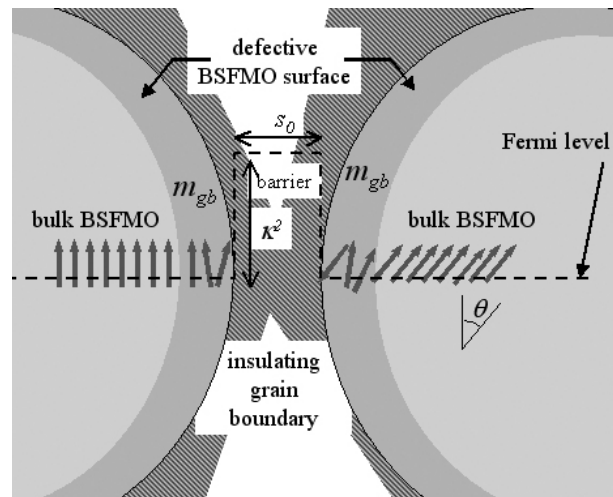

Figure 19. Schematic view of the microstructure showing the outermost BSFMO region that determines the effective magnetization for tunnelling through the insulating spacer.

semiconducting or metallic behaviour depending on the synthesis procedure, and the absolute values of the resistivity can range from those of single crystals to several orders of magnitude higher [113, 33]. The grain boundary resistance is therefore crucial in determining the resistivity in polycrystals as well as the ITMR effects. Resistivity measurements shown in figure 15(a) indicate that in the case of our undoped $(Ba_{0.8}Sr_{0.2})_2FeMoO_6$ (BSFMO) sample the absolute value of the resistivity is $\sim 2 \times 10^{-2}$ Ω cm and slightly temperature dependent. This means a relatively important grain boundary contribution, and, consequently, we expect a strong ITMR effect in our La doped $(Ba_{0.8}Sr_{0.2})_{2-x}La_xFeMoO_6$ series, which shows a resistivity two orders of magnitude higher than the one of the single crystal. This can be actually noticed in figure 15(b), with $MR_h(100\ K, 1.5\ T) = 29\%$ for BSFMO. On La doping, the absolute

value of the resistivity decreases about one order of magnitude. Grain size effects cannot be invoked in our case to explain this variation as we do not observe any line broadening in the x-ray or neutron diffraction profiles (thus, we estimate grain sizes greater than $\sim 1 \ \mu$m in all the samples). We rather suggest that the decrease of ρ and MR_h on La doping (see figure 15(b)) are attributable to the opening of new conduction channels that will not necessarily be spin dependent.

Two facts support this idea. First, the resistivity upturn on cooling shifts towards lower temperatures on La doping. Such an upturn is associated with the crossover between a resistivity dominated by the intrinsic metallic behaviour, which has a positive slope against temperature, and a tunnelling-like regime for which resistivity decreases on warming. The shift of the temperature at which the tunnelling component overcomes the metallic component can only be due to a resistance decrease of the barriers at the grain boundaries. Second, the ITMR rates are strongly reduced on La doping, meaning that the scattering of electrons passing through the new conduction channels are not affected by the magnetic field. A possible explanation for these new available channels might be the existence of some La segregation at the grain boundary that would provide electronic states of lower energy than the potential energy barrier height separating the neighbouring grains. In fact, cation segregation at the surface has already been observed in manganites [146]. These states would lead to new conduction channels and, consequently, lower resistivity as observed in figure 1(a). The conduction mechanism between the impurity states could be the second or higher order inelastic hopping due to the electron–phonon interaction. If these states took part in impurity assisted hopping, one would also expect a decrease in MR_h due to the paramagnetic nature of La, which would contribute to a spin memory loss as usually found in planar magnetic tunnel junctions [147] or even in cold-pressed CrO_2 powders [148].

In summary, although La doping has been proven to significantly enhance T_C in $(Ba_{0.8}Sr_{0.2})_{2-x}La_xFeMoO_6$, it makes worsen the ITMR response over the whole temperature range owing to the extrinsic influence on the grain boundary properties. An intrinsic spin depolarization when increasing the number of carriers cannot be discarded. In this sense, a recent analysis of the ITMR using equations (17) and (22) have revealed a critical loss of spin polarization associated with the filling of the spin down states of the conduction band [149]. Nevertheless, thanks to the perfect Fe/Mo ordering and the strong intergrain character of the conduction processes, the ITMR contribution of the parent compound BSFMO at room temperature is the largest ever reported value for a sample prepared by means of solid state reaction. The modified properties of the grain boundary in BSFMO prepared by combustion synthesis enhance the ITMR up to 10% at 425 mT [136].

On the other hand, magnetotransport properties of $Ba_{1+x}Sr_{1-3x}La_{2x}FeMoO_6$ had to be explained in terms of the increase of the spin down sub-band occupation and the moderate rise of AS as a function of doping (see table 4). In figure 16(a) the temperature dependence of the dc resistivity for $x = 0.1$, 0.2 and 0.3 is shown. In all the cases, the resistivity is found to be in the range of $\sim 10^{-2} \ \Omega$ cm and varies little with temperature. This means a substantial contribution of the intergrain resistance too, and ITMR effects can be anticipated. As the absolute value of the resistivity is independent of the doping level, we do not expect any substantial change of the microstructural parameters influencing the magnetotransport properties like the grain size, grain connectivity or La impurity assisted conduction channels at the grain boundary. This is also supported by the fact that the resistivity upturn due to the intergrain tunnelling contribution does not shift as a function of doping, contrary to the case of $(Ba_{0.8}Sr_{0.2})_2FeMoO_6$ (see figure 15(a)). Concerning the origin of such a resistivity upturn, figure 16(a) displays how it disappears under $H = 1$ T, which means that it is due to the suppression of spin dependent scattering at the grain boundary, i.e., the tunnelling feature of $\rho(T)$.

Figures 16(b) and (c) evidence how electron doping systematically reduces the LFMR effect associated with ITMR. In this series there is no reason to invoke extrinsic effects as responsible for this ITMR worsening. Instead, it seems that an intrinsic spin depolarization takes place on electron doping. Two sources of spin depolarization can be found in this series. One is the presence of AS defects (see table 4), which can act as spin scatterers and decrease the effective spin coherence length of the carriers. Moreover, it has been theoretically shown that AS disorder destroys the half-metallic ferromagnetic state of the ordered compound [92, 93]. Notice that, according to the discussion in section 2.1.2, the creation of AS defects is inherent to electron doping. Another plausible source would be the influence of electron doping itself on the electronic structure and consequently on the exchange splitting of the spin up and down sub-bands [149, 150]. In particular, the driving mechanism for the spin depolarization could be the electronic correlation, which might play an important role in the DOS when the number of conducting electrons per formula unit increases.

The strong extrinsic character of the ITMR in polycrystalline double perovskites makes it very difficult to interpret the underlying reasons for this effect to worsen. Throughout this section, both extrinsic and intrinsic effects were invoked. In our case, the extrinsic ones are related to the available conduction channels in the grain boundary: direct tunnelling and impurity assisted hopping. The intrinsic ones correspond to intrinsic depolarization sources such as AS disorder and enhancement of the electronic population of the Mo t_{2g} levels. All those effects are promoted on La doping, and are detrimental to the ITMR. It is a matter of fact that on La [115, 126, 127, 151] or Nd doping [118, 125], the ITMR effect occurring at low fields lowers. The possible origins of such a worsening are numerous. Apart from the already mentioned intrinsic factors, there are many extrinsic parameters that have been demonstrated to play an essential role in the ITMR. Indeed, almost any microstructural, impurity or compositional parameter varied in a systematic way will produce an associated monotonic ITMR change. For instance, the grain size reduction can optimize the ITMR due to the accompanying growth of the number of junctions [113]. Another example is the ITMR sensitivity to the oxidation degree of the grain boundary [111, 152], which indicates that the ITMR value could be always improved by such systematic thermal treatments under controlled atmospheres without an appreciable modification of the bulk grain. In addition, Fang *et al* have shown the reinforcement of the ITMR in Sr_2FeMoO_6 samples with APB and insulating $SrMoO_4$ nanoclusters spread within the grain [80]. This conflicts with previous reports of Sr_2FeMoO_6 annealed under weak oxidizing conditions, in which the $SrMoO_4$ impurity was thought to lie at the grain boundary rather than at the grain [152, 153]. To this fine mess one has to add the fact that the magnetocrystalline anisotropy that settles the value of the saturation magnetic field can change as a function of the cationic content [77, 135]. Thus, the magnetoresistance achieved under applied magnetic fields with values close to the saturation field can also depend on the A site stoichiometry. In conclusion, one has to take thoroughly into account the microstructure, impurity content and the grain boundary nature in order to understand the entire picture of the ITMR effect in FeMo double perovskites. This calls for the use of combined local structural probes (such as TEM, SEM and surface sensitive techniques) and macroscopic characterization tools (such as powder diffraction, thermogravimetric measurements and magnetic properties measurement).

One striking common feature of all the MR measurements in double perovskites expounded in this section, and of those appearing in the references therein, is that the magnetoresistance does not saturate at the bulk saturation field. What is more, the scaling law predicted by equation (17) is never satisfied. In order to address the origin of this observation in FeMo double perovskites, we have performed high pulsed magnetic field magnetoresistance measurements in our high quality $(Ba_{0.8}Sr_{0.2})_2FeMoO_6$ (BSFMO) sample [108]. Since the

magnetization of our sample is completely saturated at 1 T, the ITMR effect in the scope of the model described by equations (15)–(17), should fully occur below such a field. Figure 17 shows the low field magnetoconductivity ($H \leqslant 0.2$ T) as a function of the temperature and the isothermal magnetoconductivity (MC) at 4.2 K, a temperature when only the ITMR contribution is expected because it is far enough from T_C. One easily realizes that the scaling law as a function of T is fulfilled, but there is a lack of saturation in the MC at 6 T, this field being larger than the bulk saturation field to a fair extent. This fact singles out the different magnetic behaviour of the surface and the bulk BSFMO.

However one cannot conclude that the direct tunnelling model does not apply. In figure 18, the isothermal MR_0 curves under applied fields up to 50 T are shown. Unlike the behaviour found in magnetite and manganites [109, 154], MR_0 above 40 T and below 50 K clearly saturates, which shows that the high field linear magnetoresistance is not ubiquitous in the ITMR of half-metallic magnetic oxides. Instead, *the saturation value is below the maximum value foreseen for MR_0 by the direct tunnelling model, 50%*. Thus, the direct tunnelling model expounded in section 1.6 could in principle account for our measurements. Certainly, in order to explain the observed magnetoresistance, the magnetization value which determines the magnetic scattering in tunnelling processes between grains is not the bulk one, but the magnetic state in the vicinity of the grain boundary. We propose that the lack of correlation between the direct tunnelling model (equations (16) and (17)) and the experimental ITMR results can be explained by a modified Inoue and Maekawa's model in which the bulk-reduced magnetization is replaced by the magnetization of the region close to the grain boundary, m_{gb}.

$$MR_0 = -\frac{P^2 m_{gb}(H)^2}{1 + P^2 m_{gb}(H)^2}. \tag{21}$$

Figure 19 shows a schematic view of this picture. In order to verify this hypothesis, a direct measurement of m_{gb} in polycrystalline BSFMO is not currently available. Instead, we have obtained a tentative field dependence for $m_{gb}(H)$ by essaying several functional forms for the approach to saturation of m_{gb} in equation (21). The grain surface is a defective double perovskite, where off-stoichiometry, vacancies and antisite disorder are very likely to occur. Such defects act as random spin pinning centres leading to the partial suppression of ferromagnetism, owing to the different atomic environment of the surface atoms and surface–lattice relaxations. The use of a Langevin function depicting a paramagnetic-like nature of the outermost part of the grain was fruitless. In its place, m_{gb} on approach to saturation has been found to follow a functional form widely used in ferromagnets with weak random anisotropy field [155, 156],

$$m_{gb}(H) = \frac{M_{gb}(H)}{M_{gb}(H=0)} = \left(1 - \frac{a}{\sqrt{H}}\right). \tag{22}$$

Here $a = R_a^3 \beta 3_r^2 / 15 \alpha^{3/2}$, where β_r and α are proportional to the random anisotropy and the exchange strength, respectively, averaged over the distance R_a for which the local easy axes become uncorrelated. This model is suitable when $\beta_r \ll \alpha$ and the applied magnetic field is smaller than $\alpha M_{gb}(\infty)/R_a^2$, namely the exchange field. In this regime the magnetic structure is that of a quasi-collinear spin arrangement in which the tipping angle of the magnetic moments with respect to the applied field varies over the system. In figure 18 it is shown that, inserting equation (22) into equation (21), MR_0 at all temperatures can be successfully fitted [108]. The fitted region extends down to the bulk saturation field, which decreases on warming and ranges from 0.2 to 0.06 T. At lower fields, the saturation function given in equation (22) becomes singular, and no analytical expression is available. The suitability of equation (22) means that the magnetic state of the vicinity of the grain boundary can be well described as a *correlated*
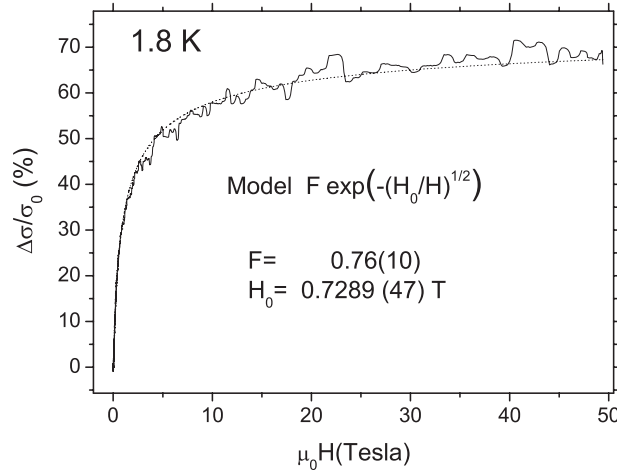
Figure 20. Fit of the experimental conductivity of $(Ba_{0.8}Sr_{0.2})_2FeMoO_6$ at 1.8 K using the empirical test function given by equation (23).

spin glass. This type of magnetic ordering was originally introduced by Chudnovsky *et al* [155] to describe a ferromagnet of wandering easy axes due to the random anisotropy, in which the correlation length (R_a) is much larger than in a canonical spin glass state. The value $P = -0.86$ is found at 1.8 K, in very good agreement with the previously reported value in Sr_2FeMoO_6 tunnel junctions [97]. Furthermore, the above explained method for P evaluation has been recently applied to the study of the carrier spin depolarization upon electron doping in Sr_2FeMoO_6 [149].

In conclusion, we have explained the magnetoresistive behaviour of BSFMO in terms of direct tunnelling between two correlated spin glass-like surfaces separated by a thin insulating layer, as depicted in figure 19. This has led us to a meaningful model from which relevant parameters regarding the grain boundary properties could be determined. Although the reliability of the above exposed model is evident, the development is worth discussing. As explained in [108], it is required that the factor κs be field independent in order to reach expression (14). In other words, we have assumed that the barrier properties are independent of the magnetic field. Using some plausible magnetic field dependence, either of the average barrier height ($\sim\kappa^2$) or of the average barrier thickness (s), our approximation could be improved. But in this case, the integration over the set of different insulating barriers to obtain the average value becomes quite complicated, because we cannot use the steepest descent approximation to perform the integration as in the case of granular magnetic films [106]. Therefore, the question whether κ^2 or s can vary with the magnetic field remains open. Any possible dependence of κs on H would yield a different functional form of $G(H)$. For instance, it has been empirically found that the magnetoconductivity of Sr_2FeMoO_6 up to 5 T follows the functional form [157]

$$MC(H) = F \exp\left(-\left(\frac{H}{H_0}\right)^{1/2}\right). \tag{23}$$

F being a constant prefactor. As shown in figure 20, our data up to 50 T in the isostructural compound BSFMO also satisfies this dependence. Of course, the existence of such a simple analytical function describing the ITMR in polycrystalline double perovskites might be useful, but it definitely deserves further theoretical support.
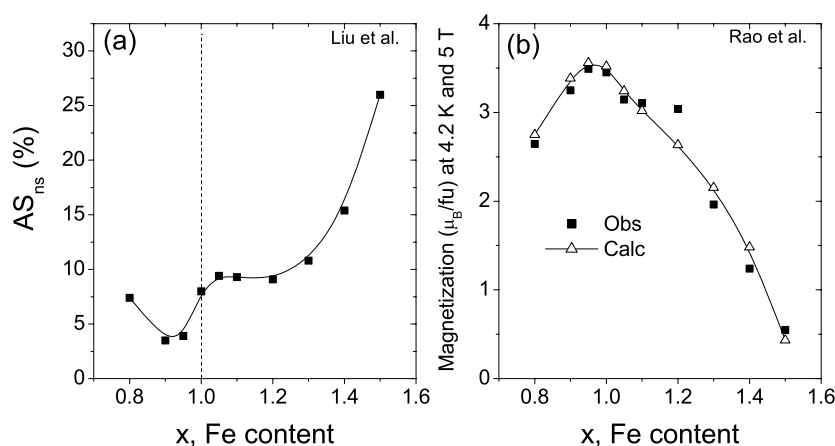
Figure 21. (a) True antisite disorder (AS_{ns}) in the non-stoichiometric $Sr_2Fe_xMo_{2-x}O_6$ (see the text) as a function of the Fe content. Data taken from [158]. (b) Observed saturation magnetization in $Sr_2Fe_xMo_{2-x}O_6$ and the calculated one (8) as given in [159].

2.2. Other stoichiometries

Up to now we have seen that the AS disorder level is somewhat related to the relative volumes of the BO_6 and $B'O_6$ octahedra. This is consistent with the intuitive picture of a cation ordering mainly controlled by differences between the ionic radii and charges. However, it is not clear yet what is the basic physical mechanism that triggers the location of Fe or Mo atoms out of their regular crystallographic sites, B and B' respectively. Doping at the B and B' sites with different cations provides an opportunity to examine the role of the cation size and charge in the BB' ordering, as well as to study the impact of the doped cations on the magnetic and structural properties of double perovskites. There are two ways to carry out doping at the B or B' sites while retaining the essential physical properties of double perovskites: either to alter systematically the 1:1 Fe to Mo content ratio or to perform weak substitution of other transition metal ions for Fe or Mo.

First we focus on the non-stoichiometric $A_2Fe_xMo_{2-x}O_6$ compounds having $x \neq 1$. In such samples, misplacement of Fe at Mo sites ($x > 1$) and vice versa ($x < 1$) is expected to occur without the formation of impurity phases [88, 158]. Due to the dilution of the Fe background which polarizes the t_{2g} hybridized sub-band, the Curie temperature decreases linearly with the Mo content for $x < 1$ [88]. Owing to the nominal off-stoichiometry, AS disorder in $Sr_2Fe_xMo_{2-x}O_6$ cannot be regarded as the fraction of misplaced Fe or Mo ions. Instead, a proper definition would be the amount of Fe(Mo) ions occupying B'(B) sites for $x \leqslant 1(x \geqslant 1)$ per formula unit. This quantity, which will be named hereafter AS_{ns}, measures the misplaced ions beyond the imposed disorder by the Fe ($x > 1$) or Mo ($x < 1$) excess. Figure 21(a) displays $AS_{ns}(x)$ extracted from the structural data published by Liu *et al* [158]. The authors also found monotonic cell shrinkage when the Fe content increase. Since this is not expected due to the larger ionic radius of Fe than that of Mo (0.645 Å for Fe^{3+} and 0.61 Å for Mo^{5+} in coordination VI [12]), this effect is attributed to the large valence disproportion of Fe and Mo in the non-stoichiometric compounds with respect to the $3+/5+ \leftrightarrow 2+/6+$ mixed valence state in Sr_2FeMoO_6. In fact, on increasing Fe content, the pristine $Mo^{5+/6+}$ ions are replaced by Fe having the same environment as in $SrFeO_3$, in which the Fe valence state must be comprised between $2+$ (the minimum in the double perovskite) and $4+$ (the valence in the

strontium ferrite). This entails a strong hole doping of the double perovskite, from which the cell shrinkage can be naturally explained due to electronic effects [118, 120, 125, 126]. Rao *et al* [159] correlated the refined AS_{ns} with the observed saturation magnetization through the spin only contributed ionic model. For their calculation they assume the following tentative charge distribution: every Fe or Mo ion which is either misplaced or in excess takes the 4+ valence state, as corresponds to $SrFeO_3$ and $SrMoO_3$. The remaining Fe and Mo atoms behave as in a canonical double perovskite. Using this model, the authors of [159] find a rather good agreement between the theoretical and the observed saturation magnetization, as shown in figure 21(b). However, other charge distributions can also account for M_S in these compounds. For instance, a satisfactory agreement has been found around the stoichiometric composition ($x = 1$) if one assumes $3d^5(Fe^{3+})$ localized spin dispersed among Mo^{6+} cores, and an itinerant nature of the Mo electrons which become linearly depolarized as x varies between 1 and 0 [88]. In any case, both models call for an antiferromagnetic coupling of misplaced Fe ions to its regular Fe neighbours, as expected from the superexchange interaction in 180° Fe–O–Fe bonds.

Rao *et al* [159] put forward an interesting argument to explain the appearance of AS disorder. On the one hand, in order to explain the good cation ordering for dissimilar enough B and B′ ions, the Gibbs free energy ($G = U + PV - TS$) must be minimized during the formation of the double perovskite phase by expelling very unlike ions to the B and B′ sites through the lowering of the internal energy (U). On the other hand, an increase of the configurational entropy by promotion of AS disorder can also stabilize the double perovskite phase. Thus, it follows that if U grows when the ionic radii and charge of the B and B′ atoms approach to each other, the AS disorder could compensate the internal energy gain by means of an entropy raise (S). According to figure 21(a), when x deviates from 1, the differences between the average radii and charge at the B and B′ sites are reduced, and therefore more and more AS disorder is required in order stabilize the double perovskite phase. Then, for the case of B = Fe and B′ = Mo the AS disorder is minimum around the stoichiometric case ($x = 1$), because at this point the differences between the B and B′ ions are the largest. The same reasoning can explain the fact that the degree of Fe/Mo ordering can be improved by increasing the synthesis temperature from 900 to 1200 °C [49], since a higher temperature reinforces the impact of the configurational entropy on the Gibbs free energy. This simple physical argument can account for most of the studies about AS disorder. For instance, we have already shown (see figure 12) that when the volume mismatch between the FeO_6 and MoO_6 octahedra is reduced, the AS disorder increases. This is because AS has to be further enhanced in order to stabilize a double perovskite phase with more alike B and B′ ions. In conclusion, the unlikeness of the average B and B′ ions will settle the final degree of AS disorder. The relevance of the unlikeness between the B and B′ sites for the minimization of AS will be stressed throughout this section with further experimental examples.

At this point we want to single out another interesting property of non-stoichiometric $A_2Fe_xMo_{2-x}O_6$ compounds. This is the development of antiferromagnetic clusters rich in Fe–O–Fe bonds embedded in a double perovskite matrix, which has to be concomitant to the Fe excess ($x > 1$) if the single phase double perovskite structure is preserved. In experimental [53] and theoretical [69, 160] studies it has been suggested that such antiferromagnetic Fe–O–Fe paths are beneficial for the stabilization of ferromagnetism in double perovskites at high temperatures. This phenomenon can become hidden in stoichiometric FeMo compounds because the misplaced Mo ions give rise to a magnetic dilution effect. However, as pointed out by Rubi *et al* [87], such a dilution effect is avoided in non-stoichiometric $A_2Fe_{1+x}Mo_{1-x}O_6$. In addition, the authors in [87] include some trivalent doping at the A site in order to counterbalance the aforementioned hole doping inherent to the Fe excess. This is achieved by
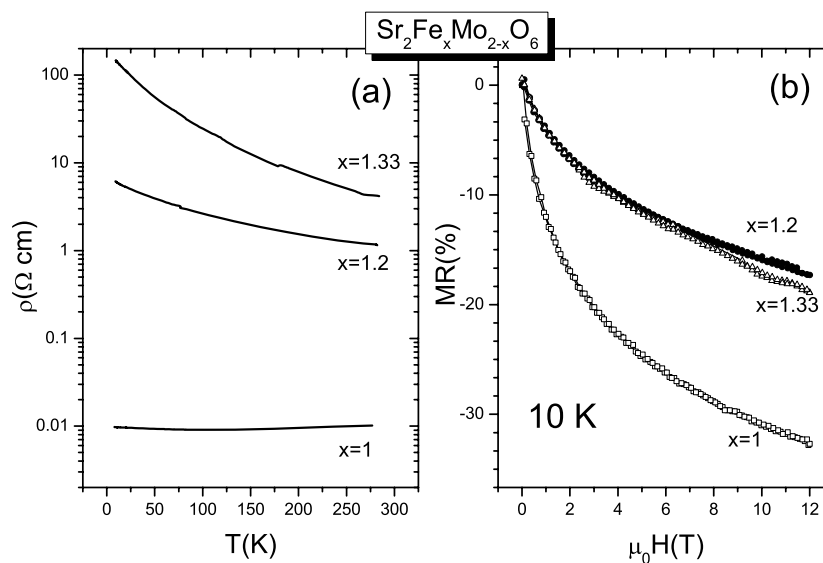
Figure 22. Temperature dependence of the dc resistivity (a) and isothermal magnetoresistance measured at 10 K (b) in $Sr_2Fe_xMo_{2-x}O_6$.

Ca^{2+} replacement by Nd^{3+}, namely $A_2 = Ca_{2-y}Nd_y$ with $y = 2x$ and $4x$, which compensates the two end valence states of the FeMo pair ($Fe^{2+}Mo^{6+}$ and $Fe^{3+}Mo^{5+}$ respectively). As a consequence, the cell volume increases with the Fe doping, as expected in view of the larger ionic radius of the Fe atom and in contrast to the result in the work by Liu *et al* [158]. Similarly to the observation by Liu *et al* AS_{ns} strongly increases with x in $Ca_{2-y}Nd_yFe_{1+x}Mo_{1-x}O_6$. Mössbauer measurements show that the molecular field acting on the Fe atom is enlarged when the Fe excess increases [161]. The main result regarding this series is the strong T_C enhancement when the Fe excess increases (about 480 K/x), which provides further support to the hypothesis raised in the works by Sánchez *et al* [53] and Alonso *et al* [69] in heavily disordered Sr_2FeMoO_6: the coherence of the AFM arrangement of neighbouring Fe–O–Fe regions is maintained across the crystal by ferromagnetic Fe–Mo–Fe coupling, and this favours the long range magnetic order in the double perovskite matrix.

We have studied the impact of the off-stoichiometry on the transport properties in series $Sr_2Fe_xMo_{2-x}O_6$. As reflected in figure 22, the resistivity and the magnetoresistance are very sensitive to the Fe excess. First, as the Fe–O–Mo bonds allowing for the electron mobility in the spin down sub-band are removed, the conduction band becomes narrower and a marked insulating character is developed on Fe doping [87, 162]. In fact, an abrupt low temperature resistivity increase of three orders of magnitude has been reported in $A_2Fe_xMo_{2-x}O_6$ around $x = 1.2$ [87, 162] (see figure 22(a)). Second, the increase of the AS disorder leads to a fast spin depolarization [92, 93]. In consequence, the ITMR effect which is responsible for the steep resistance drop at low field vanishes, as depicted in figure 22(b) and [87].

Further examples of the AS sensitivity to the B and B′ cations dissimilarity can be found in the series $Sr_2(Fe_{1-x}V_x)MoO_6$ [163], $Sr_2(Fe_{1-x}Mn_x)MoO_6$ [164] and $Sr_2(Fe_{1-x}Cr_x)MoO_6$ [24, 165]. In all cases the AS variation on doping can be correlated with the difference between the average ionic charge and radii of the B and B′ sites. In the case of V doping, V tends to occupy both Fe and Mo crystallographic sites, from which AS increases. In the case of Mn doping, the Fe/Mo ordering is improved for high doping levels
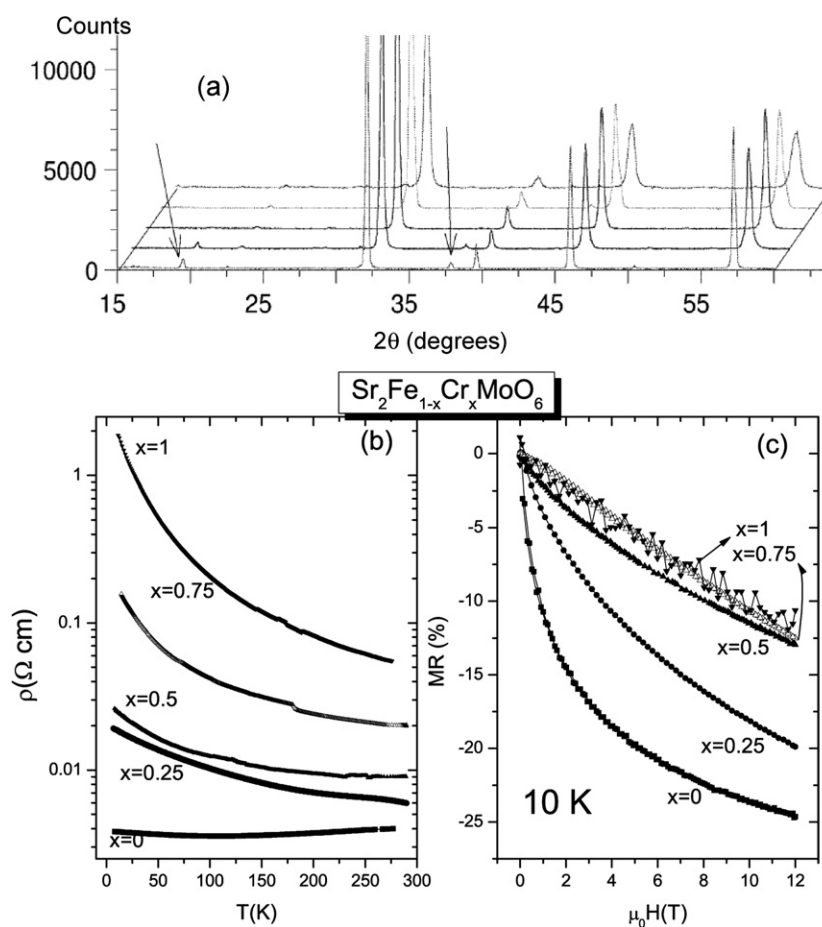
Figure 23. (a) Details of the x-ray patterns at room temperature for $Sr_2Fe_{1-x}Cr_xMoO_{6-y}$ samples. From bottom to top, $x = 0, 0.25, 0.5, 0.75$ and 1. Arrows indicate the superstructure peaks related to the ordering between B and B' sites. (b) Resistivity versus temperature for all the compounds. (c) Magnetoresistance at 10 K for $Sr_2Fe_{1-x}Cr_xMoO_{6-y}$.

($x > 0.2$), because Mn adopts preferentially the Mn^{2+} valence at the Fe site [164, 30], and then the average ionic radii and charge becomes much more different from the Mo ones with respect to the undoped compound (the high spin ionic radius in coordination VI are 0.83 Å for Mn^{2+} and 0.645 Å for Fe^{3+} [12]). We have performed a thorough neutron diffraction study on $Sr_2(Fe_{1-x}Cr_x)MoO_6$ [24]. We have found that Cr occupies preferentially the Mo site because their ionic radii are very similar (0.615 Å for Cr^{3+} and 0.61 Å for Mo^{5+} [12]). However, some Cr is left in the Fe site due to their similar valence (between 2+ and 3+), and this makes the BO_6 and $B'O_6$ octahedra shape approach to each other on Cr doping, as noticed in our neutron diffraction measurements [24]. Therefore, as displayed in figure 23(a), the AS disorder increases as the Cr content does, which is reflected in the gradually reduced intensity of the (111) and (311) superstructure peaks (marked with arrows). Figure 23(b) shows how the metallic behaviour of the resistivity in Sr_2FeMoO_6 is rapidly suppressed on Cr doping. Furthermore, in figure 23(c) it is shown that in Cr-rich compounds ($x \geqslant 0.5$) the ITMR feature is completely absent, with only a linear magnetoresistance remaining over the whole

Table 5. Cation distribution and stoichiometry of the seven measured $Sr_2Fe_{0.75}T_{0.25}MoO_6$ 25% 3d doped double perovskites. Errors are about 0.02 for Sr, 0.04 for O and 0.01–0.03 for d ions.

3d ion	A site	B site	B′ site	O content
Sc	Sr_2	$Fe_{0.62}Sc_{0.25}Mo_{0.11}$	$Mo_{0.87}Fe_{0.11}$	$O_{5.96}$
Ti	Sr_2	$Fe_{0.45}Ti_{0.19}Mo_{0.34}$	$Mo_{0.64}Fe_{0.29}Ti_{0.06}$	$O_{6.00}$
V	Sr_2	$Fe_{0.56}V_{0.14}Mo_{0.30}$	$Mo_{0.70}Fe_{0.19}V_{0.11}$	$O_{6.01}$
Cr	$Sr_{2.02}$	$Fe_{0.69}Cr_{0.09}Mo_{0.22}$	$Mo_{0.78}Fe_{0.06}Cr_{0.16}$	$O_{5.9}$
Mn	Sr_2	$Fe_{0.60}Mn_{0.25}Mo_{0.15}$	$Mo_{0.85}Fe_{0.15}$	$O_{6.0}$
Fe	$Sr_{1.99}$	$Fe_{0.94}Mo_{0.05}$	$Mo_{0.94}Fe_{0.05}$	$O_{6.0}$
Co	$Sr_{1.91}$	$Fe_{0.75}Co_{0.18}Mo_{0.07}$	$Mo_{0.93}Co_{0.07}$	$O_{5.68}$

field range. Both the conductivity and the ITMR vanishing are due to the fact that Cr-rich compounds exhibit a nearly complete random distribution of Fe, Cr and Mo over the B and B′ sites.

In order to shed some light on the factor that triggers the AS disorder, we have performed high resolution neutron diffraction studies on a series of compounds with 25% of Fe replaced by a 3d metal of the series Sc–Co [67]. Apart from testing the influence of the 3d ion size on the AS disorder, we aimed as well at a better understanding of the simultaneous occurrence of the ferromagnetic transition and the structural distortion from cubic to tetragonal in Sr_2FeMoO_6 [18], which might reflect the existence of a magnetostructural coupling. Further objectives of this work are to study the influence of the size and valence of the dopants on T_C, as proposed by Sriti *et al* [166], where a decrease of T_C simply proportional to the size of the dopant is reported. First of all, we will focus on the real sample stoichiometries by fitting the neutron patterns recorded in the paramagnetic phase, i.e., in the temperature region where all the compounds adopt the $Fm3m$ cubic structure. As in this space group there is only one free positional parameter (the x coordinate of the oxygen), the method offers the best possible decorrelation between structure and occupancy. The ratio of 3d/4d cations in the two sites was fixed to the value determined from x-ray diffraction. Table 5 lists the so determined stoichiometries and cation distributions. The percentage of dopant going to the Fe site as a function of the 3d metal is displayed in figure 24(a). On the basis of the ionic radii tabulated in [12], one realizes that a dopant with similar ionic radius to Fe (0.78 Å and 0.645 Å for Fe^{2+} and Fe^{3+} respectively in coordination VI) would occupy preferentially the Fe site. Therefore, when the ionic radius is diminished the dopant can also lie at the Mo site (0.59 Å and 0.61 Å for Mo^{6+} and Mo^{5+} respectively). However, dopants that can exhibit two different valences (and consequently different ionic radii) or mixed valence, could be present in both sites with different ionic radii. A relationship between the ionic size of the dopant and its site preference is clearly visible assuming a 3+ state for Sc–Cr, a 2+ state for Mn and a mixed 2+/3+ for Fe–Co. Interestingly, in this scheme, a very good cation ordering of the pure compound indicates a mixed valence Fe^{2+}/Fe^{3+} state, since a purely Fe^{3+} would entail an ionic radius comparable to that of V^{3+}. In figure 24(a) the dependence of the volume on the 3d element for T = Sc–Co is also shown. The hypothesis of a site selection of the dopant as a function of its volume state is confirmed by this result. The monotonic decrease between the Sc and Cr compounds reflects the decreasing ionic size when the dopant takes on the 3+ valence state. Similarly, a second decrease is nicely seen for the Mn–Fe–Co series, in which the overall larger volumes reflect again 2+/3+ valence state of these dopants. With regard to the whole AS disorder, which in this series is given by the fraction of 4d Mo ion misplaced at the Fe/3d dopant site, one can see that AS has a nearly linear dependence on the volume mismatch of the two octahedral sites, $\nu = V(BO_6)/V(B'O_6)$. Figure 24(b) shows the AS versus ν as determined by Rietveld
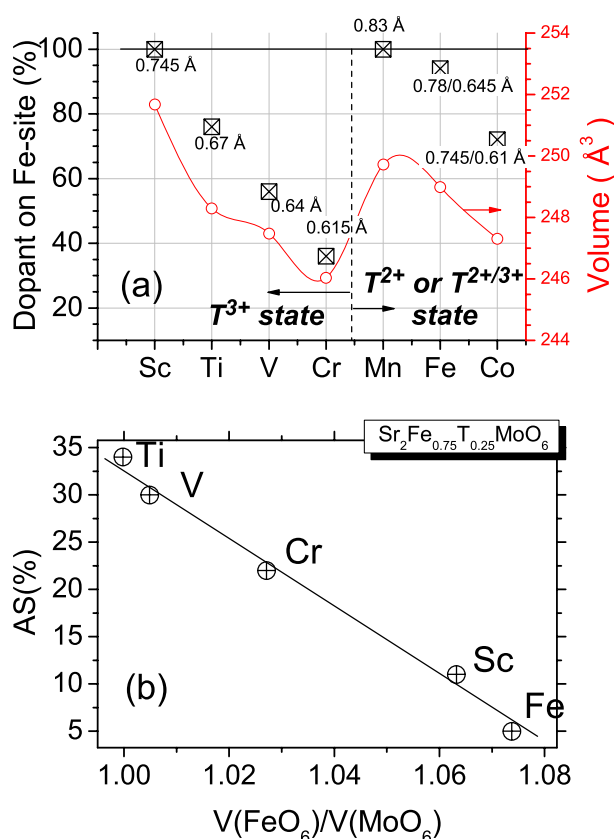
Figure 24. (a) Percentage of the dopant which goes into the Fe site (crossed squares, left axis) and the unit cell volume at 500 K (open circles, right axis) as a function of the dopant in $Sr_2Fe_{0.75}T_{0.25}MoO_6$. The proposed ionic size of the dopant, T, is indicated. (b) Percentage of [Fe–T]/Mo antisite disorder as a function of the ratio between the [Fe–T]O_6 and MoO_6 octahedra volumes.

refinements at 500 K. One readily sees that the larger AS occurs for T = Ti, for which $\nu \approx 1$ and both octahedra possess almost identical sizes. The relationship holds linear up to $\nu = 1.08$ for T = Sc, Ti, V, Cr and Fe. Mn and Co have $\nu \approx 1.11$ and deviate from the linear behaviour, probably due to the different preparation conditions. In general, assuming identical synthesis routes, we put forward that the cation ordering significantly increases for dissimilar enough octahedra volumes. This is due to the enlarged dissimilarity between the B and B′ average values of valence and ionic radii.

We move now to the interplay between the structural and magnetic properties of the $Sr_2Fe_{0.75}T_{0.25}MoO_6$ series. The results are summarized in table 6. Generally speaking, the high resolution neutron diffraction reveals an exceptionally strong influence of the dopant on the structural and magnetic behaviour. Let T_C be the temperature above which no measurable magnetic moment appears in the neutron diffraction patterns. We define T_S as the temperature at which the system undergoes a transition from $I4/m$ to $Fm3m$ space group. Careful analysis of the data revealed a third transition temperature (termed T_t), above which the system is metrically cubic while retaining the $a^0a^0c^-$ cooperative tilt of the FeO_6 and MoO_6 octahedra. Thus, below T_t the tetragonal distortion, t (see equation (2)), is different from zero, whereas below T_S the tilting angle Fe–O–Mo in the basal plane is smaller than 180°. The three transition
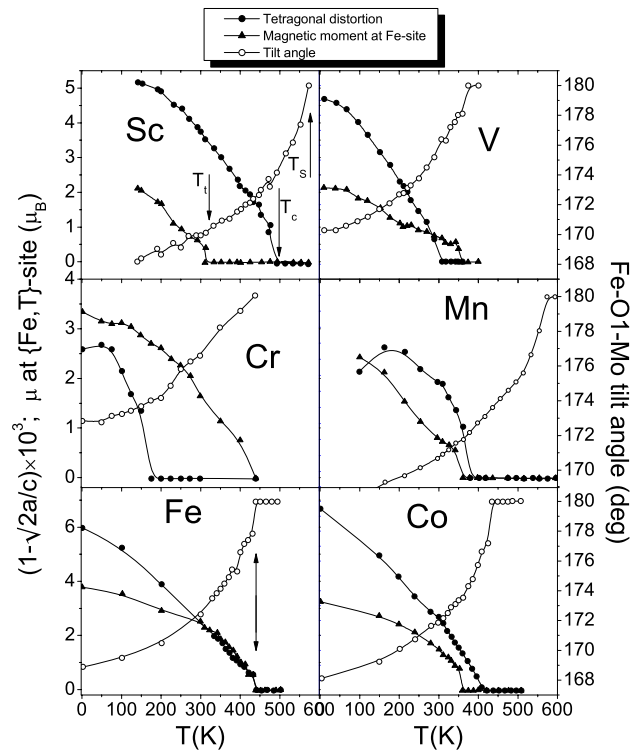
Figure 25. Temperature dependence of the tetragonal distortion (solid circles), the refined magnetic moment at the Fe–T site (solid triangles) and the value of the basal Fe–O1–Mo angle (open circles) for six different 3d 25% doped $Sr_2Fe_{0.75}T_{0.25}MoO_6$ compounds. The transition temperatures are only marked in the case of the Sc doped sample for the sake of clarity.

Table 6. Refined structural and magnetic parameters at 2 K of $Sr_2Fe_{0.75}T_{0.25}MoO_6$: lattice parameters and average Mo–O and Fe–O distances in Å; Fe–O–Mo tilt angle in the basal plane (α), refined magnetic moment at the Fe and Mo site in μ_B; saturation magnetization from SQUID measurements in μ_B/f.u.; and values of the different transition temperatures (see the text) in K.

T	Sc	Ti	V	Cr	Mn	Fe	Co
SG	$P2_1/n$	$I4/m$	$I4/m$	$I4/m$	$P2_1/n$	$I4/m$	$I4/m$
a	5.6108(2)	5.5606(2)	5.5541(4)	5.5552(8)	5.5911(6)	5.5679(7)	5.5538(6)
b	5.5915(6)				5.5780(6)		
c	7.9032(9)	7.9010(2)	7.8743(4)	8.8767(12)	7.8749(9)	7.9218(11)	7.9076(8)
Mo–O	1.963(1)	1.959(6)	1.927(6)	1.944(7)	1.969(7)	1.948(6)	1.937(5)
Fe–O	2.013(1)	1.989(6)	2.009(7)	1.994(7)	1.992(8)	2.010(6)	2.014(5
α (°)	171.1(6)	170.3(4)	172.5(4)	172.2(4)	172.8(2)	168.9(3)	168.2(5)
μ_{Fe}	2.4(1)	2.1(1)	2.0(1)	3.4(1)	3.1(1)	4.1(1)	3.3(1)
μ_{Mo}	−0.2(1)	−0.3(1)	−0.7(2)	−0.1(1)	−0.6(1)	−0.3(1)	−0.3(1)
M_S	2.5	1.3	1.3	2.2	3.4	3.8	
T_C	310	360	250	440	360	440	360
T_t	490	310	200	170	380	440	420
T_S	570	370	350	440	570	440	440

temperatures, T_C, T_S and T_t are marked with arrows in figure 25. From this plot, it becomes immediately clear that the concurrence of $T_C = T_S = T_t$ in T = Fe is the exception. Besides

the large differences among T_C, T_S and T_t, T_S is always greater than or equal to T_C and T_t. The extremely different behaviour induced by doping can be seen, for instance, comparing the transition temperature values for T = Cr and T = Mn. While in the former $T_t = 170$ K and $T_C = 440$ K, the latter has a strongly reduced T_C with $T_t \approx T_C \approx 370$ K and a very high $T_S = 570$ K. As shown in figure 25, it is clearly not possible to relate the onset of the magnetic long range order (T_C) to one of the two structural transition temperatures. Moreover, compounds for which $T_C < T_t$ show no change in the temperature dependence of the tetragonal distortion at T_C. These two findings apparently exclude any direct magnetostructural coupling mechanism. We would also like to remark that T_C can be largely influenced by factors like AS disorder [69, 85, 89], electronic band filling [115, 126, 127, 131] and steric effects [18, 83]. As all these factors do not follow a simple dependence on the 3d dopant, it is not realistic to explain the dependence of T_C on doping just with simple arguments.

3. Re-based double perovskites

Re-based double perovskites, in which the B′ site is occupied by Re ions, are the most promising ferromagnetic oxides in terms of high T_C. The compound Sr_2CrReO_6 is found to have $T_C = 635$ K [36], whereas the Ca_2FeReO_6 compound has $T_C = 530$ K [34, 167]. At the same time, Re-based double perovskites retain the attractive high spin polarization of the Mo-based ones. Kobayashi *et al* calculated for the first time the half-metallic DOS of Sr_2FeReO_6, and demonstrated a large tunnelling magnetoresistance effect in polycrystalline Sr_2FeReO_6 [43]. Throughout this section we will provide experimental evidences of high spin polarization in all the FeRe and CrRe double perovskites. When comparing the electronic structure of Sr_2FeMoO_6 and Sr_2FeReO_6 we also notice that they are qualitatively equivalent (see figure 4). Furthermore, several reports on the Fe and Re valence state indicate the coexistence of Fe^{2+}/Re^{6+} and Fe^{3+}/Re^{5+} pairs [167, 21, 168, 59]. This mixed valence state, the high Curie temperature and the metallic behaviour of compounds such as $(Ba, Sr)_2FeReO_6$ [34] or Sr_2CrReO_6 [169] suggest that the same double exchange-like mechanism of FeMo double perovskites also operates in the case of FeRe and CrRe compounds [65]. However, beyond the basic underlying physics and the almost identical crystallographic structures, there are significant differences between Re- and Mo-based double perovskites. Especially intriguing are the differences in the magnetic behaviour. Re-based double perovskites are magnetically hard [22, 167], and can show coercive fields above 2 T, in sharp contrast to the Mo-based ones, with coercive fields of a few Oe [11, 77]. Moreover, the $Mo^{5+}(4d^1, t^1_{2g}\downarrow)$ and $Re^{5+}(5d^2, t^2_{2g}\downarrow)$ ions have slightly different electronic configurations and ionic radii, so the near-E_F DOS determining the transport properties must exhibit quantitative differences [170]. In fact, the $Ca_xSr_{2-x}FeReO_6$ compounds develop a metal to insulator transition (MIT) for $x > 0.4$ [34]. On the contrary, $Ca_xSr_{2-x}FeMoO_6$ compounds remain metallic over the whole temperature and x ranges [11, 47, 171]. All these properties make the study of Re-based double perovskites very appealing, and it seems clear that systematic studies are necessary to understand their differences with respect to their Mo-based analogues. In this section we will highlight the key role played by the spin–orbit coupling in the Re atom and its electronic structure, which is crucial in order to understand the new physics behind the unexpected properties of Re-based double perovskites.

3.1. A_2FeReO_6

In this section we focus on the series A_2FeReO_6 ($A_2 = Ca_xSr_{2-x}$ or $Sr_{2-y}Ba_y$ for $x, y = 0$, 0.5, 1, 1.5 and 2). The wide range of r_A variation will simultaneously impact on lattice effects,

magnetic and magnetotransport properties: from $y = 2$ (Ba$_2$FeReO$_6$) to $x = 2$ (Ca$_2$FeReO$_6$) the ground state changes from a cubic system showing metallic behaviour to a monoclinic system showing insulating behaviour, anomalously high Curie temperature and huge coercivity. Indeed, this is the most surprising fact involving this series. The insulating nature of Ca$_2$FeReO$_6$ below 150 K was demonstrated by Iwasawa *et al* [170] through the temperature dependence of the photoemission spectral weight around the Fermi level. A narrow insulating gap opens below 150 K in the Re t$_{2g}\downarrow$ band ($\sim$50 meV), and the photoemission intensity at E_F undergoes an abrupt decrease below this temperature. This fact could be understood by the large bending of Fe–O–Re angle, which is about 156° at room temperature [21]. It is well known that such distortion reduces the pdd–π hopping interaction (see section 1.4) responsible for the conduction mechanism, which could eventually lead to the insulating behaviour. However, if this were the mechanism to produce the MIT, the pdd–π interaction decrease would straightforwardly result in a strong T_C diminishment with respect to compounds having less distorted structures, such as Sr$_2$FeReO$_6$ ($T_C \sim$ 400 K [167, 22, 27, 172]). This conflicts absolutely with the larger $T_C \sim$ 530 K of the Ca$_2$ compound. Besides, the Ca$_2$FeMoO$_6$ monoclinic compound, which exhibits the same Fe–O–Mo bending as Ca$_2$FeReO$_6$, not only is metallic over the whole temperature range, but also displays a much lower T_C value of 365 K. Definitively, the surprising phenomenology of FeRe double perovskites merits further experimental studies. Our work on A$_2$FeReO$_6$ [22] aims at a better understanding of the phase diagram of this series by means of systematic variation of r_A from A$_2$ = Ba$_2$ to A$_2$ = Ca$_2$. Our results anticipate the existence of an additional ferromagnetic interaction in Ca-rich compounds, as well as a novel magnetostructural coupling, which will be explained in sections 3.1.2 and 3.1.3. In the last subsection, we report on magnetoresistance measurements under continuous magnetic fields (up to 12 T) which demonstrate the existence of a finite spin polarization in all the FeRe compounds, as well as additional magnetoresistance contributions resembling the CMR behaviour of some manganese oxides.

3.1.1. Phase diagram: enhanced ferromagnetism for the monoclinic compounds. Refinements of the x-ray diffraction patterns at room temperature indicate that the samples are single phase except for the presence of tiny amounts of impurity phase. A common impurity, hardly detected by x-ray diffraction, is the metallic Re^0 in amounts equal to or less than 0.6%. Only in the case of $y = 2$ was an asymmetric broadening of the base of the main diffraction peaks observed, which may be related to the presence of a minor secondary perovskite phase poorly crystallized. Concerning the crystallographic and magnetic structure of Ca$_2$FeReO$_6$, Westerburg *et al* [39] claim phase separation in two different monoclinic phases with slightly different lattice parameters across a wide temperature range, already present at room temperature. Granado *et al* [173] reported the same phase separation below 150 K. On the contrary, Oikawa *et al* [38] found a structural phase transition at about 140 K between the aforementioned monoclinic phases, but with single phase behaviour below and above this temperature. These differences could be related to synthesis details, and the phase separation between the two monoclinic phases with very close free energies might be a sample dependent phenomena. In our Ca$_2$FeReO$_6$ sample, we have not found any evidence of phase separation at room temperature. The corresponding XRD pattern was successfully refined with one monoclinic $P2_1/n$ crystallographic phase, yielding structural parameters similar to the ones reported by Oikawa *et al* [38]. The compounds with $y \geqslant 0.5$ show cubic structure (space group $Fm3m$) whereas Sr$_2$FeReO$_6$ is tetragonal (space group $I4/m$), and compounds with $x \geqslant 0.5$ are monoclinic (space group $P2_1/n$). The symmetry loss when going from $y = 2$ to $x = 2$ can be understood by taking into account that a smaller cation size favours the tilting of the Fe/ReO$_6$ octahedra, as already explained in the introduction. The tilts related to the tetragonal
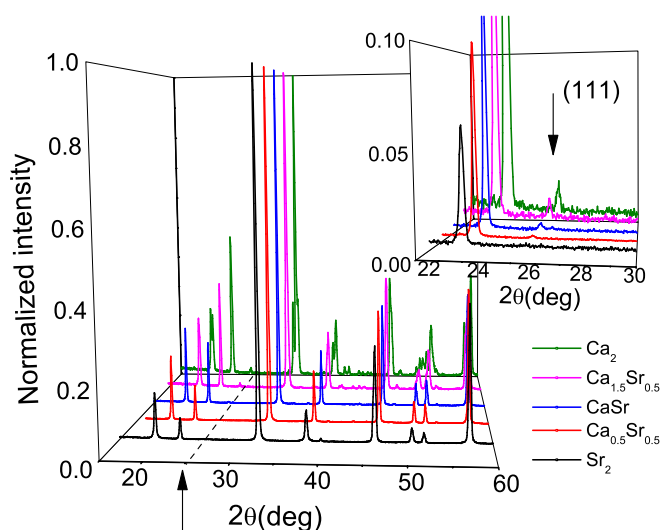
Figure 26. X-ray diffraction patterns at room temperature of the $Ca_xSr_{2-x}FeReO_6$ compounds. From bottom to top, $x = 0, 0.5, 1, 1.5, 2$. The inset shows in detail de 2θ range where the (111) peak appears and marks the appearance of the $P2_1/n$ structure.

and the monoclinic distortions entail small displacements of the oxygen atoms from the ideal cubic positions, giving rise to new diffraction peaks. Figure 26 shows the room temperature x-ray diffraction patterns for $x = 0, 0.5, 1, 1.5$ and 2. The monoclinic distortion of the unit cell is clearly visible for the $x = 2$ and 1.5 samples, and the patterns can be perfectly fitted within the $P2_1/n$ space group. The patterns of the $x = 1$ and 0.5 samples resemble the pseudocubic structure. However, a detailed inspection of the pattern evidences the presence of the (111) diffraction peak (see the inset of figure 26), which is forbidden in the tetragonal I-type lattice. It can be indexed in a primitive cell, and therefore, according to the rest of the series, we have refined the patterns in the $P2_1/n$ for the $x = 1$ and 0.5 compounds. It is worth pointing out that such fittings give better reliability factors than those performed within the $I4/m$ space group, as done in [167]. The lattice parameters obtained from the Rietveld refinements are shown in figure 27. In order to compare the overall behaviour across the studied series, the lattice parameters in the pseudocubic cell (see equation (1)) for the tetragonal and monoclinic compounds are represented instead of the parameters of the true unit cell. This is reasonable given the small distortions with respect to the cubic cell. Although the octahedra can undergo relatively large tiltings, the β angle deviates less than 0.05° from 90° (see figure 1). Beginning from $y = 2$ to $x = 0.5$ a linear dependence is observed. However, large deviations from this linear behaviour are noticed for $1 \leqslant x \leqslant 2$, for which the compression of the lattice parameters are as large as ~1% for $x = 2$. The origin of this effect is mainly steric, because exactly the same behaviour is displayed by lattice parameters of A_2FeMoO_6, as shown in figure 27. However, the huge structural effect can trigger new phenomena such as a modified electronic structure [34, 44] or a large magnetoelastic coupling [22, 173, 174]. For instance, when comparing the individual behaviour of the lattice parameters and the direction of the spontaneous magnetization at room temperature in Ca_2FeReO_6, Granado [174] and Oikawa [38] have reported independently that the spontaneous magnetization axis lies in the ac plane, the b axis being a magnetic hard axis. Such anisotropy could be ascribed to the lattice deformation. In figure 27 we notice that at room temperature the ac plane shrinks, whereas
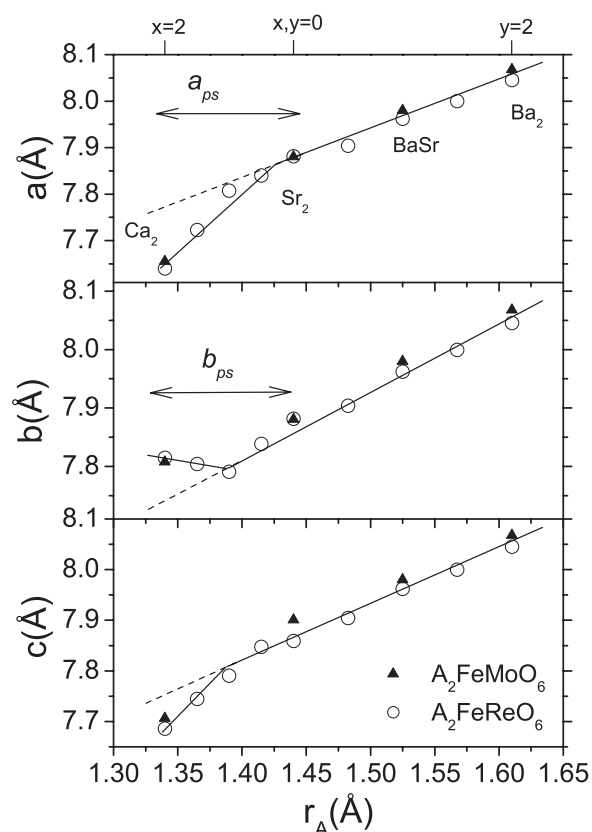
Figure 27. Room temperature cell parameters obtained from x-ray diffraction as a function of the average A site radius in A_2FeReO_6 (open circles) and A_2FeMoO_6 (solid triangles). In order to compare the overall behaviour, in the case of the tetragonal and monoclinic samples ($x \geqslant 0$) the lattice parameters a and b have been replaced by the pseudocubic parameters, $a_{ps} = a\sqrt{2}$ and $b_{ps} = b\sqrt{2}$. Lines are visual guides.

the b axis expands. This fact singles out the existence of a coupling between the structural and magnetic degrees of freedom, which brings about the hard anisotropic direction along the expanded b axis as a result of the orbital anisotropic charge density. This subject will be addressed in the next subsection. Very recently, it has also been demonstrated that at T_C, the cubic Ba_2FeReO_6 compound undergoes a slight tetragonal distortion arising from the strong magnetostructural coupling in Re-based compounds [175].

Low temperature magnetization loops are shown in figure 28. In the simplest ionic picture, two ionic configurations are possible [21, 167, 168]: Fe^{3+}–Re^{5+} and Fe^{2+}–Re^{6+}. NMR and XMCD measurements in our samples confirm that the total Re magnetic moment is antiparallel to the Fe magnetic moment [19, 176]. Therefore, both ionic configurations give an expected saturation magnetization of 3 μ_B/f.u. for spin only moments. In addition, theoretical calculations by Wu [44] predict strong band hybridization, but the calculated total spin is again 3 μ_B/f.u. As a consequence, the expected maximum value for the magnetization in these compounds is 3 μ_B/f.u. if the spin–orbit coupling is not taken into account. In figure 28 it is shown that the compounds with large cation size and zero or negligible monoclinic distortion ($x \leqslant 0.5$ and $y \geqslant 0$) achieve saturation at 5 K under an applied field of 5 T. Deviations from 3 μ_B/f.u. are normally explained as due to the presence of AS defects. Nevertheless, for the
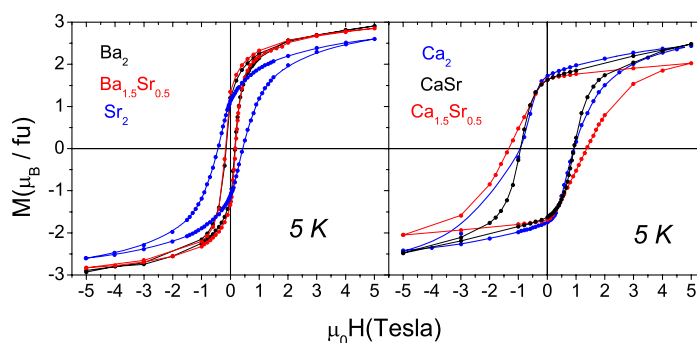
Figure 28. Low temperature magnetization loops for selected $Ba_{2-y}Sr_yFeReO_6$ ($y = 2$, 1.5 and 0) having large cation sizes (left panel) and $Ca_{2-x}Sr_xFeReO_6$ ($x = 1$, 1.5 and 2) having small cation size (right panel).
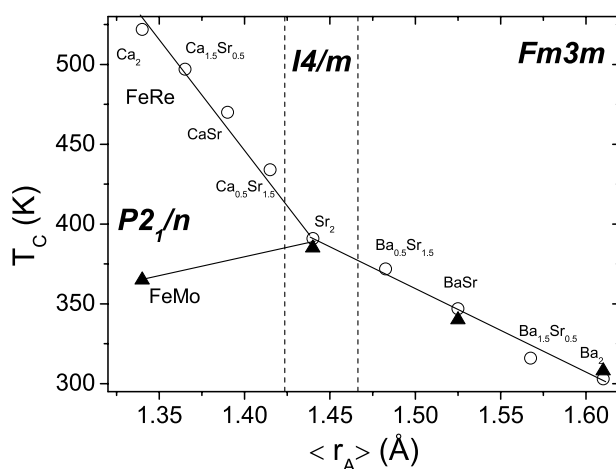

Figure 29. Phase diagram as a function of the average ionic radius at the A site in A_2FeReO_6 (open circles) and A_2FeMoO_6 (solid triangles). The coincidental behaviour in both series occurring for large cations sizes breaks for the compounds with cation size smaller than that of $A_2 = Sr_2$. Lines are visual guides.

compounds with small cation size and large monoclinic distortion ($x \leqslant 1$) the magnetization under 5 T is substantially lower than 3 μ_B/f.u., even though the refinements of the x-ray data do not yield significant amounts of AS disorder (AS < 5%). The low M_S and the lack of saturation at 5 T correlate with the large magnetic anisotropy at low temperatures of those compounds, as explained later on.

Now we will focus on the values of T_C as a function of r_A, displayed in figure 29. Two remarkable features are noticed in this plot. First, with regard to the compounds with $y \geqslant 0$ showing a cubic structure, a roughly linear increase in T_C when decreasing the ionic radius is observed, in agreement with the FeMo isostructural compounds. This increase can be therefore accounted for by the modification of the pdd–π hybridization mechanism, which, as proposed in section 2.1, is determined by the Fe–O and Re–O distances. However, taking into account the similar electronic structure of $Ba_{2-y}Sr_yFeReO_6$ and $Ba_{2-y}Sr_yFeMoO_6$, and their identical lattice parameters, one would expect a larger T_C in cubic Re-based compounds than in the Mo-based ones, because the $Re^{5+}(5d^2; t_{2g}\downarrow^2)$ ion contributes to the conduction band with two

electrons per formula unit instead of one. Second, on further decreasing r_A, the $\alpha = $ Fe–O–Re angle starts to deviate from 180° due to the octahedra tilting in the tetragonal and monoclinic space groups. It is known that the bending of such a bond angle decreases the pdd–π hopping interaction, and therefore is detrimental for the ferromagnetic interaction (see equations (10), (11) and (18)). As shown in figure 29, this effect is nicely seen in $Ca_{2-x}Sr_xFeMoO_6$ through the reduction of T_C as a function of the Ca content. However, a large deviation from this behaviour is found in the Ca-rich Re-based compounds. It seems that the ferromagnetic interaction is reinforced even though the pdd–π coupling via Fe(t_{2g})–O($2p_\pi$)–Re(t_{2g}) states is disturbed by the α deviation from 180°. In consequence, an additional mechanism must be invoked in order to explain the anomalous T_C increase for $x > 0$.

In order to understand both paradoxical observations, the lack of T_C raise in cubic compounds with Mo replaced by Re and the apparent reinforcement of the ferromagnetism when decreasing the ppd–π hybridization terms, Re-based double perovskites should comply with two essential prerequisites:

(1) The orbital degeneracy of the t_{2g} and e_g eigenstates of the cubic crystal electric field is lifted by some mechanism.
(2) An additional ferromagnetic interaction different from the pdd–π coupling must come into play.

If (1) is satisfied, the two Re 5d electrons would be distributed in the split sub-bands, which brings about the possibility of an electronic occupancy of the Re $t_{2g}\downarrow$ levels crossing the Fermi level smaller than two electrons per formula unit. Owing to the small distortions of the cubic crystal potential in $Ba_{2-y}Sr_yFe[Re, Mo]O_6$, the orbital degeneracy is not disrupted across the whole $0 \leqslant y \leqslant 2$ range. In consequence, to date published electronic structures for Ba_2FeReO_6 and Sr_2FeReO_6 do not differ significantly from that of Sr_2FeMoO_6 [43, 44, 177]. Therefore, the only available interaction that can lift the degeneracy of the t_{2g} sub-bands is the strong spin–orbit on-site coupling in the Re atom. It is well known that the spin–orbit coupling constant in 5d elements is very large compared to 4d ones [178] (for instance, for neutral Re ions it is about 0.25 eV). This is due to broader space distribution of the 5d orbitals as compared to the 4d ones. This fact was first noticed by Jeng *et al* [177] by means of relativistic LSDA band structure calculations including the spin–orbit interaction. The enhanced Re spin–orbit coupling constant, together with the strong magnetostructural coupling in Re-based double perovskites evidenced in sections 3.1.2 and 3.1.3, led us to think that the spin–orbit interaction must be treated at the same level as the crystal electric field in Re. The spin–orbit interaction provides the basis for the splitting of the Re t_{2g} levels, which can justify an effective carrier density per formula unit $n_e \approx 1$, as occurs in Mo-based double perovskites.

On the other hand, the monoclinic distortion of the ligand cubic crystal field in strongly distorted double perovskites can explain the anomalous T_C increase in the $0 \leqslant x \leqslant 2$ compounds. Recent LSDA calculations [44] have shown that a finite down spin Fe(e_g)–O($2p_\sigma$)–Re(e_g) coupling (pdd–σ) emerges at the Fermi level in Ca_2FeReO_6, which is due to the t_{2g}–e_g mixing caused by the lattice distortion. At the same time, the Fe $t_{2g}\downarrow$ component at the Fermi level decreases due to the bending of the α bond angle. Although this mechanism reduces the Fe–O–Re pdd–π coupling, the presence of the pdd–σ coupling could stabilize the ferromagnetic state for large monoclinic distortions, and hence leads to the increasing T_C as a function of x. Very recently, a linear relationship between the Re spin magnetic moment (m_S^{Re}, antiparallel to the Fe one) and T_C has been found in $A_{2-x}Sr_xFeReO_6$ (A = Ca, Ba) [176]. The m_S^{Re} value increases as $x \to 2$, contrary to the observed behaviour in the Mo analogue compounds [117], where only the pdd–π coupling plays a role. The observed variation of m_S^{Re} is in agreement with the previously expounded idea of a Curie temperature simply proportional

to the hybridization strength of 5d states at the B' site with Fe 3d states. However, since we can assume the same tendency for the pdd–π coupling in the Re-based compounds as in the isostructural Mo-based ones, the m_S^{Re} dependence on x cannot be explained by taking into account the sole $V_{pd\pi}$ hybridization terms, which weaken as $x \to 2$. Thus, we put forward that the $V_{pd\sigma}$ hybridization terms are responsible for the huge T_C enhancement in monoclinic A_2FeReO_6 compounds.

Therefore, a suitable model to explain the T_C variation in A_2FeReO_6 should incorporate the following ingredients:

- Carrier density at the Fermi level similar to that of FeMo double perovskites, which is nominally $n_e = 1$.
- The relative composition of sub-bands crossing the Fermi level with t_{2g} and e_g character.
- The gradual change of $V_{dpd\pi}$ and $V_{dpd\sigma}$ hybridization terms as a function of the $d_{Fe/Re-O}$ distances and the Fe–O–Re bond angle ($\alpha = \pi - 2\omega$).

Let ρ_{eg} and ρ_T be the e_g and total densities of states at the Fermi level. According to Wu *et al* [44], $\rho_{eg}/\rho_T = 0$ in the range $y \geqslant 0$ (including Sr_2FeReO_6), whilst $\rho_{eg}/\rho_T \sim 0.08$ for Ca_2FeReO_6, which has an average bond angle $\alpha = 152°$ [38]. The refinements of our x-ray data yield $\alpha = 150°$, $161°$, and $171°$ for Ca_2, CaSr and Sr_2 compounds respectively. However, the determination of bond angles and the transition metal distances requires a very accurate description of the oxygen positions. The lack of a systematic structural description of the series A_2FeReO_6 by means of high resolution neutron diffraction, as well as the unknown behaviour of $T(\omega)$, prevents equations (10) and (11) from being tested with experimental data. This means that the proposed model only explains the T_C increase qualitatively, at least until a precise description of $T(\omega)$ and reliable calculations of ρ_{eg}/ρ_T are available.

3.1.2. Relevance of the strong spin–orbit coupling. Throughout the previous subsection we have overlooked the detailed discussion about the relevance of the spin–orbit coupling in Re-based double perovskites. The aim of this subsection is to justify the existence of a non-zero orbital moment in Re coupled with the spin moment via the spin–orbit interaction, and to emphasize the fact that the structural and magnetic degrees of freedom are no longer independent. In fact, the spin–orbit treatment presented in this subsection can be applied to every kind of 5d element in the frame of the double exchange-like model established for high T_C double perovskites. It is well known from the theory of transition metal oxides that the wavefunctions that describe the atomic d state must diagonalize simultaneously the atomic Hamiltonian, H_{at}, and the crystal electric field potential, V_{CEF}. In an ionic environment with cubic symmetry, such as the octahedral B and B' interstices of double perovskites, the t_{2g} and e_g states are the true eigenfunctions, built up with linear combinations of the spherical harmonics, because V_{CEF} is exclusively composed of a purely cubic potential, V_{cubic}. The t_{2g} end e_g states have the same radial factor as the atomic wavefunctions, but the angular factors are linear combinations having $\langle l_z \rangle = 0$ (see equation (5)). The tetragonal and monoclinic distortions only bring about small first order corrections to the eigenvalues associated with t_{2g} and e_g states. Within this scenario, there is no possible source of orbital moment in double perovskites. However, XMCD measurements have proven the existence of a significant orbital moment borne by the Re atom in A_2FeReO_6 [176] and Sr_2CrReO_6 [179], as well as in other double perovskite compounds with 5d transition metals at the non-magnetic B' site [180]. In these studies, the Re or W orbital moment aligns antiparallel to the spin moment as corresponds for a less than half-filled shell. Although the actual Re spin (m_S) and orbital (m_L) moments values are still a matter of debate, the $|m_L/m_S|$ ratio has been found to be $\sim$0.3 [176, 179], which is not the case in Sr_2FeMoO_6 showing negligibly small orbital moment at the Mo site [54]. Then,

what is the reason for Re-based double perovskites to show an unquenched orbital moment in a cubic ligand environment? As suggested by Jeng *et al* [177], we will see that the only difference between Mo- and Re-based double perovskites is that in the former, the spin–orbit interaction can be neglected because of the lighter Mo nucleus.

The spin–orbit interaction has its origin in the relativistic theory, and in the case of a single electron in an isolated atom, it is derived from Dirac's equation as [181]:

$$H_{\mathrm{so}} = \xi(r)\vec{l}\cdot\vec{s} = \xi(r)(l_x s_x + l_y s_y + l_z s_z) \tag{24}$$

where

$$\xi(r) = -\frac{e\hbar}{2m_{\mathrm{e}}^2 c^2}\frac{1}{r}\frac{\mathrm{d}U(r)}{\mathrm{d}r} \tag{25}$$

with spherically symmetric potential $U(r)$ for the electron. Having the coordinate system fixed on the electron, equations (24) and (25) result from the Lorentz interaction of a relativistic electron with the magnetic field induced by the motion of the nucleus around the electron. The strength of the spin–orbit interaction in iron group ions is about one order of magnitude smaller than that of the Coulomb interaction, and it is comparable to that of small distortions of the cubic ligand electrostatic energy arising from tetragonal and monoclinic distortions (low symmetry ligand electric field in [178]). Nevertheless, in 5d elements as Re^{5+}, the charge cloud is much more spread out in the space and the nucleus charge is larger, so the integration over radial coordinates when calculating the matrix elements of H_{so} leads to much larger values of the spin–orbit strength. For example, whereas the typical crystal field splitting in transition metal oxides is 2–3 eV, we will show that for Re^{5+} the spin–orbit splitting can be as large as 0.4 eV. It becomes clear that the spin–orbit interaction cannot be neglected as compared to $H_{\mathrm{at}} + V_{\mathrm{cubic}}$, so that we will have to work out a common set of orthonormal eigenfunctions. In order to proceed, it is convenient to introduce the equivalence between the t_{2g} subspace with a single electron and the subspace of a p shell, the so-called the $T{-}P$ isomorphism. If we calculate the l_x, l_y and l_z by using the explicit forms of the $|t_{2g}\rangle$, $|e_g\rangle$ states in equation (5), one gets [182][3]:

$$
l_x =
\begin{array}{c c}
\begin{array}{ccccc} \mathrm{d}_{yz} & \mathrm{d}_{zx} & \mathrm{d}_{xy} & \mathrm{d}_{x^2-y^2} & \mathrm{d}_{3z^2-r^2} \end{array} & \\
\left(\begin{array}{ccc|cc}
0 & 0 & 0 & -\sqrt{3}i & -i \\
0 & 0 & i & 0 & 0 \\
0 & -i & 0 & 0 & 0 \\
\hline
\sqrt{3}i & 0 & 0 & 0 & 0 \\
i & 0 & 0 & 0 & 0
\end{array}\right) &
\begin{array}{l}
\mathrm{d}_{yz} \\
\mathrm{d}_{zx} \\
\mathrm{d}_{xy} \\
\mathrm{d}_{x^2-y^2} \\
\mathrm{d}_{3z^2-r^2}
\end{array}
\end{array}
\tag{26}
$$

$$
l_y =
\left(\begin{array}{ccc|cc}
0 & 0 & -i & 0 & 0 \\
0 & 0 & 0 & \sqrt{3}i & -i \\
i & 0 & 0 & 0 & 0 \\
\hline
0 & -\sqrt{3}i & 0 & 0 & 0 \\
0 & i & 0 & 0 & 0
\end{array}\right)
\tag{27}
$$

$$
l_z =
\left(\begin{array}{ccc|cc}
0 & i & 0 & 0 & 0 \\
-i & 0 & 0 & 0 & 0 \\
0 & 0 & 0 & 0 & 2i \\
\hline
0 & 0 & 0 & 0 & 0 \\
0 & 0 & -2i & 0 & 0
\end{array}\right).
\tag{28}
$$

[3] Throughout this section, the angular momenta are always given in units of $\hbar$. The spinor space is omitted.

At first glance we notice that all the matrix elements of l in the e_g subspace are zero. In other words, the orbital momentum is completely quenched in the e_g state, and therefore there is no first order contribution of the spin–orbit interaction within this subspace. On the contrary, in the t_{2g} subspace the orbital angular momentum is not quenched. Moreover, if we inspect closely the three 3×3 matrices corresponding to the t_{2g} boxes in equations (26)–(28), one immediately realizes that those are the matrix elements of $(-l_x, -l_y, -l_z)$ in the p state of free atoms, which is nothing but a $l = 1$ space. Thus, it yields the relationship,

$$\vec{l}(t_{2g}) = -\vec{l}(p) \tag{29}$$

which tells us that we can associate one state of the t_{2g} subspace, and only one, with another one of the six p states, the relations among the elements of each subspace being preserved with regard to l^2, l_z. This concept is formally defined as an isomorphism. Therefore, the expected value of $l^2 = l_x^2 + l_y^2 + l_z^2$ in the t_{2g} subspace is $l(l + 1)$ not with $l = 2$ but with $l = 1$. This means that the orbital angular momentum is partially quenched in the t_{2g} state. It should be noted that the T–P equivalence is only a formal matter as seen form the fact that $l(t_{2g})$ does not satisfy the commutation rules that the angular momentum with $l = 1$ should satisfy. This is due to the non-zero value of the off-diagonal matrix elements between t_{2g} and e_g states given in equations (26)–(28). However, if the cubic crystal field splitting is large enough, the off-diagonal elements can be neglected and we can work out the ground state and the splitting of the 5d states according to the following rules:

(1) The e_g subspace is characterized by $l = 0$, and therefore there is not spin–orbit splitting ascribed to these states.
(2) The t_{2g} subspace has $l = 1$, and the new eigenfunctions and eigenvalues of the total Hamiltonian, $H_{at} + V_{cubic} + H_{so}$, are those of j^2, j_z, l^2 and s^2 according to the sum rules of $j = 1 \otimes 1/2$.
(3) The spin–orbit interaction does not connect e_g and t_{2g} states and both subspaces can be treated independently.

Hence, the T–P isomorphism solves immediately the spin–orbit interaction in the e_g subspace and also gives some hints to solve it easily in the t_{2g} subspace. The treatment will be valid as long as the crystal electric field splitting, $\langle t_{2g}|V_{CEF}|t_{2g}\rangle - \langle e_g|V_{CEF}|e_g\rangle$, is large enough to neglect the $\langle t_{2g}|H_{so}|e_g\rangle$ matrix elements. Let us restrict ourselves now to the t_{2g} subspace. Within a 5d shell, $\xi(r)$ becomes a scalar operator:

$$H_{so} = \lambda \vec{l}(t_{2g}) \cdot \vec{s} = \text{equation (29)} = -\lambda \vec{l}(p) \cdot \vec{s} = -\tfrac{1}{2}\lambda(j^2 - l^2 - s^2) \tag{30}$$

where

$$\lambda = \int r^2 dr\, R_{5d}^2(\vec{r}). \tag{31}$$

Due to the T–P isomorphism there must exist a basis in which H_{so} has the same diagonal expression as in the case of a $j = 1 \otimes 1/2$ space. By equation (30), this is to say:

$$H_{so} = -\frac{1}{2}\lambda \begin{pmatrix} \overset{j=3/2}{} & & \overset{j=1/2}{} \\ 1 & 0 & 0 \\ 0 & 1 & 0 \\ \hline 0 & 0 & -2 \end{pmatrix}. \tag{32}$$

Notice that equation (32) depicts a 6×6 matrix, because we have omitted the j_z index. Then, the new electronic configuration due to the spin–orbit interaction is split in two levels, one with twofold degeneracy, $E(j = 1/2) = \lambda$, and another one with fourfold degeneracy, $E(j = 3/2) = -\lambda/2$. According to [178], $\lambda = 0.25$ eV. Provided that λ of Re in

the ReO_6 octahedra does not differ significantly from that of the isolated atom, the main conclusion is that the spin–orbit splitting of the degenerate t_{2g} states amounts to $\sim E(j = 1/2) - E(j = 3/2) = 3\lambda/2 = 0.375$ eV. On the other hand, the calculated electronic structure of Sr_2FeMoO_6 [11, 42], (Ba, Sr, Ca)$FeReO_6$ [44] and Sr_2CrReO_6 [45] show repeatedly an anomalously large exchange splitting $\Delta'_{ex} \sim 1$ eV at the non-magnetic ion site B', owing to the pdd–π hybridization. Δ'_{ex} is around 3 times larger than the spin–orbit splitting in Re. In consequence, we cannot adopt the eigenfunctions of $H_{at} + V_{cubic} + H_{so}$ as the true eigenfunctions of the total Hamiltonian. Instead, we have to apply the perturbation theory to the $|t_{2g}\downarrow\rangle$ and $|t_{2g}\uparrow\rangle$ subspaces within the scheme $H_{at} + V_{cubic} + V_{dpd\pi} \gg H_{so}$. Such subspaces have threefold degeneracy, and the unperturbed energy is given by V_{cubic} and the hybridization contribution, say $\langle t_{2g}\uparrow(\downarrow)|V_{dpd\pi}|t_{2g}\uparrow(\downarrow)\rangle = +(-)\Delta_{ex}/2$:

$$E(t_{2g} \uparrow) = -4Dq + \frac{\Delta_{ex}}{2}$$
$$E(t_{2g} \downarrow) = -4Dq - \frac{\Delta_{ex}}{2}. \tag{33}$$

The stationary perturbation theory for degenerate states demands that in order to calculate the perturbed eigenvalues (to first order) and the eigenstates (to zeroth order) of the Hamiltonian corresponding to a degenerate unperturbed state, $|t_{2g}\uparrow(\downarrow)\rangle$, one must diagonalize the matrix $H_{so|t_{2g}\uparrow(\downarrow)}$, which represents the perturbation H_{so} restricted to the eigensubspace associated with $E(t_{2g}\uparrow(\downarrow))$. Therefore, the next step is to write the H_{so} matrix in terms of the $|t_{2g}\uparrow(\downarrow)\rangle$ basis, $\{t_{2g}\} = \{|d_{yz}\downarrow\rangle, |d_{zx}\downarrow\rangle, |d_{xy}\downarrow\rangle, |d_{yz}\uparrow\rangle, |d_{zx}\uparrow\rangle, |d_{xy}\uparrow\rangle\}$. This can be calculated by means of the T–P isomorphism and the Clebsch–Gordan coefficients [150]:

$$H_{so} = \frac{1}{2}\lambda \begin{array}{c} \quad\quad |t_{2g}\uparrow\rangle \quad\quad\quad |t_{2g}\downarrow\rangle \\ \begin{pmatrix} 0 & i & 0 & 0 & 0 & -1 \\ -i & 0 & 0 & 0 & 0 & i \\ 0 & 0 & 0 & 1 & -i & 0 \\ 0 & 0 & 1 & 0 & -i & 0 \\ 0 & 0 & i & i & 0 & 0 \\ -1 & -i & 0 & 0 & 0 & 0 \end{pmatrix} \end{array}. \tag{34}$$

From equation (34) we can extract a lot of information. First of all, the 3×3 boxes that represent $H_{so|t_{2g}\uparrow(\downarrow)}$ can be easily diagonalized because they are proportional to the σ_y Pauli matrix, and therefore their eigenvalues will be 1, 0, -1. In figure 30 it is shown how the spin–orbit interaction, to a first order approximation, completely removes the degeneracy of the $|t_{2g}\uparrow(\downarrow)\rangle$ subspaces. What is more important, the ground state has no longer $\langle l_z \rangle = 0$, but it has a finite $\langle l_z \rangle$, which is found to be antiparallel to the spin moment, s_z, as corresponds for a less than half-filled d shell. The zeroth order eigenfunctions are (we use a normalized spin–orbit expected energy as quantum number to index the orbital part of the functions):

$$|1\uparrow(\downarrow)\rangle = \frac{1}{\sqrt{2}}[-i|d_{yz}\uparrow(\downarrow)\rangle + |d_{zx}\uparrow(\downarrow)\rangle]$$
$$|0\uparrow(\downarrow)\rangle = |d_{xy}\uparrow(\downarrow)\rangle \tag{35}$$
$$|-1\uparrow(\downarrow)\rangle = \frac{1}{\sqrt{2}}[i|d_{yz}\uparrow(\downarrow)\rangle + |d_{zx}\uparrow(\downarrow)\rangle].$$

We can incorporate to the model the effect of non-cubic part of the crystal electric field. Let us analyse the case of a tetragonal distortion of the oxygen octahedra caused by the deviation of the B–O1–B' basal angle off 180°, say V_{tetra}.

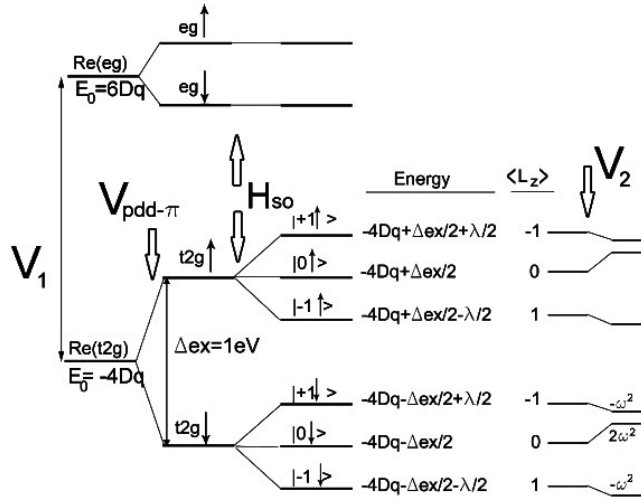$$V_{CEF} = V_{cubic} + V_{tetra} \tag{36}$$

55

Figure 30. Energy levels diagram of a Re t_{2g} degenerate state under the exchange splitting due to the kinetic terms of the Hamiltonian that give rise to the pdd–π coupling and the spin–orbit splitting. The first order correction to the energy and the l_z values for the corresponding zeroth order eigenfunctions are shown (see the text). V_{cubic} corresponds to a cubic electric field and V_{tetra} to a tetragonal distortion entailing an expansion of the ReO$_6$ octahedra in the z quantization direction.

where V_{cubic} stands for the cubic crystal field and V_{tetra} for the distortion from cubic. The expected values of V_{cubic} are $-4Dq$ and $6Dq$ for t_{2g} and e_g subspaces respectively. One can readily see that V_{tetra} in basis $\{t_{2g}\}$ is diagonal for every tetragonal distortion which could be indexed in an I-type lattice, because the mirror symmetries are preserved by such a space group. On the other hand, the diagonal terms can be estimated using simple electrostatic arguments and taking into account the shape of the charge distribution in the t_{2g} state, as done by Oikawa *et al* [38]. Let ε_{yz}, ε_{zx} and ε_{xy} be the diagonal terms of the matrix that represents V_{tetra} in the $\{|d_{yz}\rangle, |d_{zx}\rangle, |d_{xy}\rangle\}$ ($\uparrow$ or $\downarrow$) basis. Then, V_{tetra} has the following expression in the basis just described in equation (35)[4]:

$$V_{\text{tetra}} = \frac{1}{2} \begin{pmatrix} \varepsilon_{yz} + \varepsilon_{zx} & 0 & \varepsilon_{zx} - \varepsilon_{yz} \\ 0 & 2\varepsilon_{xy} & 0 \\ \varepsilon_{zx} - \varepsilon_{yz} & 0 & \varepsilon_{yz} + \varepsilon_{zx} \end{pmatrix}. \tag{37}$$

Therefore, $H_{\text{so}} + V_{\text{tetra}}$ can be simultaneously diagonalized, which is not the case in the presence of a monoclinic distortion. We can speculate about the effect of the tetragonal distortion entailing an expansion of the ReO$_6$ octahedra in the z direction and a compression of the Re–O distances in the basal plane. The $|d_{xy}\rangle$ states lying on the basal plane would become energetically less favourable due to the Coulomb interaction with the negatively charged ligands ($\varepsilon_{xy} = \varepsilon^2 > 0$). At the same time, $|d_{zx}\rangle$ and $|d_{yz}\rangle$ would decrease their energy by the same amount ($\varepsilon_{yz} = \varepsilon_{zx} = \varepsilon^2/2 < 0$), because they only differ in a 90° rotation around the z axis, against which V_{tetra} is also invariant. Thus, if we use the B–O–Re tilting angle, ω, to quantify the strength of the tetragonal distortion, V_{tetra} in basis (35) could be approximately described by (see footnote 4):

$$V_{\text{tetra}} \propto \omega^2 \begin{pmatrix} -1 & 0 & 0 \\ 0 & 2 & 0 \\ 0 & 0 & -1 \end{pmatrix}. \tag{38}$$

---

[4] We have omitted the spinor space.

The energy shift driven by V_{tetra} is shown in figure 30. The tetragonal distortion decreases the energy of the ground state, $|-1\downarrow\rangle$, whereas the energy of the first excited state $|0\downarrow\rangle$ is increased. Therefore, the tetragonal distortion can modify $\langle l_z \rangle$, as well as the relative weight of the d_{yz}, d_{zx}, and d_{xy} orbitals in the ground state. The three states lying at the lowest energy, $|t_{2g}\downarrow\rangle$, will be strongly hybridized with the oxygen and the B site state via the pdd–π hopping interaction. Therefore, the energy diagram proposed in this subsection for Re is far from being an accurate description of the electronic structure in Re-based double perovskites. It just provides an input for band structure calculations, which would clarify the effect of the strong spin–orbit coupling in Re. However, we think that the energy diagram shown in figure 30 is very useful in order to explain, at least qualitatively, the magnetostructural effects that will be presented in the following. At this stage, it is worth recalling the approximations carried out so far:

(i) $\langle t_{2g}|H_{so}|e_g\rangle \approx 0$ allows us to use the T–P isomorphism. This assumption is reasonable, since the CEF splitting in Re is around 3–4 eV [43], while the maximum spin–orbit splitting amounts only to 0.37 eV (see equation (32)). In other words, $V_{cubic} \gg H_{so}$.

(ii) $\Delta'_{ex} \gg \lambda$ allows us to apply the first order perturbation theory to the degenerate $|t_{2g}\uparrow(\downarrow)\rangle$ states. This assumption is only partially accomplished, since $\Delta_{ex} \sim 1$ eV and $\lambda \sim 0.25$ eV [178]. Therefore, it is necessary to consider the off-diagonal boxes in equation (34).

(iii) $H_{so} \gg V_{CEF} - V_{cubic}$ would allow us to apply the first order perturbation theory to the spin–orbit split $\{|1\rangle, |0\rangle, |-1\rangle\}$ states (see equation (35)) in the case of monoclinic distortions or non-centrosymmetric tetragonal distortions. In the above considered tetragonal distortion this approach is not required.

Provided that these assumptions hold true at some extent in Re-based double perovskites, the main conclusions that can be extracted are the following:

(1) $\langle l_z \rangle \neq 0$ in Re-based double perovskites, even in the cubic compounds with $V_{tetra} \approx 0$. Therefore, strong magnetostructural effects can be anticipated [22, 174].

(2) There is a strong tendency to occupy the $\langle l_z \rangle = 1$ and $\langle s_z \rangle = -1/2$ magnetic state that results from the spin–orbit coupling corrections to the t_{2g} spin down states. Our simple analytical approach is in perfect agreement with first principles investigations of the band structure by Jeng *et al* [177], who took into account the relativistic Hamiltonian, and therefore the spin–orbit coupling.

(3) The spin polarization at the Fermi level, $P < 1$. This is due to the mixing up of t_{2g} spin down and spin up states induced by the off-diagonal boxes of the spin–orbit matrix given in equation (34). Recent band structure calculations also led to similar conclusions for the Sr_2CrReO_6 system [45, 183].

(4) Both H_{so} and V_{tetra} split the t_{2g} unperturbed ground states. Interestingly, the first excited state, $|0\rangle$, has zero hybridization probability via pdd–π, because it is built with a pure $|l_z| \neq 0, 1$ state (see section 1.2 and equation (5)). As a consequence, as a function of Δ'_{ex} and the tetragonal distortion, a localization of part of the two Re electrons can occur. An increase of Δ'_{ex} favours the localization because approximation (ii) is better fulfilled, while the increase of the distortion pushes the ground and first excited away from each other (see figure 30). In particular, this justifies the carrier density at the Fermi level $n_e \approx 1$, suggested in section 3.1.1) for $Sr_{2-y}Ba_yFeReO_6$ in spite of the two unpaired electrons of Re^{5+}.

The structural distortion of the cubic crystal field, $V_{CEF} - V_{cubic}$, can vary the value of l_z, by simply adjusting the relative amount of states with different l_z at the ground state. For

example, an increase of the V_{tetra} distortion given by equation (38), at fixed Δ'_{ex}, will increase l_z since V_{tetra} pushes up in energy the first excited state, $|0\downarrow\rangle$, which has $\langle l_z \rangle = 0$. Indeed, XMCD measurements [176] have shown that the orbital moment in Re is strongly dependent on the A cation size in A_2FeReO_6.

3.1.3. Magnetostructural coupling. In section 3.1.2 we show how the Re atom, contrary to the case of 3d (Fe, Cr) and 4d (Mo) elements, can carry a significant orbital moment owing to the large spin–orbit coupling constant distinctive of 5d elements. In the following, the low temperature magnetic and transport properties are discussed from the point of view of the orbital moment borne by the Re atom. The perturbation theory presented in the previous subsection will suffice to provide a physical basis for the interpretation of the low temperature structural, magnetic and magnetotransport properties.

In Ca_2FeReO_6, a second structural and magnetic transition was observed at $T_{\text{sm}} < T_C$ by means of neutron powder diffraction [38, 39]. This transition can be considered as a hint of the coupling between the structural and magnetic degrees of freedom. Below 200 K, the (040) nuclear reflection of the $P2_1/n$ space group shows a splitting that can only be ascribed to the appearance of two crystallographic phases with the same unit cell but slightly different lattice parameters. Consistently, Granado *et al* [173] reported the same mesoscopic phase separation in a wide temperature range. They also compared the individual behaviour of the lattice parameters and the direction of the spontaneous magnetization, $\hat{m}$, with temperature. Above $T_{\text{sm}} \approx 150$ K, $\hat{m}$ in the majority phase (hereafter will be referred to as the high temperature phase or HT phase) lies on the *ac* plane, $55°$ off the *a* axis. By inspection of figure 27, we notice that in Ca_2FeReO_6 at room temperature, *a* and *c* contract, whereas *b* expands. The relative percentage of the secondary phase at high temperatures sharply increases below T_{sm}, and becomes the majority phase (hereafter low temperature phase or LT phase). On cooling, the lattice parameters of the HT phase show a smooth negative thermal expansion in the case of *a* and *c*, and positive in the case of *b*. Compared to the HT phase, the LT phase has a slightly expanded *ac*-plane and a significantly shrunk *b* parameter. More interestingly is the fact that $\hat{m}$ in the LT phase is nearly parallel to the *b* axis. Thus, it seems that the easy magnetization axis could be determined by an inverse magnetostriction effect (Villari effect), in which the strain induced by the lattice distortion sets the magnetic anisotropy. The most common mechanism explaining magnetostriction effects requires an orbital anisotropic electron charge density, which produces a preferential orientation of l_z as a function of the structural distortion, and a spin–orbit interaction that couples the orbital and spin magnetic moments. Therefore, the change of the easy magnetization direction provides further support for the existence of a finite orbital moment, which has been anticipated in the previous subsection. Another experimental example of the coupling between the lattice and spin degrees of freedom in the family of Re-based double perovskites can be found in the Ba_2FeReO_6. When probed by means of conventional XRD, Ba_2FeReO_6 remains in the undistorted *Fm3m* cubic structure at all the temperatures [21, 22, 184]. However, by the use of high flux x-ray radiation from a synchrotron beam line, the development of a small tetragonal distortion ($t = 1.6 \times 10^{-3}$ and 1×10^{-3} at 14 K and 200 K respectively) has been observed exactly below the ferromagnetic ordering temperature, $T_C \sim 315$ K [175].

The LT phase and HT phase were also detected by Oikawa in Ca_2FeReO_6 [38]. Such study did not evidence phase coexistence, but a complete magnetostructural transition from the LT phase to the HT phase that takes place at $T_{\text{sm}} = 140$ K. This means that the appearance of either a LT and HT phase coexistence or a phase transition from LT to HT is sample dependent. The common feature is that the LT phase is strongly favoured below $T_{\text{sm}} \approx 150$ K. We speculate that two phases with a very similar free energy can be very sensitive to synthesis conditions,
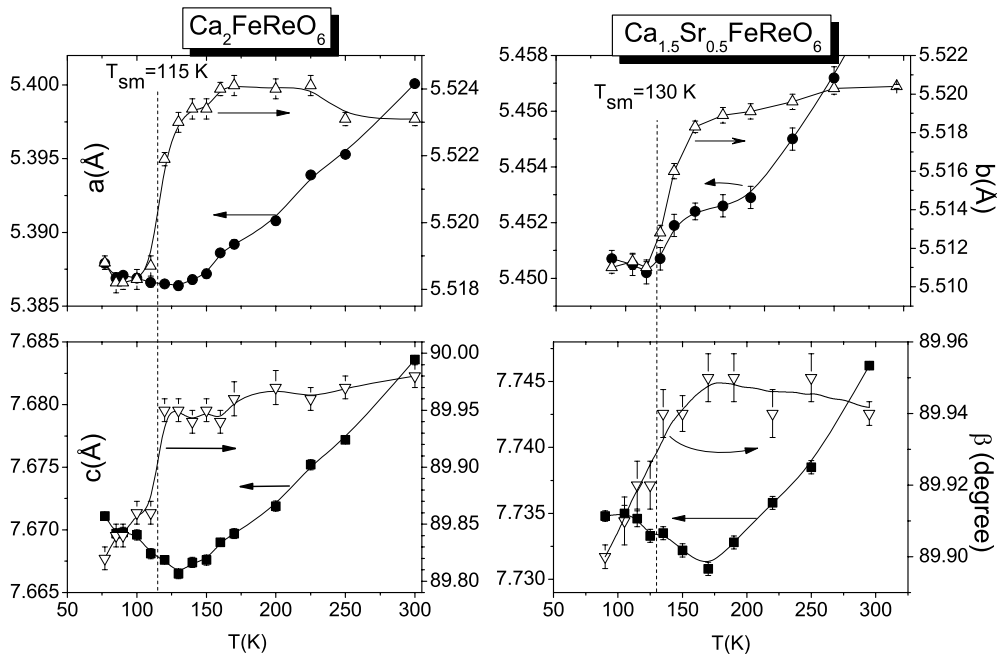
Figure 31. Temperature dependence of the cell parameters for Ca_2FeReO_6 (left) and $Ca_{1.5}Sr_{0.5}FeReO_6$ (right): a (,), b (8), c (!) and $\beta(X)$. Data obtained by XRD.

which can modify the defects concentration and make the minority phase corresponding to each temperature range unstable. Our magnetic and structural measurements at low temperatures support the presence of a magnetostructural transition in monoclinic A_2FeReO_6 compounds. The left panel of figure 31 shows the temperature dependence of the lattice parameters of Ca_2FeReO_6. Our x-ray data do not allow discerning whether there is phase coexistence or phase transition, but a considerable b shrinkage accompanied by a slight ac expansion is clear. Figure 31 also compares the structural parameters of the Ca_2 sample with those of $Ca_{1.5}Sr_{0.5}$. The same trend is observed in both samples, although in $Ca_{1.5}Sr_{0.5}$ the transition is smeared out in a larger temperature range. The main difference is the T_{sm} value, which amounts to 115 and 130 K for Ca_2 and $Ca_{1.5}Sr_{0.5}$ respectively. The temperature dependences of the lattice parameters are in agreement with previously reported data [38, 173], which suggests that the LT phase is present in both Ca_2FeReO_6 and $Ca_{1.5}Sr_{0.5}FeReO_6$ below T_{sm}.

According to Oikawa *et al* [38], the structural transition at T_{sm} entails a distortion of the ReO_6 octahedra, which changes from a compressed octahedra along the c axis (z direction) above T_{sm} to an expanded octahedra along the b axis (y direction) below T_{sm}. In equation (38) and figure 30 it is shown how the perturbed t_{2g} states with orbital moment pointing in the same direction as the expanded axis lower their energy. The preferential occupation of certain t_{2g} orbitals will determine the orbital moment direction and, as a consequence, the spin moment direction through the spin–orbit coupling. The reported variation of $\hat{m}$ towards the b direction in the LT phase is therefore a natural consequence of the structural transition combined with the spin–orbit coupling. The change of the magnetic configuration at T_{sm} is clearly reflected in the anomaly of the ac susceptibility, χ_{ac}, as shown in figure 32. The anomaly is centred around 115 and 130 K for Ca_2 and $Ca_{1.5}Sr_{0.5}$ samples respectively. These are exactly the same temperatures at which the structural transition depicted in figure 31 takes place. In conclusion, we detect a magnetostructural transition in $Ca_{1.5}Sr_{0.5}FeReO_6$ and $CaSrFeReO_6$ similar to the one studied

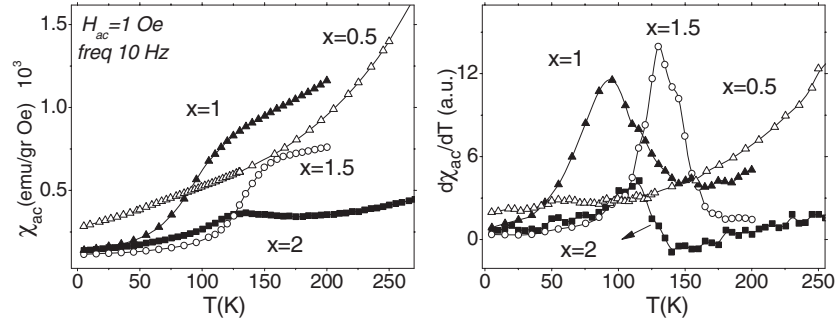**Figure 32.** Left: AC susceptibility measurements in $Ca_xSr_{2-x}FeReO_6$ showing the structural/magnetic transition at $T_{sm} = 115$ K for $x = 2$ (solid squares), 130 K for $x = 1.5$ (open circles), and 96 K for $x = 1$ (solid triangles). The sample with $x = 0.5$ (open triangles) does not show any anomaly. Right: Derivative with respect to the temperature of the AC susceptibility. T_{sm} has been taken as the temperature for which χ_{ac} has maximum slope.
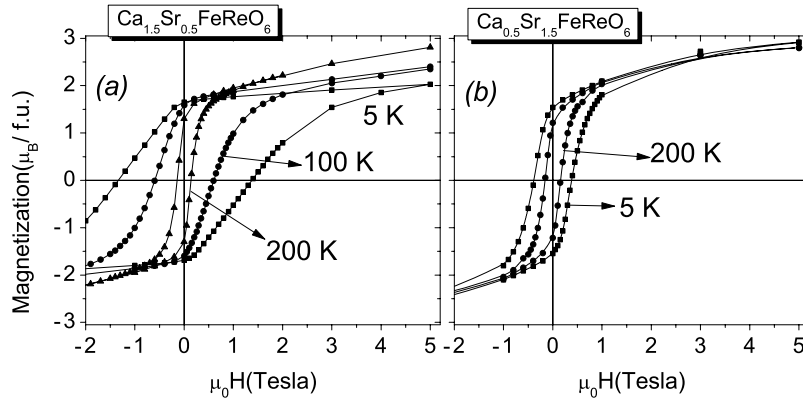

Figure 33. Magnetization loops at selected temperatures for $Ca_{1.5}Sr_{0.5}FeReO_6$ (a) and $Ca_{0.5}Sr_{1.5}FeReO_6$ (b).

exhaustively in Ca_2FeReO_6. In the $Ca_{0.5}Sr_{1.5}$ compound the anomaly in χ_{ac} vanishes. We think that the existence of the magnetostructural transition from the LT phase to the HT phase is connected with the extent of the monoclinic distortion, which is known to increase as the Ca content does (see figure 27). The monoclinic distortion should be large enough to stabilize the Re t_{2g} states with orbital moment along the b axis (notice this state would correspond to $|-1\downarrow\rangle$ in equation (35) if we would have chosen y as the quantization axis) as the ground states.

The change of the easy magnetization axis in the LT phase brings about a remarkable enhancement of the magnetic anisotropy. In figure 33 we compare the magnetization loops at temperatures above and below T_{sm} in two selected compounds. In the case of the $Ca_{0.5}Sr_{1.5}$ compound, which does not show any trace of magnetostructural transition, the behaviour is the expected one for a ferromagnetic material, with slightly larger magnetization and coercivity at 5 K than at 200 K owing to the suppression of the thermally activated domain wall movement. However, the behaviour of $Ca_{1.5}Sr_{0.5}$, with $T_{sm} = 130$ K, is drastically different. First, the magnetization under 5 T decreases below 100 K. Secondly, the coercive field is one order of magnitude higher at 5 K than at 200 K. Due to the presence of a substantial orbital moment in Re-based compounds, an increase of the intrinsic magnetocrystalline anisotropy can explain the enormous coercivity enhancement in the samples that undergo the magnetostructural

transition [22]. When the LT phase appears on cooling below T_{sm}, the compound becomes magnetically harder because $\vec{m}$ is parallel to the b axis instead of lying in the ac-plane, defining thereby a uniaxial anisotropy direction.

By means of optical and electronic conductivity measurements, Kato *et al* [34] correlated the magnetostructural transition with a metal–insulator transition. The insulating nature of the LT phase could be understood by a gap opening owing to the impact of the V_{tetra} change in the energy levels sketched in figure 30. The idea of a simultaneous electronic localization and a rearrangement of the orbital moment below T_{sm} suggests the concept of orbital ordering for the Re t_{2g} electrons. According to Granado *et al* [173], the LT phase fraction in Ca_2FeReO_6 is proportional to the intensity of the (001) weak reflection which is forbidden by the $P2_1/n$ symmetry. Whether this peak has a nuclear or a magnetic origin is not clear, but it could be the hint of the appearance of an orbitally ordered pattern. X-ray resonant scattering at the (001) reflection could shed some light on this issue.

In magnetic oxides, magnetostriction effects are normally small because the orbital moment is almost quenched. However, giant volume magnetostriction effects have been measured in the paramagnetic phase of colossal magnetoresistance manganites [185]. Also, giant anisotropic magnetostriction effects have been observed in certain oxides when instabilities of the orbital degrees of freedom play an important role [186]. The magnetostriction effects observed in $Ca_xSr_{2-x}FeReO_6$ and $Ba_ySr_{2-y}FeReO_6$ cannot be classified in any of the previous groups. The scenario in Re-based double perovskites is more similar to the case for rare earth intermetallic compounds, where the combined action of crystal field effects and a large spin–orbit coupling can lead to considerable effects [187]. The unquenched orbital moment at the Re site provides the basis for the existence of a significant interplay between the spin moment and the lattice strain, which we will study from the scope of the macroscopic magnetostriction. The magnetostriction is the deformation suffered by a material when it becomes magnetized. In the case of single ion crystal field contribution to the magnetoelastic Hamiltonian, the magnetostriction is driven by a double mechanism [187]: the crystal electric field couples the anisotropic electron charge density with the lattice, and the spin–orbit interaction couples the spin and orbital magnetic moments. Other more complex mechanisms can also produce substantial magnetostriction, such as the exchange contributed magnetostriction or the forced magnetostriction [188]. Spontaneous volume magnetostriction effects are observed when a material acquires a long range magnetic ordering, because the lattice strains itself in order to minimize the magnetoelastic energy and reach a thermodynamical equilibrium state. When the magnetostriction is produced by the magnetization process under an applied magnetic field, there are two independent strain magnitudes: the relative length deformation in the parallel direction to the field, $\lambda_\parallel = \delta L_\parallel / L_0$, and the relative length deformation in any direction contained in the plane perpendicular to the field, $\lambda_\perp = \delta L_\perp / L_0$. One can define the volume magnetostriction as the relative volume change, $\omega = \delta V / V_0$, and the anisotropic magnetostriction as the overall shape change, λ_t. In a polycrystalline specimen:

$$\begin{aligned} \omega &= \lambda_\parallel + 2\lambda_\perp \\ \lambda_t &= \lambda_\parallel - \lambda_\perp. \end{aligned} \tag{39}$$

First, we survey the magnetostriction in the compound Ba_2FeReO_6, which crystallizes in the $Fm3m$ cubic space group at room temperature. As depicted in figure 30, the spin–orbit splitting of the t_{2g} spin down states provides a low lying hybridized level with $\langle l_z \rangle \neq 0$, even in the absence of any deviation off the cubic space group. Consequently, an anisotropic local charge distribution in the Re ion can be anticipated. Under an applied magnetic field, H, the localized Fe spin moment (which is the majority moment, $\mu_{Fe} = 5\,\mu_B/\text{f.u.}$) will align parallel

to H. Then, the spin moment of the hybridized $t_{2g}\downarrow$ sub-band will align antiparallel to the Fe localized moment via the strong Hund's coupling. Therefore, as the spin and orbital moments couple antiparallel to each other (see figure 30), the Re orbital moment will be parallel to H. As a consequence, the lattice will deform in order to accommodate the new direction of the orbital moment and minimize the magnetoelastic energy. The magnetoelastic Hamiltonian is usually treated from a phenomenological point of view. If we collect structural data of the A_2FeReO_6 around magnetic transitions, a general magnetoelastic coupling pattern can be inferred from the observed spontaneous magnetostriction: the lattice experiences a shrinkage in the direction in which the magnetic moment is aligned. First, the magnetic easy axis in the Ca_2 compound rotates towards the b direction [38] at T_{sm}. As explained above, this is a natural consequence of the ReO_6 octahedra expansion in this direction. Moreover, as shown in figure 31, the b lattice parameter contracts at the same temperature. Second, the same mechanism can be appreciated in the lattice deformation undergone by Sr_2FeReO_6 at T_C (see figure 47). In this case, the ReO_6 octahedra contracts along the c direction (the Re–O3 distance decreases whereas Re–O1 expands). The alignment of the magnetic moment parallel to one of the two expanded Re–O distances would be energetically favourable as depicted by figure 30. Notice that the a lattice parameter, contained in the expanded ReO_6 basal plane in which the magnetic moment lies, is remarkably contracted below T_C in figure 47(a). What is more, in a recent report on the structural properties of Ba_2FeReO_6, a tiny tetragonal distortion at T_C has been observed [175] below our experimental resolution. One can check that such a distortion does not only entail a contraction of the c axis, but also an expansion of the ReO_6 in the c direction. Thus, we expect that this expansion gives rise to a spontaneous magnetization mostly parallel to the c axis. This fact reflects again the relationship between the spontaneous strain and the magnetization direction, which holds true even in the apparently $Fm3m$ cubic compounds in which very small lattice deformations can only be sensed in high resolution experiments [175].

Therefore, one can safely assume that the complex magnetoelastic coupling that we have just described leads to a negative strain in the direction of the total magnetic moment. As a consequence, we expect a negative $\lambda_\parallel$ and a positive $\lambda_\perp$ when the Zeeman energy is modified by the presence of an external magnetic field. Indeed, in figure 34 we observe that $\lambda_\parallel$ is negative at all the temperatures, whilst $\lambda_\perp$ is always positive. Now we combine $\lambda_\parallel$ and $\lambda_\perp$ as described in equation (39) in order to obtain the volume and anisotropic magnetostriction. As can be noticed in figure 35, ω and λ_t gradually increase on cooling. The anisotropic contribution is as large as -500 μst at the lowest temperature. A large orbital component of the magnetic moment in Ba_2FeReO_6 can account for such a large anisotropic deformation. In fact, the anisotropic magnetostriction arises from the minimization of the single ion magnetoelastic coupling [189, 190] mediated by the CEF interaction with the orbital degrees of freedom. Therefore the existence of a significant λ_t can be ascribed to the unquenched Re orbital moment. This becomes clear when looking at the magnetostriction of the $Ba_{1.6}Sr_{0.4}FeMoO_6$ isostructural compound, shown up to 2 T in the inset of figure 35. In this compound, without the presence of the Re atom, we observe a zero λ_t at all the temperatures. λ_t up to 30 T at 4.2 K measured under pulsed fields is also zero (not shown here).

Owing to the magnetic hardness of monoclinic Ca_2FeReO_6 compound, its magnetostriction has been measured in the pulsed field facility. Superimposed to the above mentioned volume and anisotropic magnetostriction, in Ca-rich compounds additional features appear at low temperatures due to the structural/magnetic transition taking place at T_{sm}. We will illustrate the phenomenology with the data corresponding to the Ca_2FeReO_6 compound [174]. We point out that, as in the case of Ba_2FeReO_6, the Ca-rich compounds show $\lambda_\parallel < 0$ and $\lambda_\perp > 0$. The left panel of figure 36 displays the ω and λ_t isotherms of Ca_2FeReO_6 up to 20 T at selected temperatures. Above $T_{sm} = 115$ K, Ca_2FeReO_6 shows a magnetostriction behaviour similar to
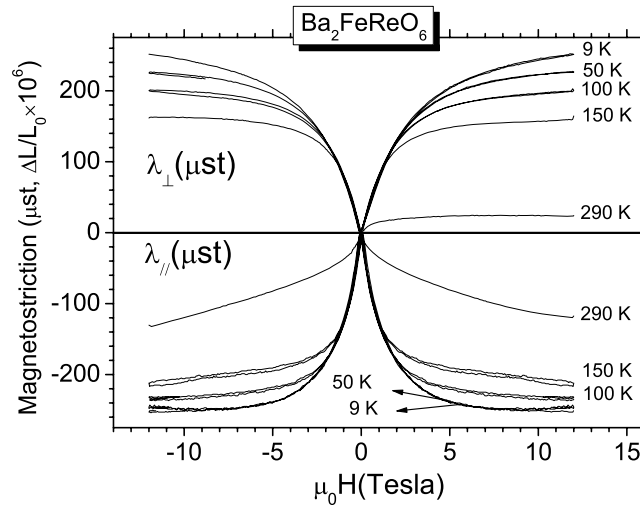
Figure 34. Magnetostriction measurements by the strain gauge method parallel ($\lambda_\parallel$) and perpendicular ($\lambda_\perp$) to the applied magnetic field at selected temperatures in Ba_2FeReO_6. Hereafter, the unit of measurement of the strain will be the *microstrain* ($\mu st = \Delta L/L_0 \times 10^6$), namely parts per million of the deformation with respect to the zero field length.
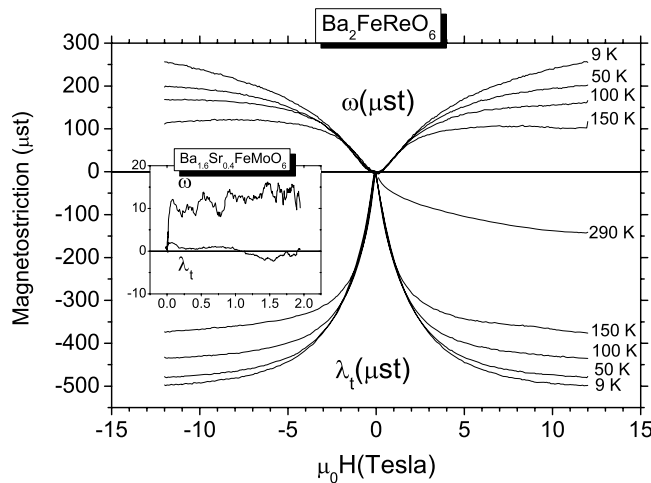

Figure 35. Volume magnetostriction (ω) and anisotropic magnetostriction ($\lambda_\perp$) at selected temperatures in Ba_2FeReO_6. The inset shows the magnetostriction data at 4.2 K of $Ba_{1.6}Sr_{0.4}FeMoO_6$.

that of Ba_2FeReO_6. The only differences with respect to this compound are an enhanced saturation magnetic field and twice as much the absolute value of the saturated λ_t. For instance, at 150 K in Ba_2FeReO_6, λ_t becomes saturated around 6 T, the saturation value attaining $-380\ \mu st$ (see figure 35). In contrast, the saturation field for the Ca_2 compound amounts to about 15 T, whilst $\lambda_t = -830\ \mu st$. The enhanced anisotropic magnetostriction found in Ca_2FeReO_6 correlates perfectly with the existence of a preferential direction for the orbital moment owing to the monoclinic distortion (see section 3.1.2), as well as with the reported coercivity raise when the A site radius decreases (see figures 28 and 33). In the undistorted Ba_2FeReO_6 the smaller $\langle l_z \rangle$
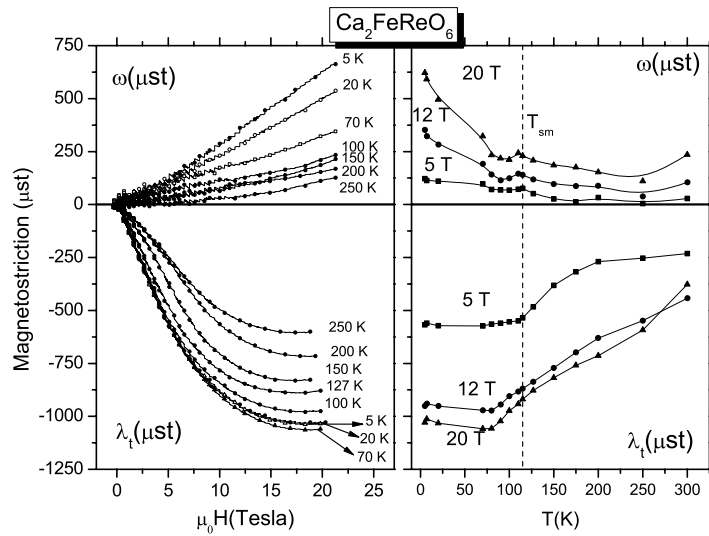
Figure 36. Left: isothermal volume (ω_t) and anisotropic (λ_t) magnetostriction at selected temperatures in Ca_2FeReO_6. Right: volume and anisotropic magnetostriction dependence on the temperature at 5, 12 and 20 T.

together with the absence of noticeable spontaneous lattice distortion can naturally explain the lower value of λ_t. Indeed, Sikora *et al* have reported a systematic l_z increase as the A cation size is reduced from $A_2 = Ba_2$ to $A_2 = Ca_2$ [176]. The volume magnetostriction is much smaller than the anisotropic one, and it shows the same value as in the case of the Ba_2 compound.

Below T_{sm} the temperature dependence of both ω and λ_t are no longer monotonic, the shape of the curves showing striking changes. The effect of the structural transition of Ca_2FeReO_6 on the magnetostriction is better noticed in the right panel of figure 36, where the temperature dependence of ω and λ_t at constant magnetic field are plotted. Incidentally, in Ca_2FeReO_6 ω is relatively important only below T_{sm}. This is connected with the fact that below T_{sm} the application of a magnetic field stabilizes the HT phase, at the expense of the LT phase, as demonstrated in the field dependent neutron diffraction study by Granado *et al* [173]. The neutron diffraction study carried out by Oikawa *et al* [38], in agreement with our own structural study shown in figure 31, unveils that at T_{sm} the unit cell volume undergoes a reduction when changing from the HT phase to the LT phase. According to Oikawa's data, $\Delta V / V_0 \approx -600 \, \mu$st, whereas from our structural data $\Delta V / V_0 \approx -480 \, \mu$st. Therefore, the growth of the HT phase fraction, which has a bigger unit cell than the LT phase, brings about an additional isotropic volume expansion as the magnetic field increases. This contribution superimposes to the intrinsic volume expansion of the HT phase and the LT phase coexisting under strong magnetic fields. The LT phase has not only a smaller unit cell, but also a marked uniaxial magnetocrystalline anisotropy, which produces an enhanced magnetic anisotropy as demonstrated in figure 33. Then, the impact of the structural transition on λ_t is twofold. First, in the LT phase the orbital moment changes its direction from the basal plane to the *b* direction, which can increase λ_t. Second, the coercivity and saturation fields are much larger in the LT phase than in the HT phase, which gives rise to a λ_t reduction when the temperature is lowered at a constant applied field. The trade off between these two competing effects results in an abrupt change of the slope of λ_t versus the temperature at T_{sm}. In addition, in figure 36 it is nicely seen that the application of a magnetic field shifts the transition towards lower
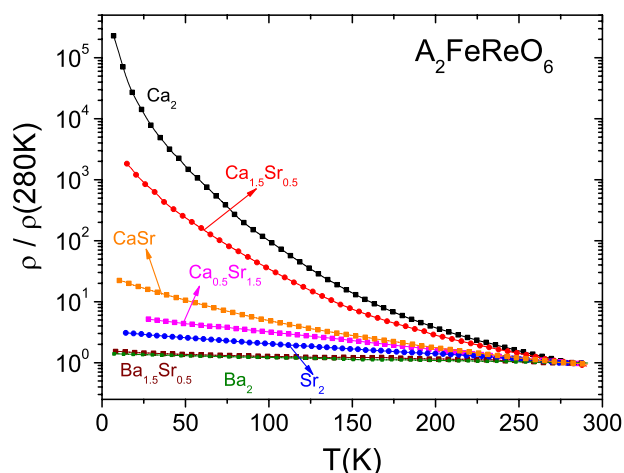
Figure 37. Temperature dependence of the resistivity for A_2FeReO_6 (the data have been normalized to the value at 280 K for the sake of clarity).

temperatures in Ca_2FeReO_6. This is because the system is laid over a place of the phase diagram which is richer in HT phase.

3.1.4. Magnetoresistive properties. The temperature dependence of the normalized resistivity is shown in figure 37. We do not observe any correlation between the absolute value of the room temperature resistivity and the cation size, as in the case of [167]. ρ typically varies between 0.05 and 1 Ω cm, which reflects the metallic character of the bulk A_2FeReO_6 grain at room temperature [34, 35]. The intergrain contribution to the resistance in half-metallic double perovskites changes with the synthesis conditions [35, 111], and can hide the true bulk metallic character of the $Sr_{2-y}Ba_y$ compounds in the temperature dependence of the resistivity. This is why our compounds in the range $y \geqslant 0$ exhibit a slightly temperature dependent resistance, at most a factor 2 between low and room temperature. However, a clear insulating tendency as r_A diminishes is developed. In $Ca_xSr_{2-x}FeReO_6$, the ratio $R(10\,K)/R(280\,K)$ amounts to a factor 10^3 and 10^5 for $x = 1.5$ and $x = 2$ respectively. The loss of metallic character in Ca-rich compounds can be related to the decrease of the pdd–π electronic transfer mediated by t_{2g} states, which weakens due to deviations of the Fe–O–Re angle off 180° in the monoclinic structure. What is more, it might occur that strong monoclinic distortions of the cubic crystal electric field lead to a gapped density of states at the Fermi level [170], as discussed above and illustrated by the energy shift proposed in figure 30. Consistently with this observation, Kato *et al* [34] reported the appearance of an insulating gap of about 0.05 eV at the optical conductivity spectra below 150 K of the $x \geqslant 1.5$ compounds. It must be noticed that those are the compounds showing the strongest monoclinic distortion and the magnetostructural transition below 150 K.

Now we will focus on the magnetoresistance of A_2FeReO_6, which is displayed in figure 38. The discussion applies also for the whole temperature range for the cubic compounds showing metallic behaviour and no trace of monoclinic distortion ($y \geqslant 0$), as well as for the monoclinic compounds ($x > 0$) above T_{sm}. Figure 38 shows the isothermal magnetoresistance at selected temperatures for a cubic compound, Ba_2FeReO_6, and a monoclinic compound above 150 K, Ca_2FeReO_6. We have observed the typical butterfly-like shape of the intergrain tunnelling magnetoresistance (see equation (17)). The hysteresis of the magnetoresistance is due to the
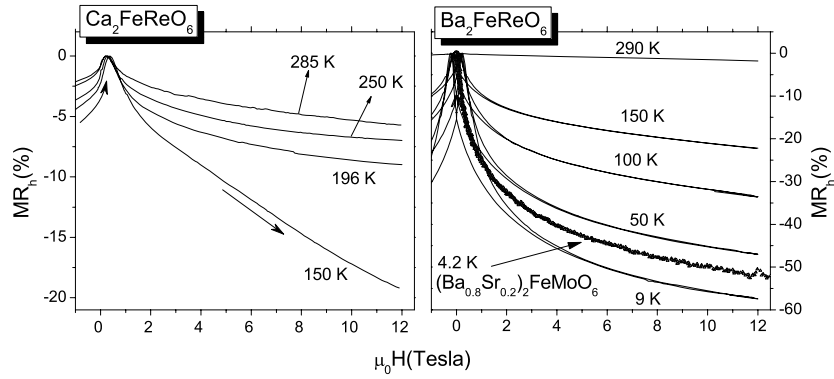
Figure 38. Magnetoresistance measurements of Ca_2FeReO_6 above 150 K and Ba_2FeReO_6 showing the intergrain tunnelling magnetoresistance effect. In the left panel, only half of the loop is plotted for the sake of clarity, and the direction of the field variation is shown with arrows. In the right panel, we have included the MR_h of the Mo-based analogues.

m^2 dependence of the ITMR. Here, the MR_h is defined as $100 \times [\rho(H) - \rho(H_p)]/\rho(H)$, $\rho(H_p)$ being the maximum resistivity as the field is swept. H_p can be viewed then as the coercive field associated with the magnetoresistance. Due to the larger magnetic anisotropy in Re-based double perovskites than in Mo-based ones, the value of H_p at room temperature disallows large ITMR ratios at fields low enough to meet the standard requirements for applications. Nevertheless, our results showing large ITMR in Re-based double perovskites suggest a high degree of spin polarization of the carriers at room temperature, at least comparable to that of A_2FeMoO_6 (see the right panel of figure 38). Those measurements are the first proof of the ITMR effect in $Ca_{2-x}Sr_xFeReO_6$ compounds for $x > 1$ [191]. H_p in the magnetoresistance isotherms is always greater than the coercivity observed in the magnetization isotherms. As explained in section 2.1.3), this occurs because the ITMR is controlled by the magnetic state close to the vicinity grain boundary magnetization, which seems to be different from the bulk one. In particular, the grain surface always exhibit a harder magnetic nature, which can be ascribed to the higher density of defects existing in the vicinity of the grain surface [191]. The magnitude of H_p for the whole x and y range is plotted in the inset of figure 39. We point out that, while in FeMo double perovskites H_p is at most some tens of Oe at the lowest temperatures, the magnetoresistance of Ba_2FeReO_6 and Ca_2FeReO_6 at 250 K peaks at $H_p = 297$ Oe and $H_p = 2280$ Oe respectively. Besides this enhanced magnetic anisotropy, another striking difference between FeMo- and FeRe-based double perovskites is noticed in the main panel of figure 39. A strong decrease of the magnetoresistance with temperature is observed in Ba_2FeReO_6 and Sr_2FeReO_6, in sharp contrast with the behaviour of the Mo-based compound. We have taken the back-extrapolation of the high field slope of MR_h down to zero tesla as the ITMR contribution. Since the ITMR is controlled by the grain boundary magnetization (m_{gb} in equation (21)), these results seem to reflect the higher robustness of the A_2FeMoO_6 surface magnetism against temperature fluctuations.

The low temperature magnetoresistance of monoclinic A_2FeReO_6 compounds shows unexpected large values in the scope of the ITMR model. From equation (17) on readily sees that $-MR_h \leqslant 100\%$. However, we illustrate with figure 40 that at low temperatures, the absolute value of MR_h for $Ca_{1.5}Sr_{0.5}FeReO_6$ is strongly enhanced beyond the limit foreseen for the ITMR effect. The largest MR_h is observed at the lowest temperature, and amounts to -250% at 12 T. While at low fields ($H \leqslant 4$ T) one can notice the butterfly-shaped effect typical
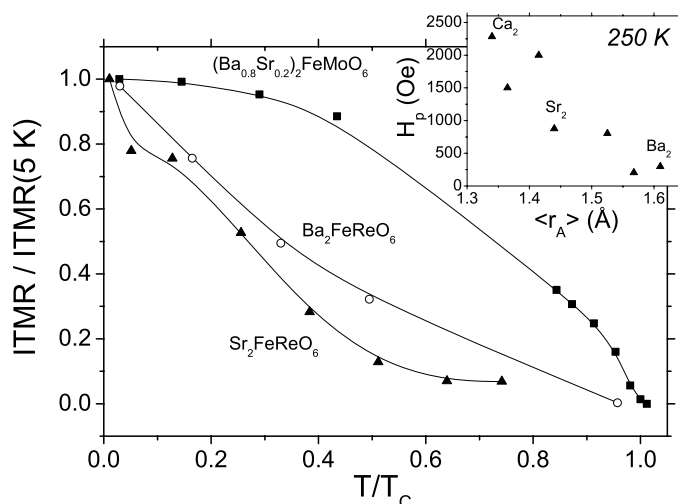
Figure 39. Comparison of the dependence of the intergranular magnetoresistance with temperature in the compounds Ba_2FeReO_6 ($T_C = 305$ K), Sr_2FeReO_6 ($T_C = 391$ K) and $(Ba_{0.8}Sr_{0.2})_2FeMoO_6$ ($T_C = 345$ K). The inset shows the value of H_p at 250 K for all the studied A_2FeReO_6 as a function of the mean ionic radius. ITMR is calculated as the back-extrapolation of the high field slope down to zero field.
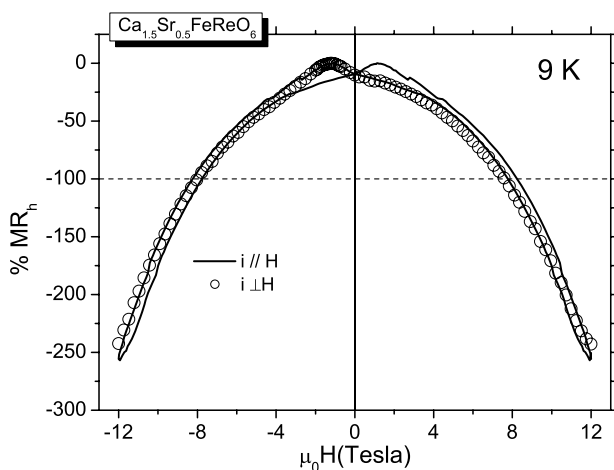

Figure 40. Magnetoresistance at 9 K of $Ca_{1.5}Sr_{0.5}FeReO_6$ measured under steady magnetic fields with the current flowing parallel (line) and perpendicular (open circles) to the field direction. There is no trace of AMR contribution to the magnetoresistance.

of the ITMR, a steep decrease of the resistance occurs at larger fields, which is far from being saturated at 12 T. In figure 40 it is also shown that such an MR effect has an isotropic character, so that a hypothetical contribution due to anisotropic MR can be discarded. We postulate that this effect, which is perfectly systematic and reproducible, can be explained in terms of the LT–HT phase coexistence. The field induced phase coexistence of a metallic (HT) and an insulating (LT) phase might produce a sort of Colossal MR effect if the stable phase under high magnetic fields is the metallic one, as is the case in Ca_2FeReO_6 [173]. The study of this CMR effect in the Ca-rich region up to 50 T will be further addressed in a forthcoming publication [192].
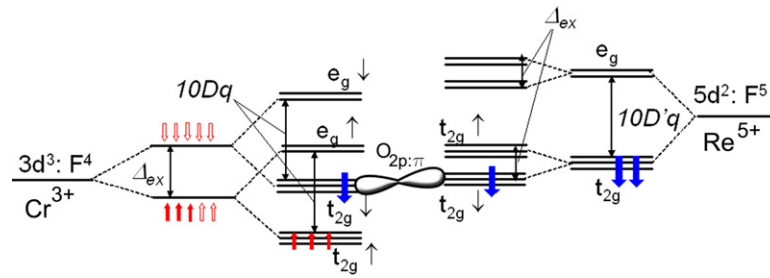
Figure 41. Energy levels diagram of Sr_2CrReO_6 as calculated in [45]. The Fermi level lies at the band formed exclusively by the $Cr(t_{2g}\downarrow)$–$O(2p\pi)$–$Re(t_{2g}\downarrow)$ sub-band.

3.2. $Sr_2(Fe_{1-x}Cr_x)ReO_6$

As previously mentioned, among the double perovskite compounds, the highest T_C has been reported for Sr_2CrReO_6 ($T_C = 625$ K) [36]. Furthermore, interest in this compound has strongly arisen since high quality metallic thin films of Sr_2CrReO_6 can be grown by sputtering techniques. In order to investigate the origin of the mechanism that drives a change of ~220 K in T_C from Sr_2FeReO_6 to Sr_2CrReO_6, we have carried out a thorough neutron diffraction study on $Sr_2Fe_{1-x}Cr_xReO_6$ [27]. This has allowed us to correlate the structural and magnetic properties with the T_C variation across the series.

3.2.1. Phase diagram. We have extracted the sample stoichiometry by means of x-ray diffraction at room temperature and neutron diffraction in the paramagnetic phase at (650–700 K). Our structural results in Sr_2FeReO_6 and Sr_2CrReO_6 coincide with those previously reported at room temperature [28]. We have found that the end compounds ($x = 0$ and 1) have the nominal stoichiometry; whereas for the intermediate compounds two secondary phases of the same structural type exist. Details are given in [27]. Here we discuss the main phase, whose stoichiometry is always closer to the nominal one. The secondary phase is an Fe-rich phase. In the main phase, the antisite level remains very low or unnoticeable (AS ~ 10% for $x = 1$–0.9, ~5% for $x = 0.75$ and ~0% for $x = 0.5$–0). At 650 K all the compounds are cubic ($Fm3m$) and paramagnetic. When decreasing the temperature, two kinds of transitions are detected: the paramagnetic–ferromagnetic transition at T_C and the cubic–tetragonal ($I4/m$) at T_S. T_C is determined as the temperature at which a non-zero magnetic moment appears at the Fe[Cr] site, marking the appearance of long range magnetic order. At T_S the octahedra tilting makes the Fe[Cr]–O1–Re angle to deviate off 180°. In contrast to the behaviour of the pristine Sr_2FeMoO_6, both transitions are clearly decoupled, as occurs in the $Sr_2T_{0.25}Fe_{0.75}MoO_6$ series [24].

In the case of Sr_2FeReO_6, the Fe magnetic moment at low temperature is ~4.5 μ_B, which is the expected value for the high spin configuration of the Fe^{2+}/Fe^{3+} mixed valence state. This is in good agreement with Mössbauer experiments which establish an isomer shift intermediate between the Fe^{3+} and the Fe^{2+} state [21, 167]. In Sr_2CrReO_6 $\mu_{Cr} = 2.52$ μ_B, which also indicates a Cr^{2+}/Cr^{3+} mixed valence state. In the case of Sr_2CrReO_6, the energy levels scheme of figure 3 has to be modified, and turns into that of figure 41. The Cr^{3+} ions possess only 3 electrons in the 3d shell, and therefore the intra-atomic Hund's exchange splitting is less important than in the Fe case, whereas the influence of the crystal electric field must be larger. The $e_g\uparrow$ levels remain empty. Nevertheless, those states cannot participate in the hopping processes with the Re t_{2g} states because they do not share spherical harmonics with the same

orbital symmetry (see equation (5)). *Ab initio* band structure calculations in the Sr_2CrWO_6 compound [13, 177], which has very close lattice parameters to those of Sr_2CrReO_6 (see table 1), show that the Cr $e_g\uparrow$ states lie above the Cr t_{2g} states, as depicted in the left side of figure 41. This is also the case for Sr_2CrReO_6, as shown in the band structure calculations by Vaitheeswaran *et al* [45]. In short, the spin up band is gapped at the Fermi level as is the case for the FeMo and FeRe double perovskites, although the gap is caused by the crystal electric field rather than by the intra-atomic exchange splitting. Therefore, the Cr $t_{2g}\downarrow$ can polarize the Re t_{2g} levels by hybridization through the pdd–π kinetic term of the Hamiltonian, which lowers the energy of the Re $t_{2g}\downarrow$ and creates a spin down polarized conduction band. Such band is populated by the two Re 5d electrons, which will plausibly produce a 2+/3+ mixed valence state in Cr, consistently with our refined Cr magnetic moment and the metallic conductivity of the Sr_2CrReO_6 thin film grown by Asano *et al* [169]. In conclusion, the same kind of double exchange-like mechanism as in Sr_2FeReO_6 operates in Sr_2CrReO_6. Then, what mechanism triggers the enormous T_C increase of the Cr compound with respect to the Fe one?

We will come back later to this question. Now it is worth raising some comments on the Re magnetic moment probed by neutron diffraction. Our refined μ_{Re} is antiparallel to the Cr $t_{2g}\uparrow$ localized spin moment, in agreement with the down spin t_{2g} picture of the conduction band. However, the neutron diffraction profile is quite insensitive to the μ_{Re} absolute values, probably due to the uncertainties in the Re magnetic form factor. For instance, if we use the magnetic form factor of Mo^{3+} instead of Re^{5+}, as done by Auth *et al* [172], we obtain at $T = 5$ K $\mu_{Re} = -0.16(7)$ and $-0.21(11)$ μ_B for Sr_2FeReO_6 and Sr_2CrReO_6 respectively, whereas NMR measurements on Sr_2FeReO_6 indicate $\mu_{Re} = -0.94$ μ_B [19]. The result does not improve by using the magnetic form factors published by Oikawa *et al* [38] and Popov *et al* [16]. In contrast, the Re spin moment extracted from the Re $L_{2,3}$ dichroic signal agrees quite well with the values calculated within the local spin density approximation [45, 179], $\mu_{Re} = -0.75$ μ_B. The general trend is that the experimental μ_{Re} is much lower than the value expected for the ionic picture of -2 μ_B, which reflects the strong hybridization of Re t_{2g} states.

Within the proposed picture of the electronic structure for $Sr_2Fe_{1-x}Cr_xReO_6$, as the Cr content increases, the Fe[Cr] $t_{2g}\uparrow$ sub-band becomes depopulated from five electrons per formula unit for $x = 0$ down to three electrons for $x = 1$. The two 5d electrons provided by the Re ions would occupy mainly the spin down sub-band formed by hybridization of Fe[Cr](t_{2g})–$O(2p_\pi)$–Re(t_{2g}). According to this scenario, the saturation magnetization should linearly decrease with the Cr doping from 3 μ_B/f.u. for $x = 0$ to 1 μ_B for $x = 1$. Our magnetization measurements are consistent with this model. In figure 42, the experimental magnetization loops are shown. The inset displays the linear dependence of the saturation magnetization on the Cr content, which ranges from 2.6 μ_B/f.u. for $x = 0$ to 0.85 μ_B/f.u. for $x = 1$. The slight discrepancy can be ascribed to the AS disorder and the chemical phase segregation which are present in this series [27].

Figure 43(a) shows the dependence of T_C and T_S on the Cr content of the main phase: whereas T_S decreases from ~ 490 K for $x = 0$ to ~ 290 K for $x = 1$, T_C increases from ~ 410 K for $x = 0$ to ~ 620 K for $x = 1$. The tolerance factor given by equation (4) reflects the overall size mismatch of the cations. We measure approximately identical tolerance factor for Sr_2FeReO_6 ($f_{obs} = 0.9960$) and for Sr_2CrReO_6 ($f_{obs} = 0.9992$) according to our neutron diffraction data at 5 K. However, a better cation size matching in Sr_2CrReO_6 is clear from the cation–oxygen distances at 5 K: $\langle d_{Fe-O}\rangle = 2.004$ Å and $\langle d_{Re-O}\rangle = 1.9475$ Å for Sr_2FeReO_6, whereas for Sr_2CrReO_6 we find $\langle d_{Cr-O}\rangle = 1.956$ Å and $\langle d_{Re-O}\rangle = 1.951$ Å. This reflects that the Cr ionic radius is more similar to the Re one than the Fe ionic radius ions. This fact could be anticipated from the tabulated ionic radii [12] of Fe^{3+}, Cr^{3+} and Re^{5+} in VI coordination, which amount to 0.645 Å, 0.615 Å and 0.58 Å respectively. As a result, the pure Cr compound
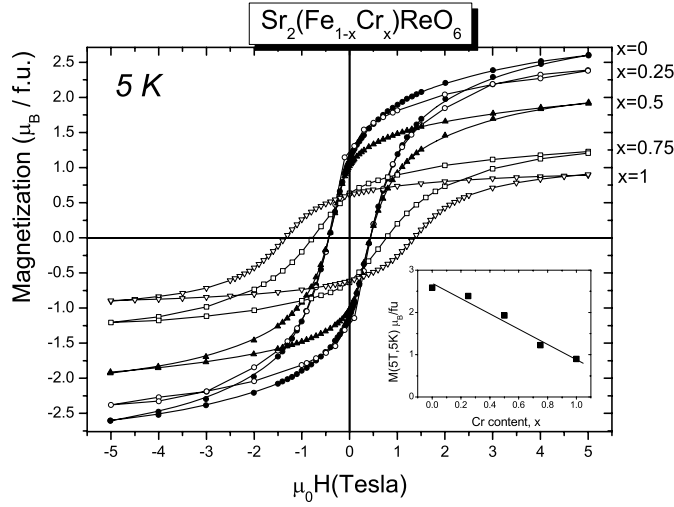
Figure 42. Magnetization isotherms up to 5 T at 5 K of $Sr_2Fe_{1-x}Cr_xReO_6$.

leads to a less distorted structure than the Fe one, and the tetragonal phase is less stable against temperature fluctuations in Sr_2CrReO_6. The AS disorder is, however, enlarged by the approach of the B and B$'$ atomic radii, leading to an AS level below the XRD resolution (2–3%) to an AS = 10% in Sr_2CrReO_6 [27].

The anomalously large increase of T_C in the $Sr_2Fe_{1-x}Cr_xReO_6$ series can be explained by structural and band hybridization effects as discussed hereafter. The local spin density approximation to the electronic structure of A_2FeReO_6 foresees a zero contribution of the Re e_g states to the Fermi level in absence of strong monoclinic distortions of the cubic ligand electric field. In $Sr_2Fe_{1-x}Cr_xReO_6$ the structure at low temperature remains tetragonal for the whole series, and the bond angle stays nearly constant around 171° [27] in the ground crystallographic state. Moreover, recent calculations of the electronic structure of Sr_2CrReO_6 confirm the assumption of a Re e_g sub-band lying well above the Fermi level [45]. This scenario disallows the hybridization of the Cr and Re e_g states, and consequently the additional pdd–σ ferromagnetic coupling postulated for Ca_2FeReO_6 cannot be the driving mechanism of the huge T_C increase in Sr_2CrReO_6. In other words, from the scope of equations (8) and (9), $V_{pdp\pi} \gg V_{pdp\sigma} = 0$ because the $|e'_g\rangle$ are not populated and $\varepsilon'_{eg} \gg \varepsilon'_{t_{2g}}$. Then, only the pdd–$\pi$ interaction operates, and equation (11) turns into:

$$T_C \propto \frac{[r_{Re}^3(r_{Fe}(1-x) + xr_{Cr})^3]^{1/2}}{d_{Fe(Cr)-O}^4 d_{Re-O}^4}. \tag{40}$$

The factor $T(\omega)\eta_{pd\pi}^2$ is absorbed in the proportionality constant, and the muffin-tin orbital radii ($r_d = r_{Fe}$, r_{Cr} and r_{Re}) in equation (6) change as a function of the Cr content, x. The values of r_d are tabulated in [73]. In figure 43(b) we plot the experimental Curie temperature against the right term in equation (40). The linear dependence of T_C as a function of the pdd–π indirect coupling becomes clear, in good agreement with our findings in section 2.1. This is indeed a clear experimental evidence of the validity of the double exchange-like model expounded in section 1.1 for high T_C double perovskites.

3.2.2. Magnetotransport properties at high temperatures.
As in other high T_C double perovskites, the magnetotransport properties are intimately related to the half-metallic character
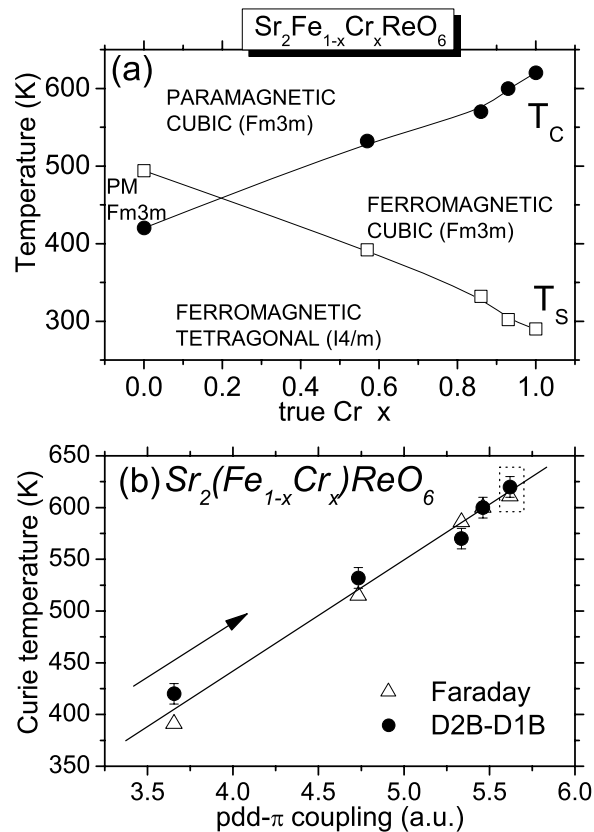
Figure 43. (a) Structural and magnetic phase diagram of the main phase of $Sr_2Fe_{1-x}Cr_xReO_6$ as a function of the true Cr content (the one refined for the main phase). (b) Evolution of the Curie temperature against the strength of the pdd coupling extracted from the structural parameters of the main phase. The Cr content increases in the arrow direction.

of the density of states at the Fermi level. In agreement with the theoretical picture of the electronic structure [44, 45], metallic behaviour has been reported for the end compounds Sr_2FeReO_6 [28, 34] and Sr_2CrReO_6 [28, 36, 169]. We notice that, despite the marked differences in their electronic structure, in both compounds the carriers at the hybridized $Fe[Cr](t_{2g})$–$O(2p_\pi)$–$Re(t_{2g})$ spin down sub-band are responsible for the ferromagnetic interaction and the conduction mechanism. We find a semiconducting-like behaviour with weak temperature dependence owing to the temperature activated conductivity across grain boundaries, which usually occurs in polycrystalline double perovskites. Thus, the absolute resistivity values of Sr_2CrReO_6 are strongly dependent on the porosity of the sample. When performing hot pressing sintering the resulting resistivities in polycrystalline Sr_2CrReO_6 are much lower, typical of a bad metal [36]. Furthermore, Fisher *et al* [193] have reported that the Seebeck coefficient in such a sample increases on warming from low temperatures, which reflects the metallic nature of the electron transport (hole dominated in this case). The overall thermoelectric power is an entirely bulk property, independent of the grain boundaries, and therefore it can be considered as a proof of the bulk metallic behaviour in poorly conducting Sr_2CrReO_6 compact pellets.

The fact that the insulating grain boundaries of our Sr_2CrReO_6 sample have a very important contribution to the resistance anticipates intergrain tunnelling magnetoresistance
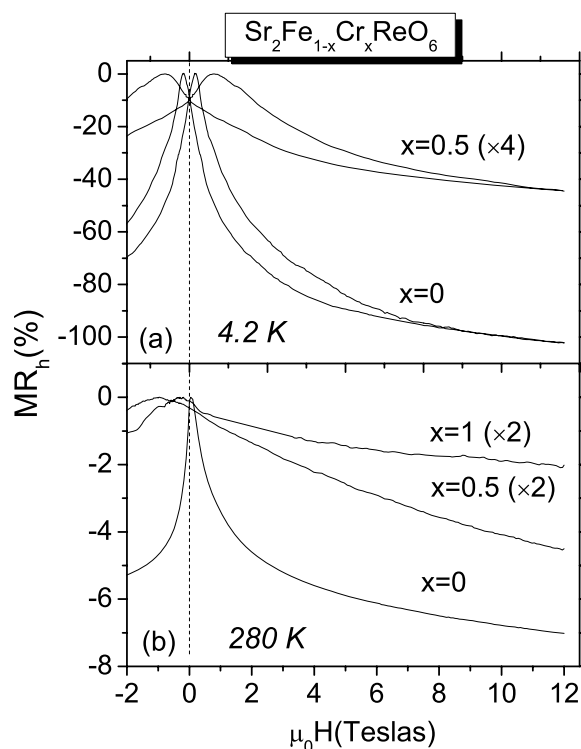
Figure 44. (a) Magnetoresistance of Sr_2FeReO_6 and $Sr_2Fe_{0.5}Cr_{0.5}ReO_6$ at 4.2 K. (b) Magnetoresistance of Sr_2FeReO_6, $Sr_2Fe_{0.5}Cr_{0.5}ReO_6$, and Sr_2CrReO_6 at room temperature. The curves of Cr doped compounds have been magnified for the sake of comparison.

phenomena. ITMR in Sr_2CrReO_6 has been scarcely reported to date, and only at low temperatures [28]. The reason might be its hard magnetic nature (the coercivity at 5 K is as large as 1.5 T, as shown in figure 42), which requires the application of enormous magnetic fields in order to make the magnetoresistance noticeable. Figure 44 depicts the main characteristics of MR_h: at room temperature, a moderate ITMR effect is evidenced by the butterfly-like shape of the magnetoresistance loops, which reflects that the bands lying at the Fermi level must be spin polarized at some extent. At low temperatures the maximum magnetoresistance rates are achieved, and at 12 T they amount to $MR_h = -101\%$ and $MR_h = -11\%$ for Sr_2FeReO_6 and $Sr_2Fe_{0.5}Cr_{0.5}ReO_6$ respectively. Despite the huge T_C of the Cr doped compounds, their MR_h values are very low both at room and low temperatures. According to equation (17), two effects might play a role in this lack of magnetoresistance. One is that, given the large value of the saturation field and H_p, several tesla are required to change m^2 significantly. Indeed, by inspection of figure 44(b), we observe that the H_p value at room temperature in Sr_2CrReO_6 is as large as 0.97 T. The other is a possible reduced spin polarization, P, with respect to Sr_2FeReO_6. This can be understood in the frame of the perturbation treatment developed in section 3.1.2, because the spin down and spin up eigenstates of the unperturbed Hamiltonian are mixed up owing to the finite spin–orbit coupling at the Re atom (see equation (34)). As density functional theory calculations concerns, this effect reduces the theoretical spin polarization at the Fermi level from $P = -1$ (without spin–orbit coupling) to $P = -0.9$ [45, 183].
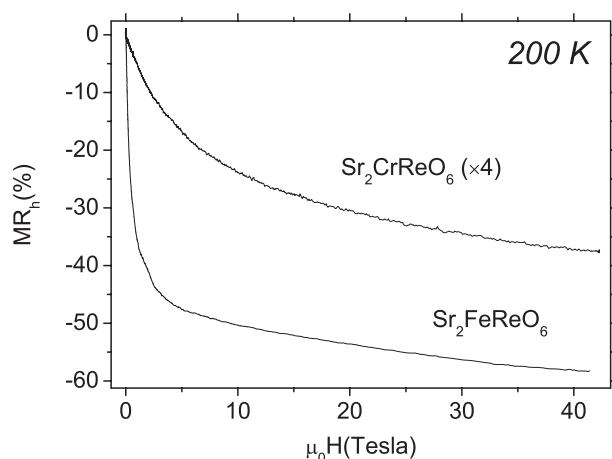
Figure 45. Magnetoresistance under pulsed fields of Sr_2FeReO_6 and Sr_2CrReO_6 polycrystalline compact pellets at 200 K (the curve corresponding to Sr_2CrReO_6 has been magnified four times allowing for comparison).

In order to further investigate the MR response up to magnetic saturation, we have performed transport measurements under pulsed magnetic fields up to 45 T. The result is shown in figure 45. At 200 K the extreme compounds Sr_2FeReO_6 and Sr_2CrReO_6 show the same degree of saturation at 45 T. Nevertheless, the MR_h is definitively smaller in Sr_2CrReO_6, especially at low fields where most of the ITMR contribution is expected. Therefore, we conclude that the effective spin polarization of the tunnelling electrons in Sr_2CrReO_6 is reduced with respect to other archetypal double perovskites, which is detrimental for applications in spintronic devices. Further experiments are being performed in order to check if the magnetoresistance of Sr_2CrReO_6 can be enhanced by modifications of the grain boundary microstructure.

3.2.3. Relevance of the strong spin–orbit coupling in Re. In [45] the relevance of the spin orbit interaction in the electronic properties of Sr_2CrReO_6 is highlighted. First, as hinted by equation (34), owing to the spin–orbit interaction the gap of the spin up sub-band at the Fermi level is closed, and the half-metallic character is not preserved. Second, a non-zero orbital moment arises at the Re atom, which has been confirmed by means of XMCD measurements [179]. In this section we will overview the implications of such an orbital moment for the magnetostructural coupling in $Sr_2Fe(Cr)ReO_6$. At first glance, the pure Cr compound is the magnetically hardest one, as can be noticed in the right panel of figure 46. The coercive field at 5 K is as large as ∼23 kOe. Such a large magnetic anisotropy has been earlier reported for Sr_2CrReO_6 [28] and other Re-based double perovskites as for instance Sr_2MnReO_6 [16] and Ca_2FeReO_6 [22]. We must point out that, according to our experience, the value of the coercive field in this double perovskites is sample dependent, which might indicate that the role of structural defects such as antiphase boundaries [99] as domain pinning centres can be very important in such highly anisotropic compounds. However, the order of magnitude is always preserved (above 1.5 T), which reflects the strong magnetocrystalline anisotropy induced by the spin–orbit coupling at the Re site.

Moreover, as can be appreciated in the left panel of figure 46, the Sr_2CrReO_6 sample undergoes a drop in the ac susceptibility at 160 K that resembles the anomaly associated with the magnetic/structural transition in the monoclinic A_2FeReO_6 compounds (see figure 32).
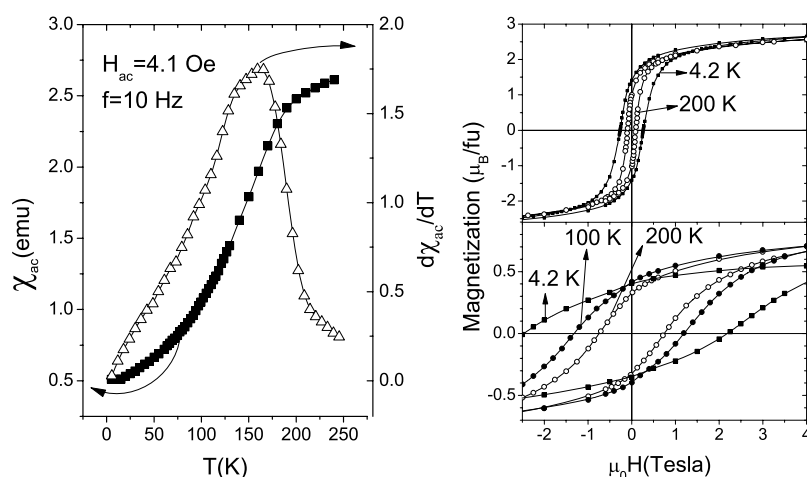
Figure 46. Left: temperature dependence of the ac susceptibility and its derivative for Sr_2CrReO_6. Right: magnetization hysteresis loops at selected temperatures for Sr_2FeReO_6 (top panel) and Sr_2CrReO_6 (bottom panel).

Indeed, if we compare the tracking of the coercivity for Sr_2FeReO_6 and Sr_2CrReO_6 shown in the right panel of figure 46, one easily realizes that a significant coercivity enhancement appears on cooling below 160 K in the Cr compound. This fact suggests that, in analogy with the scenario in A_2FeReO_6, a transition towards a higher magnetic anisotropy state takes place below 160 K. In order to find out whether this transition is driven by a simultaneous structural distortion, we have performed a neutron diffraction study as a function of the temperature in Sr_2FeReO_6 and Sr_2CrReO_6. Two remarkable observations can be noticed in figure 47. First, within our experimental resolution, there is not any structural change at 160 K in Sr_2CrReO_6 (we recall that $T_S = 290$ and 495 K for Sr_2CrReO_6 and Sr_2FeReO_6, as shown in figure 43(a)). Therefore, one must conclude that the magnetic transition observed at 160 K has not a magnetostructural origin. Second, in Sr_2FeReO_6 the ReO_6 octahedra suffer a strong compression in the apical direction below T_S and a relative expansion of 4% of the c axis. On the contrary, the ReO_6 octahedra in Sr_2CrReO_6 remains undistorted down to the lowest temperature. The effect of the distortion taking place in Sr_2FeReO_6 is opposite to the one calculated in the energy diagram of figure 30. The distortion mixes up the ground state ($\langle l_z \rangle = 1$ along the compressed direction) with the first excited state ($\langle l_z \rangle = 0$), or in other words, the magnetocrystalline energy of the system is lower if the orbital moment lies in the basal plane. Thus, as discussed in section 3.1.3 for the HT phase of Ca_2FeReO_6, there is no reason for Sr_2FeReO_6 to show a uniaxial magnetic anisotropy below T_C. The situation in Sr_2CrReO_6 is even simpler, since the ReO_6 octahedra does not change over the whole temperature range, and therefore the perturbation to the cubic crystal electric field, V_{tetra}, is negligible. In conclusion, the magnetic anomaly detected in Sr_2CrReO_6 cannot be ascribed to a magnetostructural transition, at least with measurable structural changes by means of high resolution neutron diffraction.

Nevertheless, in Sr_2CrReO_6, the existence of a large orbital moment in the Re atom is a direct observation through XMCD measurements [179]. In fact, if we compare the experimental orbital moment values extracted from the XMCD spectra of several Re-based compounds [176, 179], and using the estimated number of holes arising from band structure calculations [44], we notice that the Re m_L value in Sr_2CrReO_6 (0.25 μ_B) is comparable to
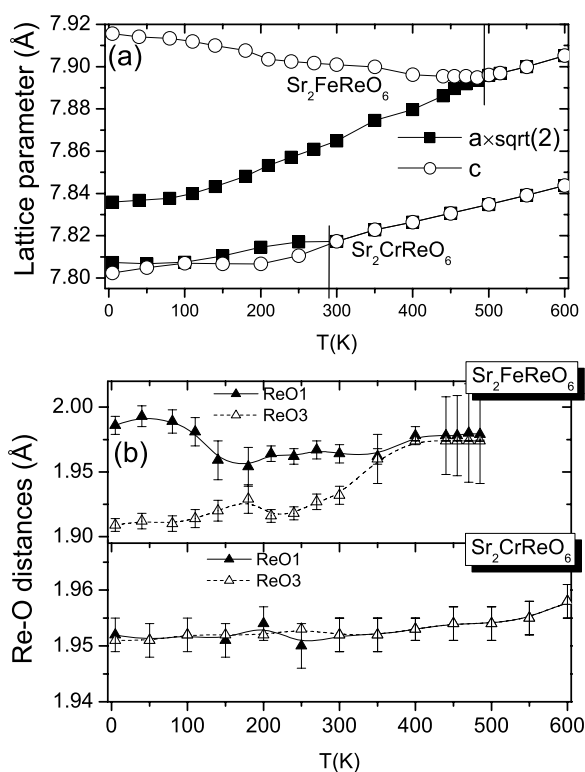
Figure 47. (a) Lattice parameters of Sr_2FeReO_6 and Sr_2CrReO_6 as a function of the temperature. (b) Temperature dependence of the atomic distances between the Re atom and the basal (O1) and apical (O3) oxygens. Data obtained from neutron diffraction experiments performed at D2B (ILL, Grenoble).

those of Ca_2FeReO_6 (0.29 μ_B) and Sr_2FeReO_6 (0.23 μ_B). Therefore, we have searched for further macroscopic evidences of magnetoelastic coupling in $Sr_2Fe_{1-x}Cr_xReO_6$ by measuring the magnetostrictive properties. In both Sr_2CrReO_6 and Sr_2FeReO_6, similarly to the A_2FeReO_6 (see section 3.1.3), the parallel magnetostriction is negative ($\lambda_\parallel < 0$) and the perpendicular magnetostriction is positive ($\lambda_\perp > 0$). We have combined $\lambda_\parallel$ and $\lambda_\perp$ in order to obtain the anisotropic magnetostriction as explained in equation (39). Results for Sr_2CrReO_6 and Sr_2FeReO_6 are displayed in figure 48. The compounds in the range $0 < x < 1$ of the series $Sr_2Fe_{1-x}Cr_xReO_6$ behave halfway between the extreme compounds, depending on the Cr content.

The same underlying physical mechanisms invoked in section 3.1.3 suffice to explain the observed magnetostriction. When the orbital moment rotates towards the direction of a strong enough applied magnetic field, the electrostatic energy can be minimized if the octahedra expands in the direction of the field (see figure 30 and equation (38)). It has been argued in the discussion of the magnetostriction in A_2FeReO_6 that this mechanism entails shrinkage of the cell in the direction of the moment, i.e., the direction of the applied field. Thus, a negative λ_t is naturally explained from the single ion magnetoelastic interaction through the interplay between the crystal electric field, the spin–orbit coupling and the Zeeman interaction. Another remarkable observation is that the λ_t value of Sr_2CrReO_6 is less than half that of Sr_2FeReO_6. This is due in part to the existence of a larger magnetic anisotropy in Sr_2CrReO_6
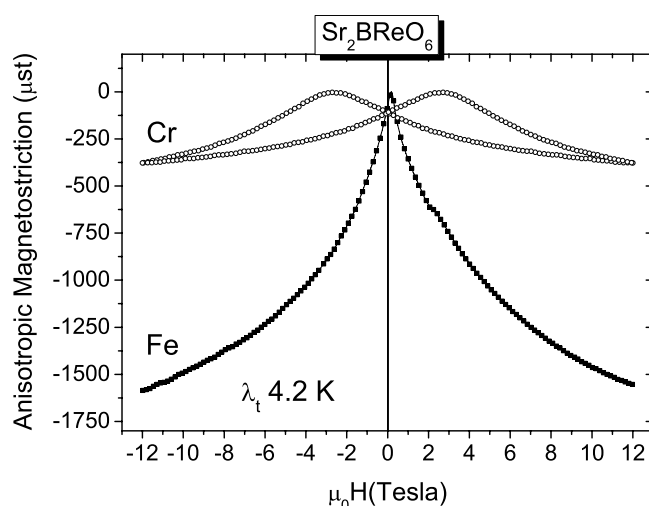
Figure 48. Volume (ω) and anisotropic (λ_t) magnetostriction at 4.2 K of Sr_2CrReO_6 (open circles) and Sr_2FeReO_6 (solid squares).

than in Sr_2FeReO_6, as is evidenced by their respective coercive fields (see figure 46(b)). The same disparity will be held by the saturation fields above which the magnetization is reversible. Indeed, in figure 48 we observe that the hysteresis loop of λ_t in Sr_2CrReO_6 is still fully open at ±12 T. In consequence, the harder magnetic nature of Sr_2CrReO_6 could lead to a reduced λ_t despite its similar orbital moment at the Re site. On the other hand, the lower saturation λ_t could be anticipated from the fact that, contrary to the Sr_2FeReO_6 case, the spontaneous magnetostriction at T_C is unnoticeable in Sr_2CrReO_6 within our experimental resolution (see figure 47). This seems to indicate a weaker magnetoelastic coupling in Sr_2CrReO_6, which leads to magnetostriction values comparable to those of Ba_2FeReO_6. The detailed temperature dependence of the magnetostriction in $Sr_2Fe_{1-x}Cr_xReO_6$ will be reported in a forthcoming publication [194].

4. Perspectives and conclusions

We have reviewed a vast amount of double perovskite compounds showing ferromagnetism up to well above room temperature. All of them exhibit common features such as metallic-like transport in some temperature range, a mixed valence state of the B and B′ sites probed by atom selective techniques, and evidence of a large carrier spin polarization. This is the case for A_2FeMoO_6, A_2FeReO_6, A_2CrWO_6, and A_2CrReO_6. There exists, as proven in table 1, a clear correspondence between the mixed valence state of the B–B′ pairs and the high temperature ferromagnetism. When an integer valence is demonstrated for the B and B′ atoms, the magnetic ordering arrangement is invariably antiferromagnetic or weakly ferromagnetic. This is the case for Sr_2MnMoO_6, A_2MnWO_6, A_2FeWO_6 and A_2CoReO_6. The transition from the former to the latter group has been theoretically and experimentally demonstrated for the $Sr_2FeMo_{1-x}W_xO_6$ B′ site alloyed compounds [35, 66]. We have introduced Sarma's model [42] as the first theoretical explanation of the peculiar DOS of Sr_2FeMoO_6, which accounts for both the fully negative spin polarization at the Fermi level and the stabilization of the high temperature ferromagnetic arrangement of the magnetic transition metal ions in spite of being quite far away from each other ($\sim$7–8 Å). Later on, the model was generalized

for other double perovskite compounds by Fang, Kanamori and Terakura [64, 65]. The key ingredient of the model is the existence of hopping interactions of the valence electrons of the non-magnetic metal (B′ = Mo, Re, W) into the strongly spin down polarized t_{2g} states of the transition metal (B = Cr, Mn, Fe) across the O 2p intermediate states. This hopping interaction is operative whenever the B′t_{2g} states lie in between two d bands with opposite spin polarization (the majority one being filled or partially filled), and gives rise to a spin down polarization of the originally non-magnetic B′t_{2g} states. Since the magnetism in the B′ site is induced by the hybridization with the magnetic B site, the magnetic ordering does not correspond to a ferrimagnetic picture, but to a ferromagnetic one. In fact, as pointed out by Kanamori and Terakura [64], such a hopping mechanism underlying robust ferromagnetism in a group of transition metal compounds diluted with non-magnetic ions entails a rather new mechanism different from other exchange interactions such as Zener's double exchange, RKKY interactions, or even superexchange. This novel mechanism was termed double-perovskite-double-exchange by Sarma *et al* [42]. In order to obtain a simple analytical approach to the double exchange-like ferromagnetic interaction, we have extended the case of p- and d-type orbital hybridization, calculated by Harrison, to the case of the hybridization of two d-type orbitals through an intermediate p-type state, say, the charge transfer across B–O–B′ bonds. Our theoretical framework is supported by numerous experimental evidences, for instance the linear dependence of the Curie temperature on the matrix elements of the kinetic term responsible for the hybridization interaction (see figures 10 and 43), or the increasingly large magnetic moment of the non-magnetic B′ metal as the hybridization mechanism strengthens [10, 117, 176, 179] (see figure 41).

This basic theoretical background paves the way to improving the performances of double ordered perovskites as potential candidates for applications in spintronics technology. For instance, we have shown that electronic band filling of the Fe($t_{2g}\downarrow$)–O(2p)–Mo($t_{2g}\downarrow$) conduction band can enhance the Curie temperature of A_2FeMoO_6 compounds to a fair extent. This band filling is achieved by means of trivalent rare earth doping at the A site. Unfortunately, we have provided evidence of an intrinsic spin depolarization of the conduction band as La^{3+} or Nd^{3+} is introduced at the A site. One plausible reason for the worsening of the spin polarization is the modification of the electronic band structure associated with the increase of the Coulomb repulsion on electron doping. Another important source of spin depolarization is the promotion of AS disorder on electron doping. The factors that trigger the creation of AS disorder and its impact on the magnetic and transport properties of double perovskites have been thoroughly surveyed in sections 2.1.1 and 2.2. From the analysis we can conclude that the atomic ordering between B and B′ sites is optimized when the differences in valence and volume states of the B and B′ atoms is maximum.

The intrinsic sources of spin depolarization, together with the extrinsic opening of spin independent conduction channels across grain boundaries in polycrystalline A_2FeMoO_6 ceramics, decrease the low field magnetoresistance (LFMR) at and above room temperature. The LFMR in double perovskites is reliably attributed to intergrain tunnelling magnetoresistance (ITMR) between strongly spin polarized grains separated by insulating grain boundaries. We have expounded on the excellent agreement between the ITMR model developed in section 1.6 and the magnetoresistive response of double perovskites. Especially appealing is the strategy reported for studying the spin polarization in DPs by means of magnetoresistance measurements under high pulsed magnetic fields [108]. In this work, the importance of the magnetic state of the grain surface for setting the magnetoresistive response is emphasized.

Another interesting route to obtaining high Curie temperature DPs is exploiting the phase diagram of A_2FeReO_6 (A = Ca, Sr, Ba). In this series, the T_C variation of Ca-rich monoclinic

compounds deviates from the behaviour predicted by the hybridization mechanism between neighbouring t_{2g} states, and confirmed by the phase diagram of A_2FeMoO_6 (section 2.1.1), cubic A_2FeReO_6 (section 3.1.1) and $Sr_2Fe_{1-x}Cr_xReO_6$ (section 3.2.1). We believe that the anomalous T_C enhancement of Ca_2FeReO_6 ($T_C = 522$ K) results from an additional ferromagnetic interaction ascribed to the e_g states, which, as suggested by Wu *et al* [44], are pushed down in energy down to the Fermi level due to the strong monoclinic distortion of the cubic crystal electric field.

The study of the huge magnetic anisotropy observed in Re-based compounds has led us to work out a first order perturbation treatment of the spin–orbit coupling in the Re atom. This model nicely reproduces the predictions of complex band structure calculations introducing a relativistic Hamiltonian [177], as well as the experimental analysis of the XMCD spectra of Re-based double perovskites [176, 179, 180]. In brief, the model foresees the existence of an unquenched orbital moment at the Re atom, which arises from the strong tendency of the Re unpaired electrons to occupy the ground state with $\langle l_z \rangle = 1$ (i.e., antiparallel to the Re spin moment). Furthermore, slight distortions of the non-cubic part of the electrostatic potential created by the oxygen ligands in the ReO_6 octahedron can substantially modify the expected value and direction of the orbital moment. As a result, the coupling between the magnetic and structural degrees of freedom gives rise to a rich phenomenology in Re-based double perovskites. For instance, in section 2.1.3 we report on the totally unexpected magnetostructural transition at low temperatures in Ca-rich A_2FeReO_6. This entails a phase transition from a low temperature insulating and hard magnetic state towards a high temperature metallic and much softer magnetic state. The two phases belong to the same crystallographic space group ($P2_1/n$) but they do have different lattice parameters. When the low temperature phase appears, the sample coercivity undergoes a steep increase ascribed to the change of the magnetocrystalline anisotropy. The uniqueness of Ca-rich A_2FeReO_6 compounds also lies in the field induced transition from the low temperature phase to the high temperature one [38, 39, 173]. In section 3.1.4, a novel colossal magnetoresistance mechanism associated with the field induced coexistence of two phases with different conductivities is reported [191].

Among high T_C double perovskites, Sr_2CrReO_6 stands out as the magnetic oxide with the largest ever reported $T_C = 635$ K [36], with the only exception of ferrites. We have disclosed the origin of such a large T_C by addressing the phase diagram of the series $Sr_2Fe_xCr_{1-x}ReO_6$. As illustrated in figure 43(b), the evolution of the Curie temperature in these series can be fully understood within the above mentioned extension of Harrison's model applied to the structure of double perovskites (see section 3.2.1). We have recently started applying the electron doping technique to the Sr_2CrReO_6 compound in order to explore the possibilities of a further T_C enhancement, in analogy with previous works on FeMo double perovskites. Preliminary results suggest that, although a net electronic band filling of the mostly spin down states of the conduction band is achieved, the Curie temperature does not change significantly in the $Sr_{2-x}RE_xCrReO_6$ series (RE = La^{3+}, Nd^{3+} and Sm^{3+}), which means that the hybridization mechanism cannot be reinforced by an increase of the occupation number of the $Cr(t_{2g})$–$O(2p_\pi)$–$Re(t_{2g})$ hybrid sub-band [195]. The plausibility of a further T_C enhancement up to 725 K in Sr_2CrOsO_6 has been recently suggested on the basis that Os contributes to the t_{2g} sub-band with one more electron than Re. Such a 5d band filling is thought to place Sr_2CrOsO_6 at the end of a spin polarized metal–insulator transition [196]. In contrast, Sr_2CrReO_6 is metallic if grown as epitaxial thin films or hot sintered under high pressures, but it exhibits semiconducting-like transport behaviour if the sample porosity is high, mainly contributed by the grain boundary resistance. Sr_2CrReO_6 shows a magnetic anomaly similar to the one observed in Ca-rich A_2FeReO_6 compounds: an abrupt increase of the coercive field and peaked *ac* susceptibility at 160 K. Within the experimental error of the D2B high resolution

neutron diffractometer, we have shown that this magnetic transition is not accompanied by any kind of structural modification.

The existence of the large unquenched orbital moment in the Re atom in all the Re-based double perovskites has been confirmed by magnetostriction measurements. The A_2FeReO_6 and $Sr_2Fe_{1-x}Cr_xReO_6$ series show large volume and shape magnetostriction (with relative variations up to 1600×10^{-3}). On the other hand, the A_2FeMoO_6 isostructural compounds do not have magnetostriction at all, which indicates that the one observed in Re-based compounds is of single ion type. In compounds with high T_C and moderate coercivity (as for instance Sr_2FeReO_6) the magnetostriction is persistent at room temperature, which permits one to imagine magnetostrictive devices based on such double perovskites.

From the point of view of applications, the most celebrated property of double perovskites is its presumably full negative spin polarization of the carriers. We have found a value of $P = -0.86$ in $(Ba_{0.8}Sr_{0.2})_2FeMoO_6$ at 2 K. If we admit the ITMR effect as a probe of the bulk spin polarization, the series $Sr_{2-y}Ba_yFeReO_6$ must have the same degree of spin polarization as their FeMo analogues (see the figure 38), in good agreement with theoretical predictions based on band structure calculations. However, if we move to compounds showing larger T_C, for instance Ca_2FeReO_6 and Sr_2CrReO_6, it turns out that the magnetoresistive response at low fields dramatically worsens. Two features contribute to this serious drawback for certain applications. One is the enhanced magnetic anisotropy of Ca-rich A_2FeReO_6 and Sr_2CrReO_6, which makes the saturation field increase up to several teslas. The other is the intrinsic decrease of the spin polarization owing to the mixing of spin up and spin down states, which is expected from the off-diagonal boxes of the spin–orbit Hamiltonian given by equation (34). As illustrated in figure 30, the overlapping of t_{2g} up and down states is controlled by Δ'_{ex}, λ and ω^2, being respectively the exchange splitting induced in Re by the hybridization with the B atom, the spin–orbit coupling constant and the strength of the structural distortion with respect to the cubic ReO_6 octahedron. In our model, λ is the same for every Re-based double perovskite, but Δ'_{ex} and ω^2 depend on the B atom, the interatomic distances and the shape of the ReO_6 octahedra. Then, we can conclude that, when the energy scales of the spin–orbit coupling and the electrostatic interaction with the distorted ligand electric field become comparable to the exchange splitting in Re, not only is a non-zero orbital moment expected, but so also is a decrease of the spin polarization of the atomic states contributing to the conduction band. Following this idea, the spin depolarization of the carriers in a given compound will increase when the orbital moment does. This could be the reason that underlies the systematically smaller low field magnetoresistance in Ca-rich A_2FeReO_6 and Cr-rich $Sr_2Fe_{1-x}Cr_xReO_6$ than in Ba-rich and Fe-rich ones, as displayed in the figures 38 and 44. However, the use of intergrain magnetoresistance to study the spin polarization is troubling, because the extrinsic character of this phenomenon makes the analysis extremely sensitive to the preparation conditions. Therefore, in order to tackle the determination of the spin polarization in Re-based double perovskites, one should make use of more specific techniques such as spin polarized photoemission spectroscopy of *in situ* broken samples, tunnelling spectroscopy of epitaxial heterostructures, or point contact Andreev spectroscopy. We think that this is a very interesting research topic for the coming years, both from fundamental and technological viewpoints.

According to the here-revisited state of the art of the intensive research in the field of high T_C double perovskites performed since the publication by Kobayashi of their half-metallic nature in 1998 [11], several families of these compounds are ready to be explored as active elements in actual devices. Although we could not identify any double perovskite matching all the desirable industrial requirements (T_C well above room temperature, 100% of spin polarization, low coercivity and thermal stability), many particular properties of several compounds could offer advantageous performances with respect to existing solid state

devices under investigation. For instance, the $Ba_{1.6}Sr_{0.4}FeMoO_6$ polycrystalline ceramic, which has a very low mass production cost, exhibits a room temperature MR as large as 10% at 425 mT [136] that surpasses the best ever reported magnetoresistance for Fe_3O_4 pellets [197]. In addition, there are several ways to improve the effectiveness of the grain boundary insulating barrier [112], thus permitting one to fully exploit the large spin polarization of double perovskites. On the thin films side, if one takes into account the lower bound of the spin polarization reported for FeMo-based double perovskites, ($P = -86\%$; see figure 18 and [100, 108]), a hypothetical tunnel junction made up of two A_2FeMoO_6 (A = Sr, Ba) sandwiching an insulating barrier would yield up to 300% of tunnel magnetoresistance within Jullière's model [101]. At this point we notice that in order to build reliable devices based on double perovskites, the difficulty of thin film fabrication has to be overcome. The progress done in this line is promising. Given the feasibility of complex oxide epitaxial growth by means of pulsed laser deposition (PLD), several authors have applied this technique to double perovskites. Most of the work has been done on Sr_2FeMoO_6, but other compounds such as Sr_2CrReO_6 and Sr_2CrWO_6 have been grown in high quality epitaxial thin films. Metallic Sr_2FeMoO_6 with full saturation magnetization can be epitaxially grown on $SrTiO_3(001)$ substrates for a very narrow range of deposition temperature and atmosphere in order to avoid atomic disorder, oxygen vacancies and/or 3D growth [100, 102, 198]. The use of substrates with lower lattice mismatch makes easier the achievement of coherent growth without strain relaxation of Sr_2FeMoO_6 having nearly the same properties as the bulk [103]. The growth of Sr_2CrWO_6 also appears to be challenging. Philipp *et al* demonstrated layer-by-layer growth of Sr_2CrWO_6 on $SrTiO_3$ showing a perfect crystallinity and a surface flatness uniquely limited by the vicinality of the substrate [199]. Later on Majewski *et al* showed that La doped $Sr_{2-x}La_xCrWO_6$ could also be grown with excellent crystallinity [129]. However, the CrW-based thin films display depressed magnetic properties. On the other hand, the epitaxial growth of almost ideal Sr_2CrReO_6 onto $SrTiO_3$ oriented either along (001) or (111) seems to be much easier than in the FeMo case [103]. In fact, thanks to the better lattice mismatch and the less restrictive deposition conditions, high quality Sr_2CrReO_6 with surface roughness of 0.5 nm can be growth by sputtering stoichiometric targets, instead of using PLD techniques as in the previous cases. The growth of FeRe-based thin epitaxial films of double perovskites has not been addressed to our knowledge. In summary, although the growth of thin films of double perovskites is just an emerging research field, to date progress indicates that in the next few years major advances will be achieved in the epitaxial growth of the above mentioned compounds or even of different ones among the numerous families with interesting properties.

If this prediction is accomplished, we can think of many heterostructures based on double perovskites with advanced functionalities. For instance, at room temperature, all the A_2FeReO_6 are conducting. Then, tunnel junctions with Sr_2FeReO_6 and Sr_2FeMoO_6 electrodes, which possess a large degree of spin polarization, would lead to high TMR ratios with the advantage that magnetic decoupling is ensured beforehand. This is due to the larger magnetocrystalline anisotropy ascribed to the Re ion, which gives rise to quite different coercive fields in the FeRe and the FeMo electrodes. Consequently, the biasing of one of the electrodes by means of an antiferromagnetic layer underneath is unnecessary, which avoids one important source of surface roughness at electrode/barrier interfaces. Furthermore, the two electrodes would share the same lattice parameters, so that epitaxial growth of such heterostructures is feasible along several crystallographic directions. This would allow studying electron tunnelling not only as a function of the spin direction, but also as a function of the orbital symmetry, which, after the discovery of the orbital symmetry influence on TMR in Fe/MgO/Fe tunnel junctions [200, 201], has become an exciting topic in materials science. Another interesting and feasible heteroepitaxy would be that of Ca_2FeMoO_6/Ca_2FeReO_6

bilayers with a metallic counter-electrode on top. When the low temperature insulating phases of Ca_2FeReO_6 were formed, the tunnelling between Ca_2FeMoO_6 and the counter-electrode would be across an insulator with strongly exchange split sub-bands, which leads to the cutting edge topic of spin filtering devices. We believe that such heterostructures provide easier growth conditions for addressing spin filtering than other previously studied systems such as $Al/EuS/Al$ or $La_{2/3}Sr_{1/3}MnO_3/NiFe_2O_4$ [202, 203]. Finally, we would like to put forward a possible application of the magnetoelastic coupling in Re-based compounds. This is the strain induced resistance modulation which could be produced by a piezoelectric layer epitaxially grown on top of the double perovskite. Such an effect has been suggested to occur in $La_{0.7}Sr_{0.3}MnO_3/Pb(Zr_{0.5}Ti_{0.5})O_3$ [204], and it is caused by the dependence of the carrier mobility on the interatomic distances. We have seen that the weak structural transition at T_{sm} gives rise to a metal–insulator transition in Ca-rich A_2FeReO_6, and therefore, strong resistance changes can be expected if the double perovskite thin film is externally strained by a piezoelectric material. The analysis of the hydrostatic pressure effect on the magnetic and transport properties of A_2FeReO_6, and the study of T_{sm} as a function of epitaxial strain relaxation in A_2FeReO_6 films of different thicknesses could help to discern the viability of the proposed multiferroic device.

As a final remark, we would like to single out the importance of systematic studies on the spin polarization of Sr_2CrReO_6. Our pulsed field magnetoresistance measurements shown in figure 45 suggest that the spin polarization is rather low as compared to Sr_2FeReO_6. However, the extremely attractive possibilities of this theoretically considered half-metal with such a high Curie temperature definitively deserve further studies on the effective spin polarization in single crystals and thin films.

We hope that this review will trigger a renewed interest in the fundamental research into the underlying physics in double perovskite compounds showing double exchange-like ferromagnetism. We aim to encourage the scientific community to develop growth routes for thin films and single crystals, in order to realize breakthrough spintronic devices and provide answers to the limitations and open questions raised in this work.

Acknowledgments

References

[1] Jonker G H and Van Santen J H 1950 *Physica* **16** 337–49
[2] Zener C 1951 *Phys. Rev.* **82** 403–5
[3] Longo J and Ward R 1961 *J. Am. Chem. Soc.* **83** 2816–8
[4] Sleight A W, Longo J and Ward R 1962 *Inorg. Chem.* **1** 245–8
[5] Sleight A W and Weiher J F 1972 *J. Phys. Chem. Solids* **33** 679–87
[6] Patterson F K, Moeller C W and Ward R 1963 *Inorg. Chem.* **2** 196–8
[7] Galasso F S, Douglas F C and Kasper R J 1966 *J. Chem. Phys.* **44** 1672–8
[8] Nakayama S, Nakagawa T and Nomura S 1968 *J. Phys. Soc. Japan* **24** 219–20
[9] Nakagawa T 1968 *J. Phys. Soc. Japan* **24** 806–11
[10] Yokoyama H and Nakagawa T 1970 *J. Phys. Soc. Japan* **28** 1197–201
[11] Kobayashi K-I, Kimura T, Sawada H, Terakura K and Tokura Y 1998 *Nature* **395** 677–80

[12] Shannon R D 1976 *Acta Crystallogr.* A **32** 751
[13] Philipp J B, Majewski P, Alff L, Erb A and Gross R 2003 *Phys. Rev.* B **68** 144431
[14] Lufaso M W and Woodward P M 2001 *Acta Crystallogr.* B **57** 725–38
[15] Shikano M, Ishiyama O, Inaguma Y, Nakamura T and Itoh M 1995 *J. Solid State Chem.* **120** 238
[16] Popov G, Greenblatt M and Croft M 2003 *Phys. Rev.* B **67** 024406
[17] Azad A K, Ivanov S, Eriksson S G, Eriksen J, Rundlöf H, Mathieu R and Svedlindh P 2000 *Mater. Res. Bull.* **36** 2215
[18] Ritter C, Ibarra M R, Morellon L, Blasco J, García J and De Teresa J M 2000 *J. Phys.: Condens. Matter* **12** 8295–308
[19] Kapusta C, Zajac D, Riedi P C, Sikora M, Oates C J, Blasco J and Ibarra M R 2004 *J. Magn. Magn. Mater.* **272–276** e1619–21
[20] Chmaissem O, Drabowski B, Kolesnik S, Short S and Jorgensen J D 2005 *Phys. Rev.* B **71** 174421
[21] Gopalakrishnan J, Chattopadhyay A, Ogale S B, Venkatesan T and Greene R L 2000 *Phys. Rev.* B **62** 9538–42
[22] De Teresa J M, Serrate D, Blasco J, Ibarra M R and Morellon L 2004 *Phys. Rev.* B **69** 144401
[23] Azad A K, Eriksson S G, Mellegard A, Ivanov S A, Eriksen J and Rundlöf H 2002 *Mater. Res. Bull.* **37** 1797–813
[24] Blasco J, Ritter C, Morellon L, Algarabel P A, De Teresa J M, Serrate D, García J and Ibarra M R 2002 *Solid State Sci.* **4** 651–60
[25] Arulraj A, Ramesha K, Gopalakrishnan J and Rao C N R 2000 *J. Solid State Chem.* **155** 233–7
[26] Moritomo Y, Xu S, Machida A, Akimoto T, Nishibori E, Takata M and Sakata M 2000 *Phys. Rev.* B **61** R7828–30
[27] De Teresa J M, Serrate D, Ritter C, Blasco J, Ibarra M R, Morellon L and Tokarz W 2005 *Phys. Rev.* B **71** 092408
[28] Kato H, Okuda T, Okimoto Y, Tomioka Y, Oikawa K, Kamiyama T and Tokura Y 2004 *Phys. Rev.* B **69** 184412
[29] Philipp J B, Reisinger D, Schonecke M, Marx A, Erb A, Alff L and Gross R 2001 *Appl. Phys. Lett.* **79** 3654
[30] Itoh M, Ohta I and Inaguma Y 1996 *Mater Sci. Eng.* B **41** 55–8
[31] Popov G, Lobanov V, Tsiper E V, Greenblatt M, Caspi E N, Borissov A, Kiryukhin V and Lynn J W 2004 *J. Phys.: Condens. Matter* **16** 135–45
[32] Azad A K, Ivanov S, Eriksson S G, Rundlöf H, Eriksen J, Mathieu R and Svedlindh P 2001 *J. Magn. Magn. Mater.* **237** 124–34
[33] Chmaissem O, Kruk R, Dabrowski B, Brown D E, Xiong X, Kolesnik S, Jorgensen J D and Kimball C W 2000 *Phys. Rev.* B **62** 14197–205
[34] Kato H, Okuda T, Okimoto Y, Tomioka Y, Oikawa K, Kamiyama T and Tokura Y 2002 *Phys. Rev.* B **65** 144404
[35] Kobayashi K I, Okuda T, Tomioka Y, Kimura T and Tokura Y 2000 *J. Magn. Magn. Mater.* **218** 17–24
[36] Kato H, Okuda T, Okimoto Y, Tomioka Y, Takenoya Y, Ohkubo A, Kawasaki M and Tokura Y 2002 *Appl. Phys. Lett.* **81** 328–30
[37] Azad A K, Ivanov S A, Eriksson S G, Eriksen J, Rundlöf H, Mathieu R and Svedlindh P 2001 *Mater. Res. Bull.* **39** 2485–96
[38] Oikawa K, Kamiyama T, Kato H and Tokura Y 2003 *J. Phys. Soc. Japan* **72** 1411–7
[39] Westerburg W, Lang O, Ritter C, Felser C, Tremel W and Jacob G 2002 *Solid State Commun.* **122** 201–6
[40] Fu Z M and Li W X 1995 *Sci. China* A **38** 974–84
[41] Maekawa S, Tohyama T, Barnes S E, Ishihara S, Koshibae W and Khaliullin G 2003 *Physics of Transition Metal Oxides* (Berlin: Springer) chapter 1, 2
[42] Sarma D D, Mahadevan P, Saha-Dasgupta T, Ray S and Kumar A 2000 *Phys. Rev. Lett.* **85** 2549–52
[43] Kobayashi K I, Kimura T, Tomioka Y, Sawada H and Terakura K 1999 *Phys. Rev.* B **59** 11159–62
[44] Wu H 2001 *Phys. Rev.* B **64** 125126
[45] Vaitheeswaran G, Kanchana V and Delin A 2005 *Appl. Phys. Lett.* **86** 032513
[46] Wollan E O 1960 *Phys. Rev.* **117** 387–401
[47] Tomioka Y, Okuda T, Okimoto Y, Kumai R, Kobayashi K I and Tokura Y 2000 *Phys. Rev.* B **61** 422–7
[48] Linden J, Yamamoto T, Karppinen M and Yamauchi H 2000 *Appl. Phys. Lett.* **76** 2925–7
[49] Balcells Ll, Navarro J, Bibes M, Roig A, Martínez B and Fontcuberta J 2001 *Appl. Phys. Lett.* **78** 781–3
[50] Greneche J M, Venkatesan M, Suryanarayanan R and Coey J M D 2001 *Phys. Rev.* B **63** 174403
[51] Colis S, Stoeffler D, Mény C, Fix T, Leuvrey C, Pourroy G, Dinia A and Panissod P 2005 *J. Appl. Phys.* **98** 033905
[52] Kapusta Cz, Riedi P C, Zajac D, Sikora M, De Teresa J M, Morellon L and Ibarra M R 2002 *J. Magn. Magn. Mater.* **242–245** 701–3
[53] Sánchez D, Alonso J A, García-Hernández M, Martínez-Lope M J, Martínez J L and Mellegard A 2002 *Phys. Rev.* B **65** 104426

[54] Besse M *et al* 2002 *Europhys. Lett.* **60** 608–14
[55] Schiffer P, Ramirez A P, Bao W and Cheong S W 1995 *Phys. Rev. Lett.* **75** 3336–9
[56] Martínez B, Navarro J, Balcells Ll and Fontcuberta J 2000 *J. Phys.: Condens. Matter* **12** 10515–21
[57] Kang J S *et al* 2002 *Phys. Rev.* B **66** 113105
[58] Herrero-Martín J, García J, Subías G, Blasco J and Sánchez M C 2004 *J. Phys.: Condens. Matter* **16** 6877–90
[59] Herrero-Martín J, García J, Subías G, Blasco J and Sánchez M C 2005 *J. Phys.: Condens. Matter* **17** 4963–76
[60] Moreno M S, Gayone J E, Abbate M, Caneiro A, Niebieskikwiat D, Sánchez R D, de Siervo A, Landers R and Zampieri G 2001 *Solid State Commun.* **120** 161–4
[61] Nakamura S, Tanaka M, Kato H and Tokura Y 2003 *J. Phys. Soc. Japan* **72** 424–8
[62] Moreno M S, Gayone J E, Abbate M, Caneiro A, Niebieskikwiat D, Sánchez R D, De Siervo A, Landers A and Zampieri G 2001 *Solid State Commun.* **120** 161–4
[63] García-Landa B, Ritter C, Ibarra M R, Blasco J, Algarabel P A, Mahendiran R and García J 1999 *Solid State Commun.* **110** 435–8
[64] Kanamori J and Terakura K 2001 *J. Phys. Soc. Japan* **70** 1433–4
[65] Fang Z, Terakura K and Kanamori J 2001 *Phys. Rev.* B **63** 180407(R)
[66] Carvajal E, Navarro O, Allub R, Avignon M and Alascio B 2005 *Eur. Phys. J.* B **48** 179–87
[67] Ritter C, Blasco J, De Teresa J M, Serrate D, Morellon L, García J and Ibarra M R 2004 *Solid State Sci.* **6** 419–31
[68] Chattopadhyay A and Millis A J 2001 *Phys. Rev.* B **64** 024424
[69] Alonso J L, Fernández L A, Guinea F, Lesmes F and Martín-Mayor V 2003 *Phys. Rev.* B **67** 214423
[70] Brey L, Calderón M J, Das Sarma S and Guinea F 2006 *Phys. Rev.* B **74** 094429
[71] Tovar M, Causa M T, Butera A, Navarro J, Martínez B, Fontcuberta J and Passeggi M C G 2002 *Phys. Rev.* B **66** 024409
[72] Navarro J, Balcells Ll, Martínez B and Fontcuberta J 2001 *J. Appl. Phys.* **89** 7684–6
[73] Harrison W A 1999 *Elementary Electronic Structure* (Singapore: World Scientific)
[74] Andersen O K and Jepsen O S 1977 *Physica* B&C **91** 317–28
[75] Radaelli P G, Iannone G, Marezio M, Hwang H Y, Cheong S W, Jorgensen J D and Argyriou D N 1997 *Phys. Rev.* B **56** 8265–76
[76] Okimoto Y, Katsufuji T, Okada Y, Arima T and Tokura Y 1995 *Phys. Rev.* B **51** 9581–8
[77] Kim B G, Hor Y S and Cheong S W 2001 *Appl. Phys. Lett.* **79** 388–90
[78] Medarde M, Mesot J, Lacorre P, Rosenkranz S, Fisher P and Gobrecht K 1995 *Phys. Rev.* B **52** 9248–58
[79] García-Muñoz J L, Fontcuberta J, Suaadi M and Obradors X 1996 *J. Phys.: Condens. Matter* **8** L787–93
[80] Fang T T 2005 *Phys. Rev.* B **71** 064401
[81] Zajac D, Kapusta Cz, Riedi P C, Sikora M, Oates C J, Rybicki D, Blasco J, Serrate D, De Teresa J M and Ibarra M R 2004 *J. Magn. Magn. Mater.* **272–276** 1756–8
[82] Wojcik M, Jedryka E, Nadolski S, Navarro J, Rubi D and Fontcuberta J 2004 *Phys. Rev.* B **69** 100407(R)
[83] Serrate D, De Teresa J M, Blasco J and Ibarra M R 2005 *J. Magn. Magn. Mater.* **290/291** 1021–4
[84] Moritomo Y, Shimamoto N, Xu S, Machida A, Nishibori E T, Takata M, Sakata M and Nakamura A 2001 *Japan. J. Appl. Phys.* **40** L672–4
[85] Ogale A S, Ogale S B, Ramesh R and Venkatesan T 1999 *Appl. Phys. Lett.* **75** 537–9
[86] Ray S, Kumar A, Sarma D D, Cimino R, Turchini S, Zennaro S and Zema N 2001 *Phys. Rev. Lett.* **87** 097204
[87] Rubi D, Frontera C, Roig A, Nogués J, Muñoz J S and Fontcuberta J 2005 *J. Phys.: Condens. Matter* **17** 8037–47
[88] Topwal D, Sarma D D, Kato H, Tokura Y and Avignon M 2006 *Phys. Rev.* B **73** 094419
[89] Navarro J, Nogués J, Muñoz J S and Fontcuberta J 2003 *Phys. Rev.* B **67** 174416
[90] Frontera C and Fontcuberta J 2004 *Phys. Rev.* B **69** 014406
[91] Rubi D, Navarro J, Fontcuberta J, Izquierdo M, Avila J and Asensio M C 2006 *J. Phys. Chem. Solids* **67** 575–8
[92] Saha-Dasgupta T and Sarma D D 2001 *Phys. Rev.* B **64** 064408
[93] Stoeffler D and Colis S 2005 *J. Phys.: Condens. Matter* **17** 6415–24
[94] Linden J, Karppinen M, Shimada T, Yasukawa Y and Yamauchi H 2003 *Phys. Rev.* B **68** 174415
[95] Yin H Q, Zhou J S, Dass R, Zhou J P, McDevitt J T and Goodenough J B 2000 *J. Appl. Phys.* **87** 6761–3
[96] Fang T T 2005 *Phys. Rev.* B **71** 064401
[97] Navarro J, Balcells Ll, Sandiumenge F, Bibes M, Roig A, Martínez B and Fontcuberta J 2001 *J. Phys.: Condens. Matter* **13** 8481–8
[98] Zajac D 2006 NMR and XAS study of magnetic and electronic properties of double perovskites *PhD Thesis* AGH University of Science & Technology
[99] Yu X, Asaka T, Tomioka Y, Tsuruta C, Naai T, Kimoto K, Kaneko Y, Tokura Y and Matsui Y 2005 *J. Electron Microsc.* **54** 61–5
[100] Bibes M *et al* 2003 *Appl. Phys. Lett.* **83** 2629–31

[101] Jullière M 1975 *Phys. Lett.* A **54** 225–6
[102] Westerburg W, Reisinger D and Jacob G 2000 *Phys. Rev.* B **62** R767–70
[103] Asano H, Kohara Y and Matsui M 2002 *Japan. J. Appl. Phys.* **41** L1081–3
[104] Sánchez D, García-Hernández M, Auth N and Jacob G 2004 *J. Appl. Phys.* **96** 2736–42
[105] Fontcuberta J *et al* 2002 *J. Magn. Magn. Mater.* **242–245** 98–104
[106] Inoue J and Maekawa S 1996 *Phys. Rev.* B **53** R11927–9
[107] Slonczewski J C 1989 *Phys. Rev.* B **39** 6995–7002
[108] Serrate D, De Teresa J M, Algarabel P A, Ibarra M R and Galibert J 2005 *Phys. Rev.* B **71** 104409
[109] Serrate D, De Teresa J M, Algarable P A, Fernández-Pacheco R, Galibert J and Ibarra M R 2005 *J. Appl. Phys.* **97** 084317
[110] Yin H Q, Zhou J S, Zhou J P, Dass R, McDevitt J T and Goodenough J B 1999 *Appl. Phys. Lett.* **75** 2812–4
[111] Niebieskikwiat D, Prado F, Caneiro A and Sánchez R D 2004 *Phys. Rev.* B **70** 132412
[112] Zhong W, Liu W, Au C T and Du Y W 2006 *Nanotechnology* **17** 250–6
[113] Yuan C L, Wang S G, Song W H, Yu T, Dai J M, Ye S L and Sun Y P 1999 *Appl. Phys. Lett.* **75** 3853–5
[114] Eerenstein W, Palstra T T M, Saxena S S and Hibma T 2002 *Phys. Rev. Lett.* **88** 247204
[115] Serrate D, De Teresa J M, Blasco J, Ibarra M R and Morellón L 2002 *Appl. Phys. Lett.* **80** 4573–5
[116] Moritomo Y, Xu S, Machida A, Akimoto T, Nishibori E, Takata M, Sakata M and Ohoyama K 2000 *J. Phys. Soc. Japan* **69** 1723–6
[117] Wojcik M, Jedryka E, Nadolski S, Rubi D, Frontera C, Fontcuberta J, Jurca B, Dragoe N and Berthet P 2005 *Phys. Rev.* B **71** 104410
[118] Rubi D, Frontera C, Fontcuberta J, Wojcik M, Jedryka E and Ritter C 2004 *Phys. Rev.* B **70** 094405
[119] Ritter C, Rubí D, Navarro J, Frontera C, García-Muñoz J L and Fontcuberta J 2004 *J. Magn. Magn. Mater.* **272–276** 852–4
[120] Frontera C, Rubí D, Navarro J, García-Muñoz J L and Fontcubera J 2003 *Phys. Rev.* B **68** 012412
[121] Rodríguez-Martínez L M and Attfield J P 2000 *Phys. Rev.* B **63** 024424
[122] Akahoshi D, Uchida M, Tomioka Y, Arima T, Matsui Y and Tokura Y 2003 *Phys. Rev. Lett.* **90** 177203
[123] Attfield J P, Kharlanov A L and McAllister J A 1998 *Nature* **394** 157–9
[124] Sher F, Venimadhav A, Blamire M G, Kamenev K and Attfield J P 2005 *Chem. Mater.* **17** 176–80
[125] Rubi D, Frontera C, Nogués J and Fontcuberta J 2004 *J. Phys.: Condens. Matter* **16** 3173–82
[126] Serrate D, De Teresa J M, Blasco J, Ibarra M R, Morellon L and Ritter C 2004 *Eur. Phys. J.* B **39** 35–40
[127] Navarro J, Frontera C, Balcells Ll, Martínez B and Fontcuberta J 2001 *Phys. Rev.* B **64** 092411
[128] Yang H M, Lee W Y, Han H, Lee B W and Kim C S 2003 *J. Appl. Phys.* **93** 6987–9
[129] Majewski P, Geprägs S, Boger A, Opel M, Alff L and Gross R 2005 *J. Magn. Magn. Mater.* **290/291** 1154–7
[130] Geprägs S, Majewski P, Gross R, Ritter C and Alff L 2006 *J. Appl. Phys.* **99** 08J102
[131] Navarro J, Fontcuberta J, Izquierdo M, Avila J and Asension M C 2004 *Phys. Rev.* B **69** 115101
[132] Saitoh T, Nakatake M, Nakajima H, Moritomo O, Kakizaki A, Xu Sh, Moritomo Y, Hamada N and Aiura Y 2005 *J. Electron Spectrosc. Relat. Phenom.* **144–147** 601–3
[133] Saitoh T, Nakatake M, Nakajima H, Moritomo O, Kakizaki A, Xu Sh, Moritomo Y, Hamada N and Aiura Y 2005 *Preprint* cond-mat/0504066
[134] Kim G *et al* 2006 *J. Appl. Phys.* **99** 08Q309
[135] Zhou J P, Dass R, Yin H Q, Zhou J S, Rabenberg L and Goodenough J B 2000 *J. Appl. Phys.* **87** 5037–9
[136] Douvalis A P, Venkatesan M, Velasco P, Fitzgerald C B and Coey J M D 2003 *J. Appl. Phys.* **93** 8071–3
[137] Moritomo Y, Xu Sh, Akimoto T, Machida A, Hamada N, Ohoyama K, Nishibori E, Takata M and Sakata M 2000 *Phys. Rev.* B **62** 14224–8
[138] Zajac D, Kapusta Cz, Riedi P C, Sikora M, Oates C J, Rybicki D, De Teresa J M, Serrate D, Marquina C and Ibarra M R 2004 *Acta Phys. Pol.* **106** 759–65
[139] Ibarra M R and De Teresa J M 1998 Magnetotransport and magnetoelastic effects in manganese-oxide perovskites *Colossal Magnetoresistance, Charge Ordering and Related Properties of Manganese-Oxides* ed C N R Rao and B Raveau (Singapore: World Scientific) p 83
[140] Hwang H Y, Cheong S W, Ong N P and Batlogg B 1996 *Phys. Rev. Lett.* **77** 2041–4
[141] Ranno L, Barry A and Coey J M D 1997 *J. Appl. Phys.* **81** 5774–6
[142] Coey J M D, Berkowitz A E, Balcells Ll and Putris F F 1998 *Phys. Rev. Lett.* **80** 3815–8
[143] Mathieu R, Svedlindh P, Chakalov R A and Ivanov Z G 2000 *Phys. Rev.* B **62** 3333–9
[144] Ziese M, Höhne R, Semmelhack H C, Reckentin H, Hong N H and Esquinazi P 2002 *Eur. Phys. J.* B **28** 415–22
[145] Park J H, Vescovo E, Kim H J, Kwon C, Ramesh R and Venkatesan T 1998 *Phys. Rev. Lett.* **81** 1953–6
[146] Dulli H, Dowben P A, Liou S H and Plummer E W 2000 *Phys. Rev.* B **62** R14629–32
[147] Jansen R and Moodera J S 2000 *Phys. Rev.* B **61** 9047–50
[148] Dai J and Tang J 2001 *Phys. Rev.* B **63** 064410

[149] Rubi D and Foncuberta J 2006 *J. Phys.: Condens. Matter* **18** 7991–8

[150] Serrate D 2005 Spin dependent transport in double perovskites and magnetic nanostructures *PhD Thesis* University of Zaragoza (Z-2.805-2005)

[151] Zhang Q, Rao G H, Dong H Z, Xiao Y G, Feng X M, Liu G Y, Zhang Y and Liang J K 2005 *Physica* B **370** 228–35

[152] Niebieskikwiat D, Caneiro A, Sánchez R D and Fontcuberta J 2001 *Phys. Rev. B* **64** 180406(R)

[153] Sharma A, Berenov A, Rager J, Brandfor W, Bugoslavsky Y, Cohen L F and MacManus-Driscoll J L 2003 *Appl. Phys. Lett.* **83** 2384–6

[154] Kozlova N, Dörr K, Eckert D, Walter T and Müller K H 2003 *J. Magn. Magn. Mater.* **261** 48–55

[155] Chudnovsky E M, Saslow W M and Serota R A 1986 *Phys. Rev. B* **33** 251–61

[156] Tejada J, Martínez B, Labarta A and Chudnovsky E M 1991 *Phys. Rev. B* **44** 7698–700

[157] Fisher B, Chashka K B, Patlagan L and Reisner G M 2004 *J. Magn. Magn. Mater.* **272–276** 1790–1

[158] Liu G Y, Rao G H, Feng X M, Yang H F, Ouyang Z W, Liu W F and Liang J K 2003 *J. Alloys Compounds* **353** 42–7

[159] Rao G H, Liu G Y, Feng X M, Zhang Q and Liang J K 2005 *Sci. Technol. Adv. Mater.* **6** 750–4

[160] Solovyev I V 2002 *Phys. Rev. B* **65** 144446

[161] Rubi D, Frontera C, Roig A, Nogués J, Muñoz J S and Fontcuberta J 2006 *Mater. Sci. Eng. B* **126** 139–42

[162] Liu G Y, Rao G H, Feng X M, Yang H F, Ouyang Z W, Liu W F and Liang J K 2003 *Physica* B **334** 229–33

[163] Zhang Q, Rao G H, Feng X M, Liu G Y, Xiao Y G, Zhang Y and Liang J K 2005 *Solid State Commun.* **133** 223–7

[164] Feng X M *et al* 2002 *J. Phys.: Condens. Matter* **14** 12503–11

[165] Feng X M, Rao G H, Liu G Y, Yang H F, Liu W F, Ouyang Z W and Liang J K 2004 *Physica* B **344** 21–6

[166] Sriti F, Maignan A, Martin C and Raveau B 2001 *Chem. Mater.* **13** 1746–51

[167] Alamelu T, Varadaraju U V, Venkatesan M, Douvalis A P and Coey J M D 2002 *J. Appl. Phys.* **91** 8909–11

[168] Sriti F, Nguyen N, Martin C, Ducouret A and Raveau B 2002 *J. Magn. Magn. Mater.* **250** 123–30

[169] Asano H, Kozuka N, Tsuzuki A and Matsui M 2004 *Appl. Phys. Lett.* **85** 263–5

[170] Iwasawa H, Saitoh T, Yamashita Y, Ishii D, Kato H, Hamada N, Tokura Y and Sarma D D 2005 *Phys. Rev. B* **71** 075106

[171] Dai J M, Song W H, Wang S G, Ye S L, Wang K Y, Du J J, Sun Y P, Fang J, Chen J L and Gao B J 2001 *Mater. Sci. Eng.* **83** 217–22

[172] Auth N, Jakob G, Westerburg W, Ritter C, Bonn I, Felser C and Tremel W 2004 *J. Magn. Magn. Mater.* **272–276** e607–8

[173] Granado E, Huang Q, Lynn J W, Gopalakrishnan J, Greene R L and Ramesha K 2002 *Phys. Rev. B* **66** 064409

[174] Serrate D, De Teresa J M, Algarabel P A, Marquina C, Morellon L, Blasco J and Ibarra M R 2005 *J. Magn. Magn. Mater.* **290/291** 843–5

[175] Ferreira F F, Granado E, Carvalho W Jr, Skycia S W, Bruno D and Droppa R Jr 2005 *J. Synchrotron Radiat.* **13** 46–53

[176] Sikora M, Zajac D, Kapusta Cz, Borowiec M, Oates C J, Prochazka V, Rybicki D, De Teresa J M, Marquina C and Ibarra M R 2005 *Appl. Phys. Lett.* **89** 062509
      Sikora M, Zajac D, Kapusta Cz, Borowiec M, Oates C J, Prochazka V, Rybicki D, De Teresa J M, Marquina C and Ibarra M R 2005 *Preprint* cond-mat/0503358, 1

[177] Jeng H T and Guo G Y 2003 *Phys. Rev. B* **67** 094438

[178] Griffith J S 1964 *The Theory of Transition Metal Ions* (Cambridge: University Press)

[179] Majewski P, Geprëgs S, Sanganas O, Opel M, Gross R, Wilhelm F and Rogalev A 2005 *Appl. Phys. Lett.* **87** 202503

[180] Majewski P *et al* 2005 *Phys. Rev. B* **72** 132402

[181] Cohen-Tannoudji C, Diu B and Laloë F 1977 *Quantum Mechanics* vol I (New York: Wiley)

[182] Sugano S, Tanabe Y and Kamimura H 1970 *Multiplets of Transition-Metal Ions in Crystals* (New York: Academic) p 154

[183] Vaitheeswaran G, Kanchana V and Delin A 2006 *J. Phys.: Conf. Ser.* **29** 50–3

[184] Prellier W, Smolyaninova V, Biswas A, Galley C, Greene R L, Ramesha K and Gopalakrishnan J 2000 *J. Phys.: Condens. Matter* **12** 965–73

[185] De Teresa J M, Ibarra M R, Blasco J, García J, Marquina C and Algarabel P A 1996 *Phys. Rev. B* **54** 1187–93

[186] Ibarra M R, Mahendiran R, Marquina C, García-Landa B and Blasco J 1998 *Phys. Rev. B* **57** R3217–20

[187] Del Moral A *et al* 2002 *J. Magn. Magn. Mater.* **242–245** 788–96

[188] Del Moral A 2006 *Handbook of Magnetostriction and Magnetostrictive Materials* (London: Taylor and Francis) at press

[189] Callen E and Callen H B 1965 *Phys. Rev.* **139** A455–71

[190] Ibarra M R, Del Moral A and Abell J S 1984 *J. Magn. Magn. Mater.* **46** 157–66
[191] De Teresa J M, Serrate D, Blasco J, Ibarra M R and Morellón L 2005 *J. Magn. Magn. Mater.* **290/291** 1043–9
[192] Serrate D, De Teresa J M, Algarabel P A, Blasco J, Morellón L, Ibarra M R, Ritter C and Galibert J 2006 *Phys. Rev.* B submitted
[193] Fisher B, Chashka B, Patlagan L and Reisner G M 2004 *Phys. Rev.* B **70** 205109
[194] Serrate D, De Teresa J M, Blasco J, Morellon L and Ibarra M R 2006 in preparation
[195] Michalik J, De Teresa J M, Serrate D, Blasco J and Ibarra M R 2006 *J. Magn. Magn. Mater.* at press
[196] Alff L 2006 private communication
[197] Wang W, Yu M, Chen Y and Tang J 2006 *J. Appl. Phys.* **99** 08J108
[198] Di Trolio A, Larciprete R, Testa A M, Fiorani D, Imperatori P, Turchini S and Zema N 2006 *J. Appl. Phys.* **100** 013907
[199] Philipp J B, Reisinger D, Schonecke M, Opel M, Marx A, Erb A, Alff L and Gross R 2003 *J. Appl. Phys.* **93** 6853–5
[200] Faure-Vincent J, Tiusan C, Jouguelet E, Canet F, Sjieddine M, Bellouard C, Popota E, Hehn M, Montaingne F and Schuhl A 2003 *Appl. Phys. Lett.* **82** 4507–9
[201] Yuasa S, Nagahama T, Fukushima A, Suzuki Y and Ando K 2004 *Nat. Mater.* **3** 868–71
[202] Moodera J S, Hao X, Gibson G A and Meservey R 1988 *Phys. Rev. Lett.* **61** 637–40
[203] Lüders U, Bibes M, Bouzehouane K, Jacquet E, Contour J P, Fusil S, Bobo J F, Fontcuberta J, Barthélémy A and Fert A 2006 *Appl. Phys. Lett.* **88** 082505
[204] Thiele C, Dörr K, Lin W M, Müller K H and Schultz L 2006 *Sensors Actuators* A **129** 180–3